On the Extremal Principles in the Theory of Irreversible Processes

A. S. Pleshanov

Presented by Academician G.S. Golitsyn June 15, 2001

Received June 20, 2001

The variational principle in the theory of irreversible processes, i.e., the principle of the minimum of the algebraic sum of squares of dissipative flows in a stationary nonequilibrium state, is proposed. This sum is in fact the difference between the sum of squares of proper dissipative flows integrated over the Kirchhoff potential and the square of the thermal flux, which is a consequence of a purely transport character of the heat conduction function. Some applications of the principle introduced and the well-known principle of the minimum energy dissipation in the stationary state are considered. In particular, the conclusion is made that in some specific tasks, a solution to the energy equation near the stationary nonequilibrium state can be replaced by the condition of constant dissipation. Such an asymptotic representation is a consequence of the principle of the minimum dissipation.

1. As an extremal principle for the parabolic dissipative equation that describes a non-steady-state irreversible process, I imply the variational principle whose steady-state condition is given by the same equation that describes an irreversible process in the final stationary state, which can also be nonequilibrium. We can say that the steady-state condition is fulfilled here in a literal sense. If the equation of an irreversible process described by a certain function $u(t, \mathbf{r})$ has the form

$$u_t = f[t, \mathbf{r}; u, (\mathbf{v}\nabla)u, \Delta u, \dots],$$

and the functional $J(t)$ is given by the relation

$$J(t) = \int \mathscr{L} dV,$$

then its first variation is expressed as

$$\delta J = \int \delta \mathscr{L} dV = \delta J_e + \delta J_i \equiv \delta J_e + \int f \delta u dV,$$

and the steady-state condition $\delta J = 0$ is equivalent to the conditions

$$\delta J_e = 0, \quad f(t = \infty, \dots) = 0.$$

OAO Krzhizhanovskiĭ Power Engineering Institute, Leninskii pr. 19, Moscow, 117927 Russia

Here, $\mathscr{L}$ is the Lagrangian, the subscripts e and i are related to the external and internal parts of J, and the remaining notation is that used in [1]. Two extremal principles are known in the mechanics of dissipative continua: the principle of the minimal energy dissipation (PMED) in a stationary state and the principle of the minimum entropy production in the same state [2] (see also [3]). The first principle gives the steady-state equations of motion and continuity equations for substances (impurities, charges) in the diffusion approximation. The second leads to the steady-state energy equations under particular assumptions. An attempt to extend the domain in which the second principle is correct was made in [4] using a certain identity transformation of the initial nonlinear heat conduction equation. According to [2], this principle is valid only if the heat conduction coefficient is $\kappa(T) \sim T^{-2}$ (where T is temperature). It was found, however, that such a transformation occurs only at the expense of lowering the level of generality of geometric description (a transition to one-dimensional description) and boundary conditions (adiabaticity). The latter implies that the final state is equilibrium. Moreover, only the necessary condition was obtained in [4] for the minimum of entropy production, rejecting, in essence, the variational description of the problem at hand. This follows from the fact that the steady-state condition $\mathrm{div}\,\mathbf{q} = 0$ (where $\mathbf{q}$ is the thermal flux) cannot be obtained, in general, from the variational principle [2] (more exactly, in the case of identical fulfillment of this condition by virtue of the equality $\mathbf{q} = 0$). Here we set forth the possibility of invoking the variational principle that meets all above-listed general requirements.

2. Channels for dissipation and scattering of energy follow from the general heat transfer equation (entropy equation; see, e.g., [1])

$$\rho T \frac{ds}{dt} = \left(\sigma'_{ik} \frac{\partial v_i}{\partial x_k} + \frac{\mathbf{j}^2}{\sigma} + Q + \frac{\mathbf{i}^2}{\alpha_d} + \frac{\mathbf{i}^2}{\alpha_f} \right) \tag{1}$$
$$- \mathrm{div}\,\mathbf{q} \equiv \mathscr{L}_1 - \mathrm{div}\,\mathbf{q},$$

where bracketed terms are related to viscous, Joule, chemical, diffusion, and filtration energy dissipation

(its transformation into heat), while the term $\operatorname{div}\mathbf{q}$ corresponds to the transfer (scattering) of heat due to the heat conduction. Here,

$$\sigma'_{ik} = \eta\left(\frac{\partial v_i}{\partial x_k} + \frac{\partial v_k}{\partial x_i}\right) \equiv \eta s'_{ik} \tag{2}$$

is the incompressible (for the sake of simplicity) part of the tensor of viscous stresses;

$$\mathbf{j} = -\sigma\nabla\varphi \tag{3}$$

is the electric current density, and φ is the potential. In the diffusion treatment, the mass flux $\mathbf{i}$ has the form

$$\mathbf{i} = -\rho D\nabla c \equiv -\alpha_d\left(\frac{\partial\mu}{\partial c}\right)_{T,\,p}\nabla c, \tag{4}$$

while in the filtration treatment it is

$$\mathbf{i} = -\rho\frac{k}{\eta}\nabla p \equiv -\alpha_f\left(\frac{\partial\mu}{\partial p}\right)_{T,\,c}\nabla p. \tag{5}$$

Here, μ is the chemical potential, c is the concentration, and k is the permeability of the porous medium. Clearly, $k > 0$, and thermodynamic derivatives

$$\left(\frac{\partial\mu}{\partial c}\right)_{T,\,p},\quad \left(\frac{\partial\mu}{\partial p}\right)_{T,\,c} = \left(\frac{\partial V}{\partial c}\right)_{T,\,p}$$

are also positive. Finally,

$$\mathbf{q} = -\kappa\nabla T \equiv -\nabla K, \tag{6}$$

where $K = \int\kappa dT$ is the Kirchhoff potential. In the formulas for the fluxes, small irreversible crosseffects (such as thermal diffusion) are disregarded. In the general case, the positive dissipative coefficients of viscosity η, electric conduction σ, diffusion D, and heat conduction κ depend on T. For the flux $\mathbf{q}$, the functional F, for which the steady-state condition with respect to T yields the relation $\mathcal{L}_1 - \operatorname{div}\mathbf{q} = 0$, is similar to [5]:

$$F = \int\mathcal{L}_2 dV \equiv \int\left(\int\mathcal{L}_1 dK - \frac{\mathbf{q}^2}{2}\right)dV$$

$$= \int\left[\left(\int\eta dK s'_{ik}\frac{\partial v_i}{\partial x_k} + \int\frac{dK}{\sigma}\mathbf{j}^2\right.\right. \tag{7}$$

$$\left.\left. + \int QdK + \int\frac{dK}{\alpha_d}\mathbf{i}^2 + \int\frac{dK}{\alpha_f}\mathbf{i}^2\right) - \frac{\mathbf{q}^2}{2}\right]dV.$$

Indeed, the condition $\mathcal{L}_1 - \operatorname{div}\mathbf{q} = 0$ follows from

$$\delta F = \int\delta\mathcal{L}_2 dV$$

$$= \int\delta K(\mathbf{q}d\mathbf{S}) + \int(\mathcal{L}_1 - \operatorname{div}\mathbf{q})\delta K dV = 0$$

in view of $\delta T_e = 0$ or $\mathbf{q}_e = 0$. The variational principle (7) is determined as the principle of the minimum algebraic sum of squares of dissipative fluxes (PMDF) in the steady-state nonequilibrium state. As can be seen

from (7), the algebraic sum is, in essence, the difference between the sum of squares of dissipative fluxes integrated over K and the square of the heat flux. This follows from the fact that the heat flux enters as a linear term into the general heat-transfer equation (1), implying a purely transport character of the heat conduction function that represents the sole channel for energy (heat) dissipation. The functional

$$D = \int\mathcal{L}_1 dV \tag{8}$$

in cases (3)–(6) has the Lagrangian

$$\mathcal{L}_1 = \frac{1}{2}\frac{\mathbf{I}^2}{L} = \frac{1}{2}L(\nabla\Phi)^2,\quad \mathbf{I} = -L\nabla\Phi,$$

where $\mathbf{I}$ is the flux, Φ is the potential, and $L > 0$ is the kinetic coefficient, which is independent of Φ. The variation of the functional

$$\delta D = -\int\delta\Phi(\mathbf{I}d\mathbf{S}) + \int\delta\Phi\operatorname{div}\mathbf{I}dV = 0$$

yields the steady-state continuity equations of the diffusion type

$$\operatorname{div}\mathbf{I} = 0.$$

The functional

$$D = \frac{1}{2}\int\sigma'_{ik}\frac{\partial v_i}{\partial x_k}dV$$

leads to the steady-state equation of motion for an incompressible fluid, which follows from

$$\Delta\mathbf{v} = 0,$$

$$\delta D = \int\sigma'_{ik}\delta v_i dS_k - \int\eta(\Delta\mathbf{v}\delta\mathbf{v})dV = 0.$$

Finally, the functional

$$F = \int\frac{\mathbf{q}^2}{2}dV,$$

by analogy with (8), yields the steady-state energy equation

$$\operatorname{div}\mathbf{q} = 0.$$

The combined cases are of greater interest.

3. We consider first the isothermal mode of a steady-state flow for a viscous incompressible fluid through a channel under the action of a longitudinal (with respect to the channel) pressure gradient. If a plane (along the channel radius) profile of the longitudinal velocity is specified at the channel inlet, i.e.,

$$u = \text{const} = U_0, \tag{9}$$

then, under the action of the viscosity, this profile changes as the longitudinal coordinate z increases; as $z \longrightarrow \infty$, the profile approaches asymptotically to the stabilized Poiseuille profile. Thus, if the flow was non-equilibrium with respect to both coordinates at its transition segment, it will remain nonequilibrium after stabilization only along the radius. Within standard approximations, $\left|\dfrac{u_{zz}}{u_{rr}}\right| \ll 1$,

$$p_r = 0, \qquad (10)$$

and with allowance for the boundary conditions

$$u_r(z, 0) = 0, \quad u(z, a) = 0, \qquad (11)$$

$$v(z, 0) = 0, \quad v(z, a) = 0, \qquad (12)$$

the integrals of the steady-state axisymmetric continuity equations, the motion, and mechanical energy take the form

$$\left(\int_0^a u r^n dr \right)_z = 0, \qquad (13)$$

$$\rho_0 \left(\int_0^a u^2 r^n dr \right)_z + \frac{a^{n+1}}{n+1} p_z = \eta_0 a^n u_r(z, a), \qquad (14)$$

$$\rho_0 \left(\int_0^a \frac{u^3}{2} r^n dr \right)_z + p_z \int_0^a u r^n dr = -\eta_0 \int_0^a u_r^2 r^n dr, \qquad (15)$$

where the values $n = 0, 1$ are related to the planar and cylindrical geometry, respectively, and the indices imply partial differentiation. Giving up the traditional isolation of a boundary layer, we introduce the variable profile, unified throughout the channel cross section,

$$u(z, r) = U\varphi(\xi) \equiv U\varphi_0(\xi)(1 + a_1 \xi^v + a_2 \xi^{2v} + \dots). \ (16)$$

Here, $\varphi_0 = 1 - \xi^v$, $\xi = \dfrac{r}{a} \in (0; 1)$, and $U, v, a_1, a_2, \dots$ are the functions of z to be determined. For the simplest situation, in which $a_1, a_2, \dots$ are disregarded, we obtain the closed system of equations (13)–(15) for determining p, U, and v. The initial conditions p_0 and U_0 are assumed specified. Setting $u(0, r) = U_0$, we arrive at the initial condition

$$v(z \longrightarrow 0) \longrightarrow \infty. \qquad (17)$$

In this case, the variational principle takes the form of the PMED specific for the problem of a conditional extremum:

$$J = D + \lambda G \equiv \frac{1}{2}\eta_0 \int_0^a u_r^2 r^n dr + p_z \int_0^a u r^n dr, \qquad (18)$$

where $\lambda = p_z = const$ is the Lagrange coefficient and $G = const$ is the mass rate [integral (13)]. The condition

$\delta J = 0$ yields the steady-state equation of motion, as follows from

$$\delta J = (\eta_0 r^n u_r \delta u)\big|_0^a + \int_0^a [r^n p_z - \eta_0 (r^n u_r)_r] \delta u \, dr = 0.$$

Substitution of $u = U\varphi_0$ into G gives U as a function of v:

$$\frac{U}{U_0} = 1 + \frac{n+1}{v}.$$

Hence,

$$D = \frac{1}{2}\eta_0 U_0^2 a^{n-1} \frac{(v+n+1)^2}{2v+n-1},$$

and the variation of D with respect to v has the form

$$\delta D = 2D \frac{v-2}{(v+n+1)(2v+n-1)} \delta v;$$

i.e., the steady-state condition for D results in the Poiseuille profile with $v = 2$.

The less obvious example of using the PMED is the determination of the correcting factor a_1 in (16). We represent a_1 as

$$a_1(v) = a_{1\infty}\psi(v),$$

where $a_{1\infty} \equiv a_1(\infty)$ and the undetermined function $\psi(v)$ satisfies the following passages to the limits

$$\psi(v \longrightarrow 2) \longrightarrow v - 2 \longrightarrow 0, \quad \psi(v \longrightarrow \infty) \longrightarrow 1.$$

The simplest choice of a_1, which satisfies these conditions, has the form

$$a_1 = a_{1\infty} \frac{v-2}{v}. \qquad (19)$$

It turns out that the use of the PMED leads in this case to an expression that functionally coincides with relation (19). Indeed, upon substituting (16) into D and differentiating the result with respect to a_1, we obtain

$$a_1 = -\frac{v-2}{v} \frac{1 + (n-1)/(4v)}{1 + (n-1)(3v-2)/(4v)},$$

so that for the cylindrical geometry ($n = 1$)

$$a_1 = -\frac{v-2}{v}, \qquad (20)$$

which functionally coincides with (19). For the sake of clarity, we show in Fig. 1, for $n = 1$, the dependences of v and of the dimensionless dissipation $\overline{D} = \dfrac{D}{(\eta U^2)_0}$ on the dimensionless coordinate

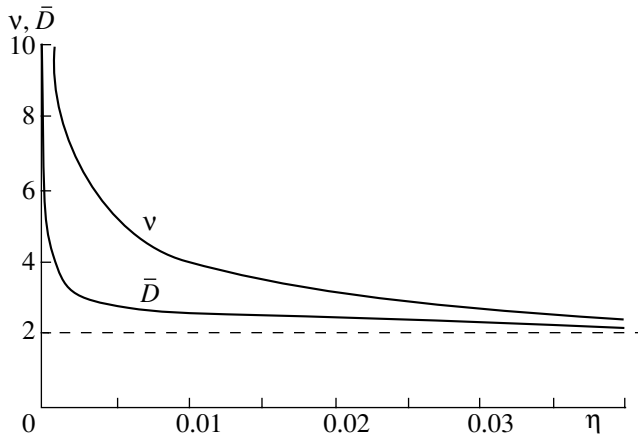$$\eta = \frac{1}{Re_0} \frac{z}{2a} \equiv \frac{\eta_0}{(\rho U)_0 2a} \frac{z}{2a}.$$

Figure.

Comparing this calculation of D with the traditional calculation [6] shows their good agreement. A considerably earlier passage to the asymptotic behavior of the quantity $D(\eta)$ than $\nu(\eta)$ (as well as all the remaining quantities) is a consequence of the PMED. From this, it follows that in specific tasks, near the stationary non-equilibrium state (the degree of closeness is seen in Fig. 1), the solution to the equation of energy can be replaced by the condition of constant dissipation.

4. We now consider the problem of stability for the process of heat release in a heat-conducting medium. In this case, the PMDF takes the form

$$F = \int\left[\int Q dK - \frac{(\nabla K)^2}{2}\right] dV, \tag{21}$$

where the conditions $Q > 0$ and $\dfrac{dQ}{dT} > 0$ correspond to the combustion process. The first variation of (21) is

$$\delta F = \int \delta K(\mathbf{q} d\mathbf{S}) + \int(-\text{div}\mathbf{q} + Q)\delta K dV,$$

from which the steady-state heat conduction equation follows

$$-\text{div}\mathbf{q} = \Delta K = -Q. \tag{22}$$

This equation was firstly solved in [7, 8] for the case $Q \sim \exp(\alpha T)$, with κ and $\alpha = $ const assuming the planar and cylindrical geometry (see also [9]); the absence of solutions to boundary value problems in [7, 8] was treated as an absolute instability. The same solutions based on group-theoretic considerations were obtained in [9, 10]. The variational statement (21) makes possible the use of the general method of analysis of stability based on the solution of the so-called Jacobi equation (see, e.g., [11]).

Restricting our consideration to the planar geometry, we have the argument $x \in (-d, d)$ and the even function $T(x) = T(-x)$. The boundary conditions are

$$T(-d) = T_-, \tag{23}$$

$$\frac{dT}{dx}(0) = 0. \tag{24}$$

Clearly, we also have

$$Q(T) = Q_- e^{\alpha(T - T_-)}$$

so that the dimensionless function is

$$\theta = \alpha(T - T_-) \in (0, \theta_0),$$

where θ_0 is to be determined. It is convenient to introduce the dimensionless argument

$$\xi = \left(\frac{\alpha Q_-}{2\kappa}e^{\theta_0}\right)^{1/2} x.$$

In this case, Eq. (22) takes the form

$$\theta_{\xi\xi} + 2e^{\theta - \theta_0} = 0, \tag{25}$$

and its solution is

$$\theta = \theta_0 - 2\ln\cosh\xi. \tag{26}$$

The condition for determining

$$\xi_0 = \left(\frac{\alpha Q_-}{2\kappa}e^{\theta_0}\right)^{1/2} d,$$

i.e., the quantity θ_0, is

$$\frac{\xi_0}{\cosh\xi_0} = \left(\frac{\alpha Q_-}{2\kappa}\right)^{1/2} d. \tag{27}$$

The Jacobi equation is the disturbed equation (25):

$$\tau_{\xi\xi} + 2\frac{\tau}{\cosh^2\xi} = 0, \tag{28}$$

where $\tau = \delta\theta$ [11]. Its general solution is

$$\tau = C_1\tau_1 + C_2\tau_2 \equiv C_1\tanh\xi + C_2(1 - \xi\tanh\xi), \tag{29}$$

with the constants being determined from the standard boundary conditions [11]

$$\tau(\mp\xi_0) = 0, \quad \frac{d\tau}{d\xi}(-\xi_0) = 1. \tag{30}$$

The final form of the solution for $\xi \in (-\xi_0, \xi_0)$ is given by the formula

$$\tau = \mp[\tau_2(\xi_0)\tau_1(|\xi|) - \tau_1(\xi_0)\tau_2(\xi)]. \tag{31}$$

The stability condition ($\delta^2 F > 0$) is reduced to the requirement

$$\tau > 0 \tag{32}$$

for $\xi \in (-\xi_0, \xi_0)$ [11]. We ascertain by direct substitution that condition (32) is satisfied only for

$$\tau_2(\xi_0) = 1 - \xi_0\tanh\xi_0 \geq 0, \tag{33}$$

so that the boundary of the stability domain is determined by the condition $\tau_2(\xi_0) = 0$.

The result expressed by relation (33) coincides with the stability criterion [7, 9], which follows from (27) and is obtained from the geometrically apparent condition

$$\frac{d}{d\xi_0}\frac{\xi_0}{\cosh\xi_0} = \frac{1}{\cosh\xi_0}(1 - \xi_0\tanh\xi_0) \geq 0.$$

In this example, the unsteady-state stage is described by the equation

$$h_t = \Delta K + Q(T),$$

where $h = \int \rho c\, dT$ and $K = \int \chi\, dh \left(\chi = \frac{\kappa}{\rho c}\right)$. Differentiating F [given by formula (21)] with respect to t yields

$$F_t + \int (K_t)_e (\mathbf{q}_e d\mathbf{S}) = -\int h_t K_t dV < 0,$$

so that for $(T_t)_e = 0$ or $\mathbf{q}_e = 0$, we have $F_t < 0$. This inequality is the necessary condition for the attainment of the steady state (minimum of F), but, as shown by this example, it is not the sufficient condition. The sufficient condition for the minimum of F is $\delta^2 F > 0$; it requires the solution to the Jacobi equation and its investigation. In conclusion, we note that the results of [5], where the variational principle was proposed for the unsteady-state nonlinear heat-conduction equation, allow a substantial extension. Indeed, if

$$E_2 \equiv \partial_t \theta_2 - K(\Delta\theta_2) = 0$$

is the heat-conduction equation for the potential θ_2 introduced by the relationship $h = \Delta\theta_2$ then we obtain from the variational principle [5] two equivalent equations

$$\partial_t E_2 \equiv \Delta[\partial_t^2 \theta_2 - \chi\Delta K(\Delta\theta_2)]$$
$$= \Delta(\partial_t \pm \chi\Delta)[\partial_t\theta_2 \mp K(\Delta\theta_2)] = 0.$$

From these equations, we find the desired equations

$$\partial_t\theta_2 \mp K(\Delta\theta_2) = 0, \tag{34}$$

which were obtained in [5] for the partial linear case $\chi = $ const. The same equations were also obtained in [12, 13], where the same linear case was studied. Thus, the parallel existence of two identical subsystems postulated in [13] with opposite directions of time is obtained here automatically for the general nonlinear case. The conclusion [5] that the total energy

$$H_2 = \Delta\partial_t\theta_2\frac{\partial}{\partial\Delta\partial_t\theta_2}\mathscr{L}_2 - \mathscr{L}_2$$
$$= [\partial_t\theta_2 + K(\Delta\theta_2)][\partial_t\theta_2 - K(\Delta\theta_2)]$$

vanishes in this case follows from (34) and is the consequence of the complete compensation of the energy dissipation in the system as a whole.

ACKNOWLEDGMENTS

REFERENCES

1. L. D. Landau and E. M. Lifshitz, *Course of Theoretical Physics*, Vol. 6: *Fluid Mechanics* (Nauka, Moscow, 1986; Pergamon, New York, 1987).

2. I. Prigogine, *Etude thermodynamique des phénomènes irréversibles* (Dunod, Paris, 1947).

3. S. R. de Groot and P. Mazur, *Nonequilibrium Thermodynamics* (North-Holland, Amsterdam, 1962; Mir, Moscow, 1964).

4. A. S. Pleshanov, Dokl. Akad. Nauk **378**, 38 (2001) [Dokl. Phys. **46**, 304 (2001)].

5. A. S. Pleshanov, Dokl. Akad. Nauk **371**, 175 (2000).

6. J. D. Campbell and K. Slattery, Trans. ASME, Ser. D **85** (1), (1963).

7. D. A. Frank-Kamenetskiĭ, Dokl. Akad. Nauk SSSR **18**, 411 (1938).

8. D. A. Frank-Kamentsetskiĭ, Zh. Fiz. Khim. **13**, 738 (1939).

9. Ya. B. Zel'dovich *et al.*, *Mathematical Theory of Combustion and Explosion* (Nauka, Moscow, 1980).

10. I. M. Gel'fand, Usp. Mat. Nauk **14** (2), 137 (1959).

11. I. M. Gelfand and S. V. Fomin, *Calculus of Variations* (Fizmatgiz, Moscow, 1961; Prentice-Hall, Englewood Cliffs, 1963).

12. L. Ya. Aĭnola, Inzh.-Fiz. Zh. **12**, 465 (1967).

13. P. M. Morse and H. Feshbach, *Methods of Theoretical Physics* (McGraw-Hill, New York, 1953; Inostrannaya Literatura, Moscow, 1958), Vol. 1.

Translated by A. Kozlenkov

════════════════════ **PHYSICS** ════════════════════

Generation of Gravitons in the Hot Uniform and Isotropic Universe

Corresponding Member of the RAS S. S. Gershtein, Academician A. A. Logunov, and M. A. Mestvirishvili

The problem of the possibility of generating gravitons in the Universe was thoroughly studied in [1, 2]. In [2], the formula was derived for the graviton generation rate in the uniform and isotropic Universe

$$\frac{1}{\sqrt{-g}}\frac{d}{dt}(\sqrt{-g}\,n_g) = \frac{1}{288\pi}R^2 \qquad (1)$$

under the assumption that

$$\frac{R^2}{R_{\rho\lambda\mu\nu}R^{\rho\lambda\mu\nu}} \ll 1, \qquad (2)$$

where R is the scalar curvature and $R_{\rho\lambda\mu\nu}$ is the Riemannian curvature tensor.

For the radiation-dominant evolution stage of the hot Universe, the equation of state

$$p = \frac{1}{3}\rho c^2 \qquad (3)$$

holds. Since, according to the general relativity theory (GRT), the scalar curvature R is exactly zero at this stage of the Universe's evolution, the authors of [1, 2] concluded that in the hot and uniform Universe the generation of gravitons does not occur. In [1], it was also noted that the generation of gravitons apparently prohibits isotropic singularities in the vicinity of which the equation of state

$$p > \frac{1}{3}\rho c^2 \qquad (4)$$

takes place. Such a conclusion evidently arose due to the fact that in this case the scalar curvature R would become as large as is wished. Therefore, an extremely intense graviton generation must occur, which, in the case of the existence of a singularity, could lead to an inconsistency with modern data on the density of matter in the Universe.

––––––––––––

Institute of High-Energy Physics, Protvino, Moscow oblast, 142284 Russia
E-mail: gershtein@mx.ihep.su; logunov@mx.ihep.su; filimonova@th1.ihep.su

In the relativistic gravitational theory (RGT) considering the gravitational field as a physical field with a spin of 2 or 0, which evolves in the Minkowski space, the completely opposite situation arises: the evolution of the uniform and isotropic Universe is described by other equations [3, 4]. It is extremely important to emphasize that, in this case, no singularities are present:

$$\frac{1}{a}\frac{d^2a}{d\tau^2} = -\frac{4\pi G}{3}\left(\rho + \frac{3p}{c^2}\right) - 2\omega\left(1 - \frac{1}{a^6}\right), \qquad (5)$$

$$H^2 \equiv \left(\frac{1}{a}\frac{da}{d\tau}\right)^2 = \frac{8\pi G}{3}\rho - \frac{\omega}{a^6}\left(1 - \frac{3a^4}{a_{\max}^4} + 2a^6\right). \qquad (6)$$

Here,

$$\omega = \frac{1}{12}\left(\frac{mc^2}{\hbar}\right)^2, \qquad (7)$$

and m is the graviton mass.

As follows from these equations (see [3, 4]), for the radiation-dominant stage of the Universe's evolution and for small values of the scaling factor $a(\tau)$, the equation is valid

$$\frac{\ddot{a}}{a} + \left(\frac{\dot{a}}{a}\right)^2 = \frac{\omega}{a^6}, \quad \dot{a} = \frac{da}{d\tau}. \qquad (8)$$

In the GRT, the left-hand side of Eq. (8) is exactly zero in the radiation-dominant region. Therefore, at this stage of the Universe's evolution, the Fridman stage takes place when the scaling factor $a(\tau)$ varies with time according to the $\sqrt{\tau}$ law. In the RGT, according to Eq. (8), the pre-Fridman stage of the Universe's evolution exists in the radiation-dominant phase. Here, the scalar curvature for the uniform and isotropic Universe is

$$R = -\frac{6}{c^2}\left[\frac{\ddot{a}}{a} + \left(\frac{\dot{a}}{a}\right)^2\right]. \qquad (9)$$

On the basis of Eq. (8), we have

$$R = -\frac{1}{2}\left(\frac{mc}{\hbar}\right)^2 \frac{1}{a^6}. \tag{10}$$

From Eq. (6), it follows that the scaling factor $a(\tau)$ cannot turn into zero, and its minimum value equals

$$a_{\min} = \left(\frac{\rho_{\min}}{2\rho_{\max}}\right)^{1/6}, \tag{11}$$

where

$$\rho_{\min} = \frac{1}{16\pi G}\left(\frac{mc^2}{\hbar}\right)^2, \tag{12}$$

while in fact the maximum density $\rho_{\max}$ of matter in the gravitational field is an integral of motion, which is not determined theoretically.

Based on relationships (10)–(12), we may conclude that, at the time moment when the maximum density of matter is attained, the scalar curvature of effective Riemannian space takes the value

$$R = -\frac{16\pi G}{c^2}\rho_{\max}. \tag{13}$$

At this time moment, the Hubble constant H is exactly zero. We can see from formula (13) that, in contrast to GRT, in the RGT the scalar curvature R in the radiation-dominant stage of the Universe's evolution does not turn into zero. Moreover, it may be sufficiently large, since it is determined by the maximum density of matter $\rho_{\max}$ in the gravitational field.

Thus, according to the RGT, in the radiation-dominant phase of the Universe's evolution, there is a pre-Fridman stage in which the scalar curvature not only differs from zero but may be sufficiently large, since it is determined by the maximum density $\rho_{\max}$ of matter. In order to find the graviton generation rate, we cannot apply formula (1), because it was derived in approximation (2), which is not fulfilled in our case.

If, based on dimensional concepts, we assume, in the general case, the graviton generation rate to be dependent only on the quantities

$$R^2, \ R_{\rho\lambda\mu\nu}R^{\rho\lambda\mu\nu}, \tag{14}$$

then a time interval should be chosen during which the Hubble constant attains its maximum, since the Fridman stage arises very soon. It can be easily found from Eqs. (5), (6) that the Hubble constant H attains its maximum at a time moment when the scaling factor $a(\tau)$ is

$$a^2(\tau) = \frac{3}{2}a_{\min}^2. \tag{15}$$

Employing relation (15), we find from Eqs. (6) the

maximum value of the Hubble constant

$$H_{\max} = 3^{-2}(32\pi G\rho_{\max})^{1/2}. \tag{16}$$

At the time moment when H attains its maximum, the scalar curvature is

$$R = -\left(\frac{2}{3}\right)^3 \times 16\pi G\frac{\rho_{\max}}{c^2} \tag{17}$$

and the ratio $\dfrac{\ddot{a}}{a}$ is determined by the expression

$$\left(\frac{\ddot{a}}{a}\right) = 3^{-4} \times 32\pi G\rho_{\max}. \tag{18}$$

The invariant obtained by the convolution of the curvature tensor for the metric of a uniform and isotropic Riemannian space is

$$R_{\rho\lambda\mu\nu}R^{\rho\lambda\mu\nu} = \frac{12}{c^4}\left[\left(\frac{\ddot{a}}{a}\right)^2 + \left(\frac{\dot{a}}{a}\right)^4\right]. \tag{19}$$

Substituting Eqs. (16), (18) into this expression, we arrive at

$$R_{\rho\lambda\mu\nu}R^{\rho\lambda\mu\nu} = 8 \times 3^{-7}\left(\frac{32\pi G}{c^2}\rho_{\max}\right)^2. \tag{20}$$

It should be noted that the Hubble constant varies from zero to the maximum value $H_{\max}$, which is determined by formula [16] during a rather short time interval equal to [3, 4]

$$\tau = \left(\frac{3}{32\pi G\rho_{\max}}\right)^{1/2}\left[\frac{\sqrt{3}}{2} + \ln\left(\sqrt{\frac{3}{2}} + \sqrt{\frac{1}{2}}\right)\right]. \tag{21}$$

If the graviton generation rate is determined by quantities (14), then during time interval (21) a sufficiently large amount of gravitons can be generated, provided that the density $\rho_{\max}$ is reasonably high. However, if it is much lower than the Planck density, this implies that the generated gravitons immediately become free, while their energy further decreases due to the red shift.

Thus, a gravitational relict background of nonthermal origin must arise. The gravitons interact with each other sufficiently strongly, since their interaction constant is equal to unity. In the case of a sufficiently high density of the gravitons, this fact can violate the uniformity of the relict gravitational background having a nonthermal origin. From dimensional considerations, the total number per cubic centimeter of generated grav-

itational-field quanta is proportional to the quantities

$$cR^2\tau, \quad c(R_{\rho\lambda\mu\nu}R^{\rho\lambda\mu\nu})\tau, \tag{22}$$

where the quantities R_2, $R_{\rho\lambda\mu\nu}R^{\rho\lambda\mu\nu}$, and τ are given by expressions (17), (20), and (21). It follows from these formulas that the graviton generation rate in the hot radiation-dominant phase of Universe evolution is determined, basically, by the value of the maximum matter density ρ_{max}. Being informed about the process of the graviton generation in more detail, we would be able to determine the maximum value of the matter density intrinsic to the Universe in the present expansion cycle. On the other hand, we can formulate the following hypothesis: the gravitational background of nonthermal origin could be a dark matter that manifests itself in the Universe as a missing mass. However, this hypothesis requires a more thorough analysis.

REFERENCES

1. L. P. Grishchuk, Zh. Éksp. Teor. Fiz. **67**, 825 (1974) [Sov. Phys. JETP **40**, 4009 (1975)].

2. Ya. B. Zel'dovich and A. A. Starobinskiĭ, Pis'ma Zh. Éksp. Teor. Fiz. **26**, 373 (1977) [JETP Lett. **26**, 252 (1977)].

3. S. S. Gershtein, A. A. Logunov, and M. A. Mestvirishvili, Yad. Fiz. **61**, 1526 (1998) [Phys. At. Nucl. **61**, 1420 (1998)].

4. A. A. Logunov, *Theory of Gravitational Field* (Nauka, Moscow, 2000).

Translated by G. Merzon

<hr>

=========================== **PHYSICS** ===========================

Specific Character of Critical Behavior in a Finite-Size System: A Model with the Landau Effective Hamiltonian

N. M. Kortsenstein* and A. L. Tseskis**

Presented by Academician V.P. Skripov June 1, 2001

Received June 28, 2001

We show that the problem on the critical behavior in a three-dimensional model with the Landau effective Hamiltonian can be solved exactly if a certain inequality is fulfilled. For a system with sufficiently small sizes (specified by this inequality), we calculate critical indices and a shift of the heat-capacity maximum with respect to its position in the thermodynamic limit. The shift is also calculated for systems of noncubic shape. If the space dimension exceeds an upper critical value, the results turn out to be exact in the thermodynamic limit since the model under consideration is renormalizable in this case.

1. As a rule, exact results of statistical mechanics have an asymptotic character. This implies the passage to the thermodynamic limit (i.e., to the number of particles N tending to infinity) in the corresponding calculations. In this case, the results concerning macroscopic systems with the number of particles (or degrees of freedom) on the order of Avogadro's number are virtually exact by virtue of the smallness of fluctuations determined by values on the order of $N^{-1/2}$. This concerns the temperatures of various phase transitions and, for example, the phase interfaces in the first-order transitions or the coinciding sharp (possibly, infinite) peaks of the heat capacity, susceptibility, etc., in the second-order transitions. On the contrary, if N is not too large, the fluctuations are not small and the second order transitions are smeared over a certain temperature interval. In this case, singularities of physical quantities are smoothed, and the extrema are shifted with respect to their positions for infinite N. Recently, such effects were studied in numerous experiments (see, for example, [1, 2]). As to their theoretical description, it is reduced to finding corrections to exact solutions for discrete models with finite (but large!) numbers N [3, 4] or to extrapolating the results obtained for $d \geq 4$ to the physical dimension $d = 3$ by ε-expansion within the

framework of a continuous model [5]. It should be noted that the volume V of the system, rather than the number N, must be considered in the continuous model.

Here, we report exact results for the continuous model with the Landau effective Hamiltonian, which are valid only for systems with small sizes. It should be noted beforehand that we ignore surface effects in finite systems. In contrast to [5], we consider the case of $d = 3$, with no extrapolation used, and directly calculate the heat capacity c_p. For finite systems, the critical temperature is identified with the maximum point for c_p. In fact, this result is reduced to finding a correction to the Landau theory, which occurs due to the zero-mode fluctuation. In the theoretically important case of $d \geq 4$, we also show that the results obtained remain exact in the thermodynamic limit.

2. Within the framework of the continuous model, investigating the vicinity of the second-order phase-transition temperature is reduced to calculating a fluctuation correction to the thermodynamic potential (the so-called singular part of the potential) [6]:

$$\Phi_{\text{sing}} = -T \ln Z.$$

Here, the statistical integral Z corresponds to the summation over all possible distributions of the field η in the volume L^d (d is the space dimension):

$$Z = \int \exp\left\{ -\frac{H(\eta)}{T} \right\} \mathcal{D}\eta. \tag{1}$$

We start from the Landau effective Hamiltonian H_{eff}, which takes the following form in terms of the Fourier transform of the field η ($t = T - T_c$, $V = L^d$):

$$H_{\text{eff}} = V\left(at \sum_{\mathbf{k}} \eta_{\mathbf{k}}^2 \right.$$
$$\left. + b \sum_{\mathbf{k}_1, \mathbf{k}_2, \mathbf{k}_3} \eta_{\mathbf{k}_1} \eta_{\mathbf{k}_2} \eta_{\mathbf{k}_3} \eta_{-\mathbf{k}_1 - \mathbf{k}_2 - \mathbf{k}_3} + g \sum_{\mathbf{k}} \mathbf{k}^2 \eta_{\mathbf{k}}^2 \right). \tag{2}$$

_____

* *Joint Institute for High Temperatures,*
  Russian Academy of Sciences,
  ul. Izhorskaya 13/19, Moscow, 127412 Russia
** *Krzhizhanovskiĭ Power Engineering Institute,*
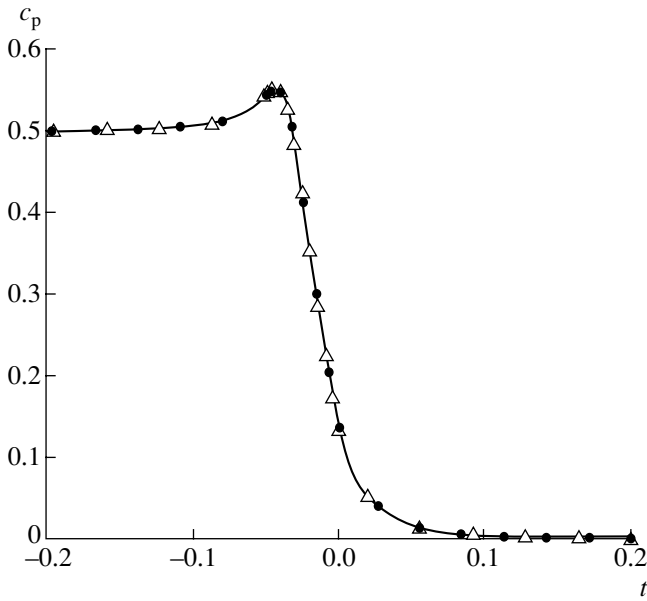 *Leninskiĭ pr. 19, Moscow, 117927 Russia*

Fig. 1. Temperature dependence of the heat capacity (in dimensionless units) for various ways of representing the fourth-order terms h_4 in H_{eff}: ($\triangle$) $h_4 = h_4^{(1)}$, ($\bullet$) $h_4 = h_4^{(2)}$; solid line corresponds to one degree of freedom.

As $V \longrightarrow \infty$, the number of degrees of freedom in the model tends to infinity $\left(n = \left(\dfrac{K}{2\pi}\right)^d V \right.$, where K is the cutoff parameter $\left.\right)$. To describe a finite-size system in the case of $d = 3$, we consider the field in the volume L^3 such that the following inequality holds for a nonzero wave number κ with the smallest modulus:

$$g\left(\frac{\kappa}{b}\right)^{1/2} \gg 1. \tag{3}$$

It is evident that this inequality is also fulfilled for all the components with nonvanishing k. Taking into account that $\kappa \sim \dfrac{1}{L}$, we also have that $\dfrac{g}{(bL)^{1/2}} \gg 1$. It is easy to see that the contribution of the regions with nonvanishing $\eta_{k \neq 0}$ into the statistical integral is negligible if these inequalities are fulfilled. Under these conditions, average values of physical quantities are also independent of the particular form of the terms of the fourth order in η, which enter into H_{eff}. This statement is confirmed by the calculation of the heat capacity (see necessary relationships below) of the system with three degrees of freedom, with the fourth-order term simulated by two various polynomials of the fourth degree:

$$h_4^{(1)} = \eta_0^4 + \eta_1^4 + \eta_2^4 + \eta_0^2\eta_1^2 + \eta_0^2\eta_2^2 + 2\eta_1^2\eta_2^2,$$

$$h_4^{(2)} = \eta_0^4 + \eta_1^4 + \eta_2^4 + \eta_0^2\eta_1^2 + \eta_0^2\eta_2^2 + \eta_1^2\eta_2^2 + \eta_0^2\eta_1\eta_2.$$

The calculations were carried out with the following values of parameters: $L = 20$, $a = b = T_c = 1$, and $g = 100$. The results are presented in Fig. 1. In the same figure, we also show the calculation results for the heat capacity of the system with one degree of freedom, η_0 (for the same values of the parameters). As is seen from Fig. 1, the points corresponding to all the cases under consideration are in the same curve.

Thus, when describing the phase transition in a system with sufficiently small sizes, we can only consider a system with one degree of freedom. Such a problem corresponds to spatially homogeneous fluctuations and can be solved exactly. We also note that solving this problem is interesting by itself, serving as a formal example of an exactly solvable model of the second-order phase transition. It is evident that this model corresponds to the correction to the Landau theory, which is due to spatially homogeneous (with $k = 0$) fluctuations. Omitting the subscript in the component η_0, we write out the effective Hamiltonian in the form (as before, $a = b = T_c = 1$)

$$H = V(t\eta^2 + \eta^4). \tag{4}$$

Twice differentiating the singular part of the potential with respect to the temperature t, with H_{eff} given by (4), we obtain the following expression for the heat capacity per unit volume:

$$c_p = \frac{\langle H^2 \rangle - \langle H \rangle^2}{V}.$$

Performing the change of variables $V\eta^4 = x^4$ and introducing the denotation $tV^{1/2} = \xi$, we arrive at

$$c_p = \frac{\int\limits_{-V^{1/4}}^{V^{1/4}} x^4 \exp\{-\xi x^2 - x^4\}dx}{\int\limits_{-V^{1/4}}^{V^{1/4}} \exp\{-\xi x^2 - x^4\}dx}$$

$$- \left(\frac{\int\limits_{-V^{1/4}}^{V^{1/4}} x^2 \exp\{-\xi x^2 - x^4\}dx}{\int\limits_{-V^{1/4}}^{V^{1/4}} \exp\{-\xi x^2 - x^4\}dx}\right)^2. \tag{5}$$

For sufficiently large ξ, evaluating integrals in (5) by the saddle-point method is reduced to integration over the vicinity of the minimum for H_{eff} in the exponent, i.e., of the point $x = 0$. Hence, in the high-temperature
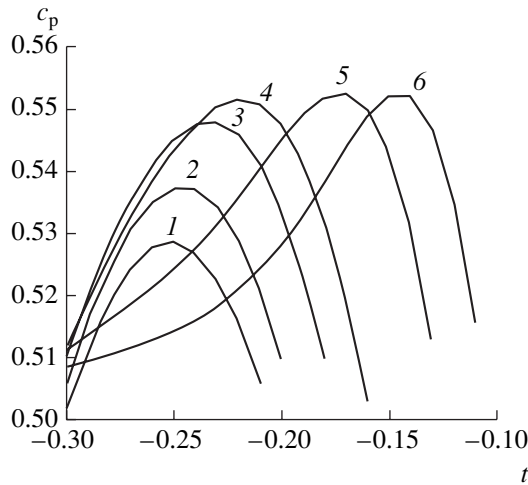
Fig. 2. Temperature dependence of the heat capacity for small ($L \le 9$) sizes of the system: $L =$ (*1*) 5.8, (*2*) 6, (*3*) 6.4, (*4*) 6.8, (*5*) 8, and (*6*) 9.
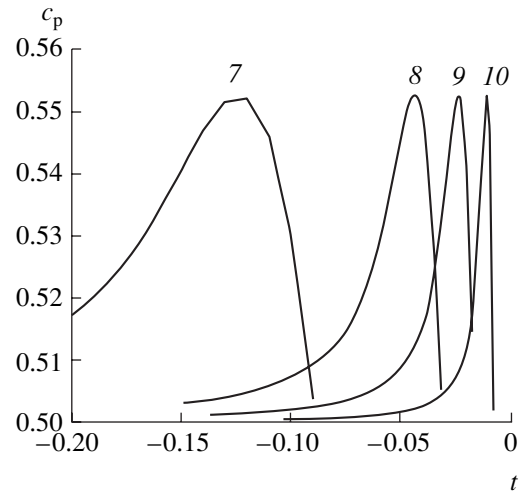

Fig. 3. Temperature dependence of the heat capacity for $L \ge$ 10: $L =$ (*7*) 10, (*8*) 20, (*9*) 30, and (*10*) 50.

region ($t > 0$), the heat capacity c_p decreases, tending to zero with increasing t. For $t = 0$ ($\xi = 0$),

$$c_p = \frac{\Gamma(1/4)\Gamma(5/4) - \Gamma^2(3/4)}{\Gamma^2(1/4)} = 0.135763.$$

In this case, the derivative $\dfrac{\partial c_p}{\partial t}$ is negative and proportional to $V^{1/2}$. In the low-temperature phase ($t < 0$), with the help of the change of variables $-\xi^2 = y^2$, the quantity c_p is transformed to a form in which the exponent in the integrands is $y^2 - \dfrac{y^4}{\xi^2}$, while the right-hand side of Eq. (5) is additionally multiplied by ξ^{-2}. For sufficiently large but finite ξ^2 (in any case, $\xi^2 > 1$), it is easy to prove that the contribution of $\dfrac{\partial(\xi^{-2})}{\partial t}$ into the derivative of c_p with respect to t is essential, being positive and proportional to $V^{1/2}$. Thus, the curve of the heat capacity must have a maximum at a certain point t_m in the region $-AV^{-1/2} < t < 0$ (A is a constant). By virtue of the finiteness of ξ, this maximum is finite and independent of V; however, the tangents to the curve on both sides of this point become vertical as $V \longrightarrow \infty$.

The calculation results for the heat capacity are shown in Figs. 2–4. Figures 2 and 3 display the variation in the heat-capacity behavior (in its temperature dependence) with increasing sizes of the system. It is worth noting that while decreasing t in the low-temperature phase, the heat capacity tends to a value of 0.5. This value is evidently determined by the order parameter minimizing H_{eff} in the exponent. Thus, the difference $c_p(-\infty) - c_p(\infty)$ is the heat-capacity jump in the

Landau theory $\left(\Delta c_p = \dfrac{a^2 T_c}{2b} \text{ in conventional units} \right)$. In this case, both the shape of the curves and its variation with an increase in L are in a qualitative agreement with experimental data [1, 2] for systems with small L. (It is interesting to note that, for systems with a small number of particles, a similar behavior of the heat capacity is possible even if the phase transition is not of the second order [7].) In particular, it can be seen from Fig. 2 that the heat-capacity maximum increases with L for the sufficiently small L for which the approximation
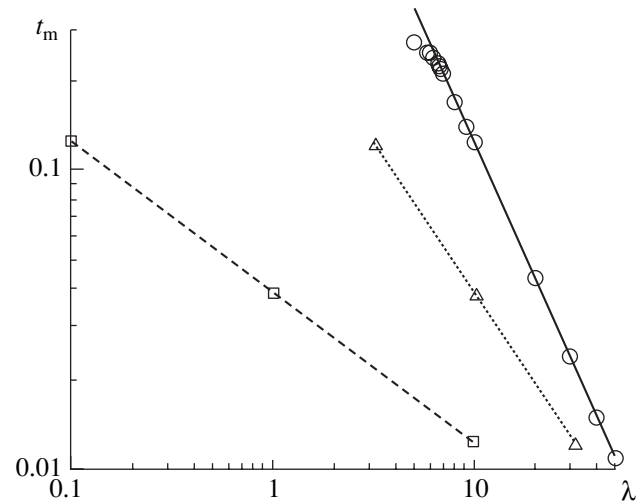

Fig. 4. Temperature t_m corresponding to the heat-capacity maximum as a function of size and geometry of the system: ($\circ$) cubic geometry, positions of the maxima in curves *1–10* of Figs. 2 and 3; (solid line) the dependence $t_m = -3.875\lambda^{-1.498}$; ($\triangle$) lengthy geometry; (dotted line) the dependence $t_m = -0.39175\lambda^{-1}$; ($\square$) flat geometry; and (dashed line) the dependence $t_m = -0.039175\lambda^{-0.5}$.

under consideration is immediately applicable. The dependence of the maxima t_m of curves *1–10* in Figs. 2 and 3 on the size of the system is shown in Fig. 4. As is seen, the corresponding points approach the curve (in this case, $\lambda \equiv L$)

$$t_m = -3.875 L^{-1.498}$$

with increasing L. The fact that the exponent slightly differs from 3/2 is associated with the limited computational accuracy of the numerical integration. Since t_m tends to zero from below as $V \longrightarrow \infty$, the shift in the critical temperature with respect to its value in the thermodynamic limit is given by the universal dependence

$$T_c(L) - T_c(\infty) = \text{const} L^{-3/2}, \qquad (6)$$

with the constant determined above. It should be noted that, in general, the dependence on the size of a finite system in the critical region (finite-size scaling), as well as the shift in the position of the heat-capacity maximum with a variation in the size, is a characteristic of the critical behavior of finite-size systems. Thus, in the case under consideration as well as when solving the two-dimensional Ising model, the corresponding relationships can be established exactly, in contrast to the case considered in [8], for example, where such relationships are fairly indefinite. In the case under consideration, L is a unique quantity with the dimension of length. Hence, the exponent in the relationship $t_m \sim L^{-3/2}$ has to be immediately related to the critical index ν; therefore, $\nu = 2/3$. It is not difficult to find the remaining (temperature) indices. It is evident that $\alpha = 0$ and $\beta = 1/2$. For finding the susceptibility index, we differentiate Φ_{sing} with respect to t. As a result, the mean square of fluctuations in the volume V at $t = 0$ is

$$\left\langle \int \eta^2 dV \right\rangle \sim V^{1/2}.$$

Taking into account that $L \sim t^{-2/3}$, we find that $\gamma = 1$; hence, $\zeta = 1/2$. The above results concerning systems with the cubic geometry can be extended to other systems, for example, to lengthy systems having the shape of a rectangular parallelepiped $L \times \lambda \times \lambda$ or to plane systems, $L \times L \times \lambda$, with $L \gg \lambda$. It is found for these cases,

$$t_m(\lambda) \sim \frac{\lambda^{-1}}{\sqrt{L}} \quad \text{and} \quad t_m(\lambda) \sim \frac{\lambda^{-1/2}}{L},$$ respectively, with t_m

being the absolute value of the corresponding quantity. The numerical results are shown in Fig. 4. Thus, the shift in the critical temperature is determined by the shape of a system as well as its size. This conclusion is in qualitative agreement with the experimental data.

3. In conclusion, we make the following notes. In the case of $d = 3$, the results listed above have a direct physical sense, provided that, of course, the inequalities

indicated at the beginning of this paper are fulfilled. As was noted above, the extrapolation of the results to large L is of methodical interest. In the space with a dimension $d \geq 4$, these results are exact just in the thermodynamic limit, which can be proved by the following manner. Using the change of variables $\eta_k L^{d/4} = x_k$, with regard to $tL^{d/2} \sim 1$, we exclude the quantity L from the two first sums in the effective Hamiltonian (2). The last sum proportional to g takes the form

$$g L^{d-2} \sum_k k^2 x_k^2;$$

hence, the corresponding term is not small even for the smallest $k \sim L^{-1}$. With regard to the representation of the Dirac δ function in the form

$$\delta(z) = \lim_{s \to \infty} \frac{s}{\pi} \exp(-s^2 z^2),$$

it is evident that a product of the Dirac δ-functions,

$\prod_k \delta(k)$, enters into the functional-integration element

in the statistical sum, while the corresponding additional factor independent of t yields a negligible additive term to Φ_{sing} after taking the logarithm. Thus, the field components with nonzero k are eliminated. Therefore, in the case of $d \geq 4$, the consideration similar to that carried out above for $d = 3$ becomes exact as $L \longrightarrow \infty$. This is evidence of the renormalizability of the model η^4 for $d \geq 4$. The consideration gives, as it must be, the values of indices coinciding with those in the model of free field: $\alpha = 0$, $\beta = 1/2$, $\gamma = 1$, $\nu = 1/2$, and $\zeta = 0$.

REFERENCES

1. J. A. Nissen, T. C. P. Chui, and J. A. Lipa, Physica B (Amsterdam) **194**–**196**, 615 (1994).
2. S. Mehta, M. O. Kimball, and F. M. Gasparini, J. Low Temp. Phys. **114**, 467 (1999).
3. M. E. Fisher and F. E. Ferdinand, Phys. Rev. Lett. **19**, 169 (1967).
4. A. L. Tseskis, Zh. Éksp. Teor. Fiz. **106**, 1089 (1994) [JETP **79**, 591 (1994)].
5. E. Brezin and J. Zinn-Justin, Nucl. Phys. B **257**, 867 (1985).
6. L. D. Landau and E. M. Lifshitz, *Course of Theoretical Physics*, Vol. 5: *Statistical Physics* (Nauka, Moscow, 1976; Pergamon, Oxford, 1980), Part 1.
7. S. V. Shevkunov, Dokl. Akad. Nauk **376**, 318 (2001) [Dokl. Phys. **46**, 12 (2001)].
8. V. Privman, Physica A (Amsterdam) **177**, 241 (1991).

Translated by V. Bukhanov

=========================== **PHYSICS** ===========================

Development of the Thermodynamic Theory for the Linear Magnetoelectric Effect in Cr_2O_3 Antiferromagnet

S. S. Krotov and A. V. Lisnyak

Presented by Academician Yu.A. Osip'yan June 28, 2001

The concept of magnetic symmetry [1] served as a basis for the statement on the principle possibility of the existence of the magnetoelectric (ME) effect. Furthermore, specific predictions of the ME effect in the Cr_2O_3 antiferromagnet were made [2].

Recently, the ME effect was experimentally discovered in the polydomain Cr_2O_3 crystal [3]. Later, more exact experiments [4] revealed an anisotropy in the ME effect, and the first microscopic theory of the ME effect appeared [5].

All subsequent microscopic theories followed the initial assumption that, under the action of the electric field **E**, a certain parameter of the spin Hamiltonian changes, namely, the axial term (*D*-term) quadratic in spins [5], isotropic exchange [6], *g*-factor [7], antisymmetric exchange [8], and biquadratic exchange [9]. The temperature-averaged terms entering into the expressions for the components α_{ij} of the ME susceptibility tensor that determines the linear ME effect were calculated basically by three methods. These methods imply the approximation of the molecular field [5], the allowance for the experimentally determined temperature dependence of magnetic susceptibility [8], and the Green's function method [10].

The magnetic susceptibility tensor α_{ij}, which determines the linear ME effect, does not possess any internal symmetry. However, it should be invariant under the action of operations of crystal magnetic-symmetry point groups. In particular, this statement is true for the point group of the Cr_2O_3–$\bar{3}'m'$ magnetic symmetry (the prime implies the operation of the time inversion). As a result, the matrix acquires the form

$$\alpha_{ij} = \begin{pmatrix} \alpha_\perp & 0 & 0 \\ 0 & \alpha_\perp & 0 \\ 0 & 0 & \alpha_\parallel \end{pmatrix}$$

(the *z*-axis coincides with the axis of the third order).

The authors of [8], after comparing the refined theory with available experimental data, made a conclusion that the temperature dependence of $\alpha_\perp$ in Cr_2O_3 is best described by the mechanism of the single-ion (spin-orbital) type. At the same time, for $\alpha_\parallel$, the best agreement with the experimental data in the high-temperature and low-temperature regions is provided by the double-ion (isotropic exchange) and single-ion (*g*-factor variation) mechanisms, respectively.

However, it is unlikely that any particular microscopic theory of the ME effect can be considered to be completely satisfactory. Difficulties arise due to the impossibility of error estimation while calculating the temperature-averaged quantities that are present in the theory. The Green's-function method [10], in principle, must give more precise results. However, the discrepancy in the values of $\alpha_\perp$ predicted on the basis of different versions of the theory (the random-phase approximation and Callen decoupling) is comparable with the divergence between these versions, on one hand, and predictions of the molecular-field approximation, on the other hand.

Meanwhile, the simple development of the phenomenological theory makes it possible to obtain a result that can describe the temperature dependence of $\alpha_\parallel$ and $\alpha_\perp$ within a wide temperature range. In this case, the true behavior (i.e., the behavior consistent with experimental data) is provided as *T* tends to zero, as well as in the spin-flop phase. The development of the theory is the goal of this paper.

The construction of the thermodynamic theory describing the ME effect in antiferromagnets starts from the consideration of a certain nonequilibrium thermodynamic potential, e.g., the Gibbs potential

$$G = G_0 - \frac{1}{2}k_{ij}E_iE_j - \frac{1}{2}\chi_{ij}H_iH_j - \alpha_{ij}E_iH_j,$$

where G_0 is independent of the components of the **H**- and **E**-fields (indices *i* and *j* determine Cartesian *x*-, *y*-,

Moscow State University,
Vorob'evy gory, Moscow, 119899 Russia

and z-axes; the summation over recurring indices is implied). The relations

$$\mathbf{P} = -\frac{\partial G}{\partial \mathbf{E}}, \quad \mathbf{M} = -\frac{\partial G}{\partial \mathbf{H}} \tag{1}$$

result in the following material equations:

$$
\begin{aligned}
P_i &= k_{ij}E_j + \alpha_{ij}H_j, \\
M_i &= \chi_{ij} + \alpha_{ji}E_j.
\end{aligned} \tag{2}
$$

In order to solve the problem formulated above, we write out the Gibbs potential in the form of the expansion into a series of the antiferromagnetism vector $\mathbf{L}$ and its components including powers to the sixth order:

$$
\begin{aligned}
G = {}& G_0 + \frac{1}{2}A\mathbf{L}^2 + \frac{1}{2}B\mathbf{M}^2 + \frac{1}{2}D(\mathbf{LM})^2 + \frac{1}{4}CL^4 \\
&+ \frac{1}{6}IL^6 + \frac{1}{2}A'(L_x^2 + L_y^2) + \frac{1}{4}C'(L_x^2 + L_y^2)^2 \\
&+ \frac{1}{6}I'(L_x^2 + L_y^2)^3 + \frac{1}{4}KL_z(3L_x^2 L_y - L_y^3) \\
&+ \frac{1}{6}R_1(L_x^3 - 3L_x L_y^2)^2 + \frac{1}{6}R_2(3L_x^2 L_y - L_y^3)^2 \\
&+ \frac{1}{6}K'L^2 L_z(3L_x^2 L_y - L_y^3) - (\mathbf{MH})
\end{aligned} \tag{3}
$$

(the z-axis of the Cartesian coordinate system is aligned along the symmetry axis of the third order; the x-axis coincides with that of the second-order axes).

Minimizing relation (3) over $\mathbf{M}$ for a given $\mathbf{L}$, we arrive at

$$\mathbf{M} = \chi_\perp \mathbf{H} - (\chi_\perp - \chi_\parallel)\frac{(\mathbf{LH})}{\mathbf{L}^2}\mathbf{L}, \tag{4}$$

where

$$\chi_\perp = \frac{1}{B}, \quad \chi_\parallel = (B + DL^2)^{-1}.$$

We now introduce several definitions:

$$\mathbf{L} = L\mathbf{l},$$

$\mathbf{l} = \{\cos\phi\sin\theta, \sin\phi\sin\theta, \cos\theta\}$ is the unit vector in the spherical coordinate system;

$$\mathbf{H} = \{H_\perp\cos\psi, H_\perp\sin\psi, H_\parallel\}$$
$$= H\{\cos\psi\sin\nu, \sin\psi\sin\nu, \cos\nu\}.$$

Using these definitions, as well as relation (4), and ignoring the isotropic terms of the form $\frac{A}{2}\mathbf{L}^2$, which are unessential in considering the spin flop, we can rewrite series (3) in the form

$$
\begin{aligned}
G = {}& G_0 - \frac{1}{2}\chi_\perp H^2 + \frac{1}{2}(\chi_\perp - \chi_\parallel)(\mathbf{lH})^2 + \frac{A'}{2}L^2\sin^2\theta \\
&+ \frac{C'}{4}L^4\sin^4\theta + \frac{I'}{6}L^6\sin^6\theta + \frac{K}{4}L^4\cos\theta\sin^3\theta\sin3\phi
\end{aligned}
$$

$$+ \frac{K'}{6}L^4\cos\theta\sin^3\theta\sin3\phi$$

$$+ \left[\frac{R_1}{6}\cos^2 3\phi + \frac{R_2}{6}\sin^2 3\phi\right]L^6\sin^6\theta.$$

Minimization of this expression over ϕ under the condition $H_\parallel^2 > H_c^2 = \frac{A'L^2}{\chi_\perp - \chi_\parallel}$ (H_c is the threshold field of the spin-flop transition for $H_\perp = 0$) determines the position of the vector $\mathbf{L}$ in the spin-flop phase. It is easy to see that if $\theta = \frac{\pi}{2}$, then it is determined by the roots of the following equation

$$\sin6\phi = 0. \tag{5}$$

On the other hand, the presence in series (3) of the term $\frac{1}{4}KL_z(3L_x^2 L_y - L_y^3)$ results in the violation of the rigorous inequality $\theta = \frac{\pi}{2}$ in the spin-flop phase, even if $\nu = 0$ is the incomplete spin flop. With allowance for this fact, Eq. (5) is replaced by the new equation

$$\sin3\phi = \frac{3}{2R'}\left(\frac{K}{4}\frac{1}{L^2} + \frac{K'}{6}\right)\frac{\cos\theta}{\sin^3\theta}, \quad R' = \frac{R_1 - R_2}{2}.$$

Thus, we can consider that $\phi \approx 0$; i.e., the vector $\mathbf{L}$ is directed along one of the light axes in the (x, y)-plane [11].

A part of the Gibbs potential, which corresponds to ME interactions, with the invariants of both the first [12] and the third power (in the components of the vector $\mathbf{L}$) taken into account, is written as

$$
\begin{aligned}
G_{ME} = {}& -\Lambda^{(1)}E_z(\mathbf{LM}) - \Lambda^{(3)}E_z\mathbf{L}^2(\mathbf{LM}) \\
&- \lambda_1\{L_x(E_xM_y + E_yM_x) + L_y(E_xM_x - E_yM_y)\} \\
&\times [1 + kL^2 + r(L_x^2 + L_y^2)] \\
&- \lambda_2 E_z(L_xM_x + L_yM_y)[1 + eL^2 + f(L_x^2 + L_y^2)] \\
&- \lambda_3 L_z(E_xM_x + E_yM_y)[1 + cL^2 + d(L_x^2 + L_y^2)] \\
&- \lambda_4 M_z(L_xE_x + L_yE_y)[1 + gL^2 + h(L_x^2 + L_y^2)] \\
&- \lambda_5 L_z M_z E_z[1 + aL^2 + b(L_x^2 + L_y^2)] \\
&- \lambda_6(E_xM_y - E_yM_x)(L_x^3 - 3L_xL_y^2) \\
&- \lambda_7 L_z E_z[M_y(L_x^2 - L_y^2) + M_x \times 2L_xL_y] \\
&- \lambda_8 L_z M_z[E_y(L_x^2 - L_y^2) + E_x \times 2L_xL_y] \\
&- \lambda_9 L_z[(E_xM_x - E_yM_y)(L_x^2 - L_y^2) \\
&+ (E_xM_y + E_yM_x) \times 2L_xL_y] - \lambda_{10}E_zM_z(3L_x^2 L_y - L_y^3)
\end{aligned} \tag{6}
$$

$$-\lambda_{11}(E_xM_x + E_yM_y)(3L_x^2L_y - L_y^3).$$

The exchange invariants of both the first and the third power over **L** with the corresponding constants are written out in the first line of this relation.

Dividing the tensor α into two parts $\alpha = \alpha^{(1)} + \alpha^{(3)}$, in addition to the results obtained previously [12] (the

constant $\Lambda^{(1)}$ is introduced in accordance with [13]), we now find from relations (1) and (2)

$$\alpha_{ij}^{(1)} = \begin{pmatrix} \lambda_1 L_y + \lambda_3 L_z & \lambda_1 L_x & (\Lambda^{(1)} + \lambda_2)L_x \\ \lambda_1 L_x & -\lambda_1 L_y + \lambda_3 L_z & (\Lambda^{(1)} + \lambda_2)L_y \\ \lambda_4 L_x & \lambda_4 L_y & (\Lambda^{(1)} + \lambda_5)L_z \end{pmatrix}.$$

From here, it immediately follows that

$$\alpha_{ij}^{(3)} \approx \begin{pmatrix} \lambda_1 kL^2L_y + \lambda_3 cL^2L_z & \lambda_1 kL^2L_x & (\Lambda^{(3)} + e\lambda_2)L^2L_x \\ \lambda_1 kL^2L_x & -\lambda_1 kL^2L_y + \lambda_3 cL^2L_z & (\Lambda^{(3)} + e\lambda_2)L^2L_y \\ \lambda_4 gL^2L_x & \lambda_4 gL^2L_y & (\Lambda^{(3)} + a\lambda_5)L^2L_z \end{pmatrix},$$

$$\alpha_{33} \approx [(\Lambda^{(1)} + \lambda_5) + (\Lambda^{(3)} + a\lambda_5)L^2]L_z,$$

and, if the constant denoted by us as a is negative and sufficiently large, so that $\Lambda^{(3)} + a\lambda_5 < 0$, then, while the temperature tends to zero, α_{33} also becomes negative.

A similar temperature behavior of the corresponding tensor components α_{ij} evidently manifests itself in the spin-flop phase. This behavior is completely consistent with the results of the experiment performed in [11]. However, we should note once again that the presence of the mixed term $\frac{1}{4}KL_z(3L_x^2L_y - L_y^3)$ of the fourth power in expansion (3) for the Gibbs potential results in the fact that the z-component of the antiferromagnetism vector L_z does not vanish in the spin-flop phase. The term of similar nature in expression (6) for $G_{ME} - (\lambda_{10}E_zM_z(3L_x^2L_y - L_y^3))$ contributes to α_{33}. This contribution is proportional to the third power of L. Due to this fact, the term α_{33} can differ from zero in the spin-flop phase [12].

REFERENCES

1. L. D. Landau and E. M. Lifshitz, *Course of Theoretical Physics*, Vol. 8: *Electrodynamics of Continuum* (Nauka, Moscow, 1992; Pergamon, New York, 1984).
2. I. E. Dzyaloshinskiĭ, Zh. Éksp. Teor. Fiz. **37**, 881 (1959) [Sov. Phys. JETP **10**, 628 (1960)].
3. D. N. Astrov, Zh. Éksp. Teor. Fiz. **38**, 984 (1960) [Sov. Phys. JETP **11**, 708 (1960)].
4. V. J. Folen, G. T. Rado, and E. W. Stalder, Phys. Rev. Lett. **6**, 607 (1961).
5. G. T. Rado, Phys. Rev. Lett. **6**, 609 (1961).
6. M. Date, J. Kanamori, and M. Tachiki, J. Phys. Soc. Jpn. **16**, 2589 (1961).
7. E. B. Royce and N. Bloembergen, Phys. Rev. **131**, 1912 (1963).
8. R. Hornreich and S. Shtrikman, Phys. Rev. **161**, 506 (1967); **159**, 408 (1967); Erratum: **166**, 598 (1968).
9. M. Mercier, E. F. Bertaut, G. Quezel, and P. Bauer, Solid State Commun. **7**, 149 (1969).
10. H. Yatom and R. Engelman, Phys. Rev. **188**, 793 (1969).
11. Yu. F. Popov, A. M. Kadomtseva, A. K. Zvezdin, *et al.*, Pis'ma Zh. Éksp. Teor. Fiz. **69**, 302 (1999) [JETP Lett. **69**, 330 (1999)].
12. D. V. Belov, G. P. Vorob'ev, A. K. Zvezdin, *et al.*, Pis'ma Zh. Éksp. Teor. Fiz. **58**, 603 (1993) [JETP Lett. **58**, 579 (1993)].
13. S. S. Krotov and A. V. Lisnyak, Vestn. Mosk. Univ., Ser. 3: Fiz., Astron., No. 3, 57 (2001).
14. G. T. Rado, Phys. Rev. **128**, 2546 (1962).
15. R. Engelman and H. Yatom, Phys. Rev. **188**, 803 (1969).

Translated by T. Galkina

═══════════════ **PHYSICS** ═══════════════

A Crystallographic Model for Describing of Exact Location of Atoms in Quasicrystals

V. C. Goulliaev

Presented by Academician K.S. Aleksandrov June 27, 2001

Received July 9, 2001

Since the discovery of quasicrystals [1], a large number of theoretical papers have been published devoted to their investigation (see, e.g., [2–6]). The main challenge to the theory of quasicrystalline structures is related to determination of the actual arrangement of atoms in a quasicrystal [7]. D. Gratias, one of discoverers of quasicrystals [1, 7], noted that for significant progress in studying physical properties of quasicrystals it is necessary to know the actual arrangement of atoms in these structures. Thus, in order to calculate

such properties of quasicrystals as strength, plasticity, electrical conduction, etc., we need a theory capable of thoroughly describing quasicrystal structures, i.e., much as traditional crystallography describes periodic crystals.

In this study, we analytically solve the problem of quasicrystal structures, namely, the determination of coordinates of atoms in a quasicrystal. For this, we apply a method involving traditional crystallography that describes periodic and incommensurate crystal
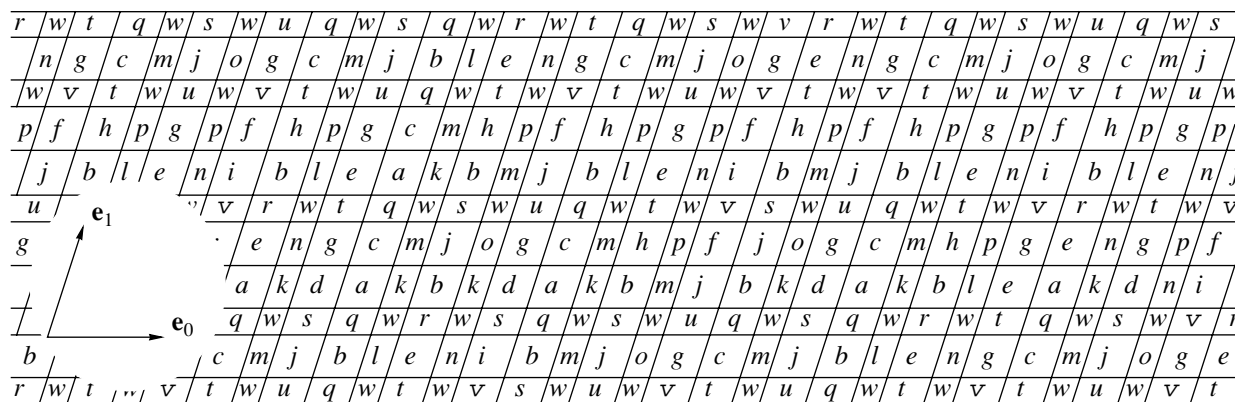

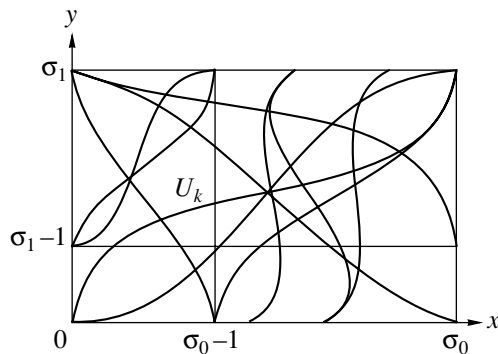**Fig. 1.** Scheme of a two-dimensional quasicrystal with the *a–w* structure cells.

Fig. 2. Validity of the condition $p_k(n + \beta) = 1$ in the region U_k corresponding to a *k*th structure cell.

Kirenskiĭ Institute of Physics, Siberian Division, Russian Academy of Sciences, Akademgorodok, Krasnoyarsk, 660036 Russia
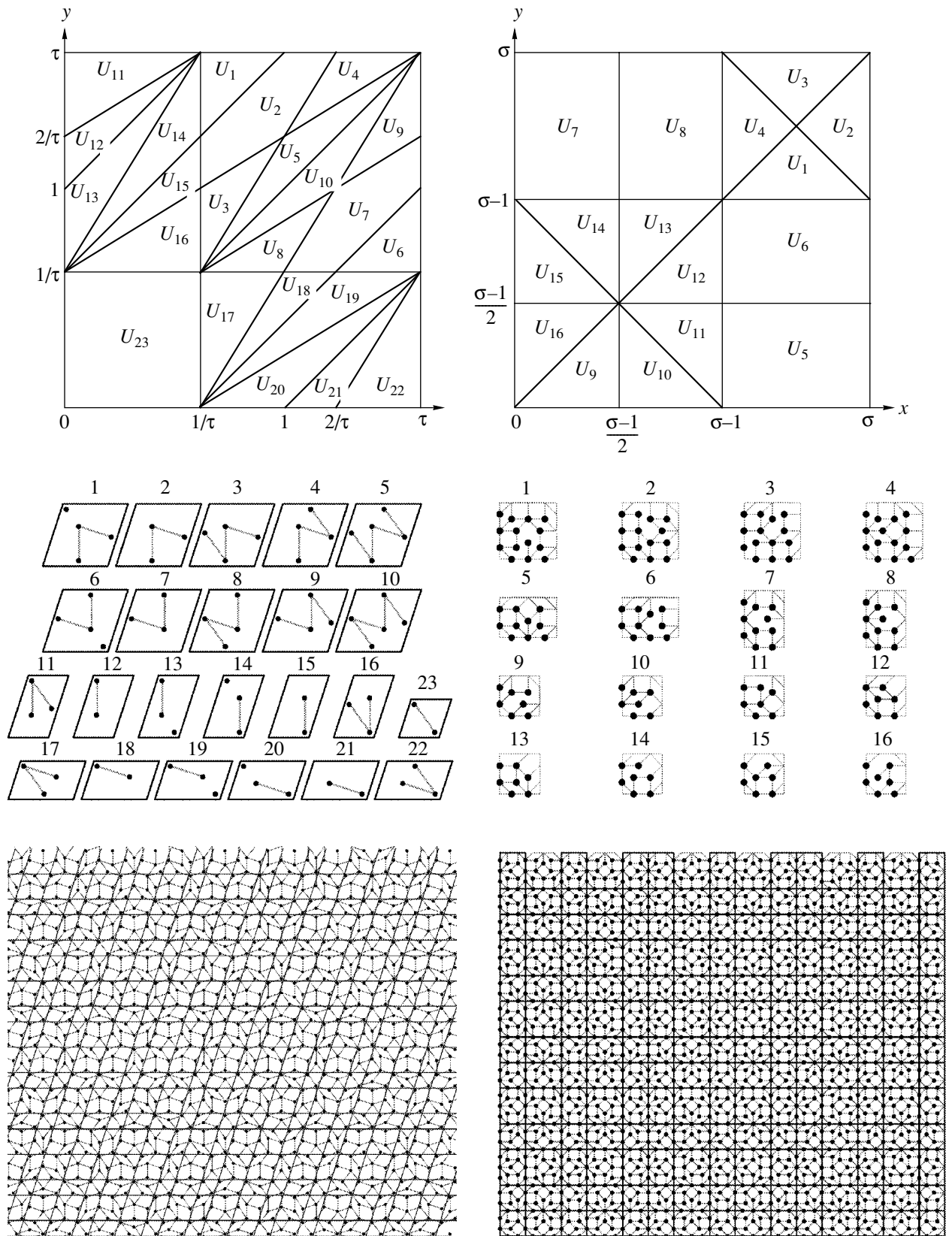
Fig. 3. The map of U_k regions and corresponding 23 structure cells for a Penrose quasicrystal (top left). The same scheme with 16 structure cells for the Ammann–Beencker quasicrystal (top right). Quasicrystals in the bottom part of the figure are generated by a computer program on the basis of formulas (1) and (2).
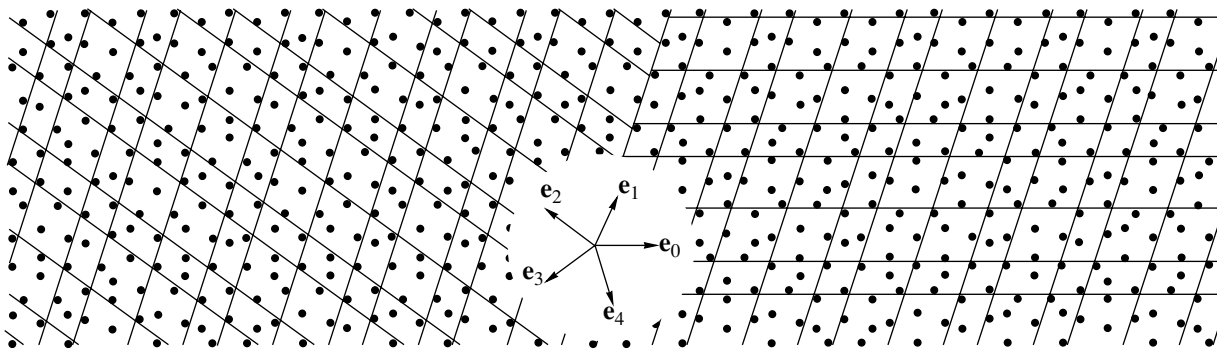
Fig. 4. Illustration of the symmetry for a Penrose quasicrystal, as an example. In the coordinated bases ($\mathbf{e}_0$, $\mathbf{e}_1$) and ($\mathbf{e}_1$, $\mathbf{e}_2$), a quasicrystal is described by formulas (1) and (2) but with different parameters $\boldsymbol{\alpha}$ and $\boldsymbol{\beta}$.

structures. This method generalizes the definition of a crystal. In the framework of the model proposed, a periodic crystal can be represented as a particular case of a quasicrystal. We obtained simple and clear formulas describing the position of any atom in the quasicrystal. The exact solutions for Penrose and Ammann–Beencker quasicrystals are presented. The method is universal and can be used in the analysis of biological microstructures and fractal images. The symmetries of quasicrystal structures are considered on the basis of superspace groups [8, 9], a classical method in the present-day description of incommensurate structures.

Crystal structures (in particular, quasicrystals) exhibiting point diffraction, which, however, are aperiodic, can be described by a finite number of structure cells. Figure 1 shows the scheme of a two-dimensional quasicrystal with a–w structure cells.

In such a quasicrystal whose crystallographic axes are parallel to base vectors $\mathbf{e}_0$ and $\mathbf{e}_1$, the structure cells are assumed to be situated in quasiperiodic lattice sites with coordinates

$$\mathbf{r}_n(\alpha, \beta) = \mathbf{e}_0 x_0(a_0, \beta_0) + \mathbf{e}_1 x_1(a_1, \beta_1),$$

where

$$x_{n_l} = a_l\left(n_l + a_l + \frac{1}{\chi_l}\left[\frac{n_l + \beta_l}{\sigma_l}\right]\right),$$

$[x]$ is the integer part of x, $\sigma_l > 1$ and χ_l are irrational numbers, a_l and β_l are arbitrary numbers, a_l are the lattice parameters, and $l = 0, 1$. In what follows, we assumed that $\dfrac{\beta_l}{\sigma_l} < 1$ since, in the opposite case, a_l changes; i.e., $a_l' = a_l + \dfrac{1}{\chi_l}\left[\dfrac{\beta_l}{\sigma_l}\right]$. Let the vector $\mathbf{Y}_n(\beta')$ be given in a Cartesian coordinate system by the following expression:

$$\mathbf{Y}_n(\beta) = \left(\left\{\frac{n_0 + \beta_0}{\sigma_0}\right\}, \left\{\frac{n_1 + \beta_1}{\sigma_1}\right\}\right),$$

where $\{x\}$ is the fractional part of x. Then, the distribu-

tion function for the density of atoms in a quasicrystal with K structure cells can be written out in the form

$$\rho(n, \alpha, \beta)$$
$$= \sum_{n_0, n_1 = -\infty}^{\infty} \sum_{k=1}^{K} p_k(n + \beta) \sum_{j_k}^{J_k} \delta(\mathbf{r} - \mathbf{r}_n(\alpha, \beta) - \mathbf{r}_{j_k}), \quad (1)$$

$$p_k(n + \beta) = \begin{vmatrix} 0, & \mathbf{Y}_n(\beta) \in U_k \\ 1, & \mathbf{Y}_n(\beta) \notin U_k, \end{vmatrix} \quad (2)$$

where $\mathbf{r}_{j_k}$ is the vector characterizing the positions of atomic centers in a kth structure cell with respect to the lattice point with which the cell is connected; the domains U_k are located within the rectangle $\sigma_0 \times \sigma_1$. In general, the shapes of U_k regions can be arbitrary (Fig. 2).

Equations (1) and (2) determine the positions of atoms in a quasicrystal and can be easily introduced into a computer program [10] to generate a quasiperiodic structure of arbitrary size having arbitrary parameters α and β. As an example, Fig. 3 demonstrates a solution for Penrose quasicrystals $\left(\sigma_0 = \sigma_1 + \chi_0 = \chi_1 = \tau, \right.$

$\tau = \dfrac{1 + \sqrt{5}}{2}, \ a_0 = a_1 = 1 \Big)$ and Ammann–Beencker

$(\sigma_0 = \sigma_1 = \chi_0 = \chi_1 = a_0 = a_1 = \sigma, \ \sigma = 1 + \sqrt{2})$ quasicrystals.

For simplicity, we considered the construction of a two-dimensional quasicrystal. In the three-dimensional case, the structure cells represent parallelepipeds with their edges parallel to the crystallographic axes, and the U_k regions are considered as volume elements in a rectangular parallelepiped. This approach was first proposed by the author in [11].

For an arbitrary shape of U_k domains, the analytical calculation [12] of the radiation diffraction on a quasicrystal, according to formulas (1) and (2), shows that

the diffraction pattern is independent of parameters α and β. Since physical properties of a quasicrystal, namely, the scattering of radiation, do not depend on α and β, the following invariance condition can be formulated for a quasicrystal [8, 9]: if only the parameters α and β, rather than the function ρ in itself, change under the action of a transformation operator on the atomic-density distribution, then such a quasicrystal is invariant with respect to this transformation. Thus, if the condition

$$R\left(\frac{2\pi}{q}, \mathbf{r}_0\right)\rho(\mathbf{r}, \alpha, \beta) = \rho(\mathbf{r}, \alpha', \beta'),$$

is fulfilled [where $R(\varphi, \mathbf{r}_0)$ is the rotation operator, φ is the rotation angle, and $\mathbf{r}_0$ is the coordinate of a point about which the rotation occurs], then such a quasicrystal has a symmetry axis on the order of q (Fig. 4).

ACKNOWLEDGMENTS

REFERENCES

1. D. Shechtman, I. Blech, D. Gratias, and J. W. Cahn, Phys. Rev. Lett. **53**, 1951 (1984).
2. P. Kramer and R. Neri, Acta Crystallogr. A **40**, 580 (1984).
3. P. A. Kalugin, A. Yu. Kitaev, and L. S. Levitov, Pis'ma Zh. Éksp. Teor. Fiz. **41**, 119 (1985) [JETP Lett. **41**, 145 (1985)].
4. D. Levine and P. J. Steinhardt, Phys. Rev. B **34**, 596 (1986).
5. M. Baake, P. Kramer, M. Schlotmann, and D. Zeidler, Int. J. Mod. Phys. **4**, 2217 (1990).
6. B. Grushko, R. Wittmann, and R. Urban, J. Mater. Res. **9**, 2899 (1994).
7. D. Gratias, Recherche **178**, 788 (1986).
8. A. Janner and T. Jansen, Phys. Rev. B **15**, 643 (1977).
9. A. Janner and T. Jansen, Acta Crystallogr. A **36**, 399 (1980).
10. http://www.kirensky.ru/download/tilings.zip.
11. V. C. Gouliaev, Quasicrystals, Preprint of Krasnoyarsk State Pedagogical Univ., No. 1F, Krasnoyarsk, 1994.
12. V. Gouliaev, e-print cond-mat/9903263; http//xxx.lanl.gov.

Translated by Yu. Vishnyakov

=========== **PHYSICS** ===========

Thermodynamic Investigation of Intermediate Phases
for the Ni–Zr System

## A. I. Zaitsev, N. E. Zaitseva, and E. Kh. Shakhpazov

Presented by Academician O.A. Bannykh July 5, 2001

Received July 9, 2001

Nickel–zirconium alloys have a high glass-forming ability in a wide range of their concentrations and thus are a base for a number of bulky amorphous metallic materials [1]. However, no Gibbs energies for the formation of nickel–zirconium crystalline phases have been determined until now due to experimental difficulties associated with the high reactivity of zirconium and low values of partial saturated-vapor pressures of the components. The lack of experimental data prevents the analysis of thermodynamic and kinetic parameters of the Ni–Zr-liquid transition into the amorphous state, hampers understanding the reasons for the easiness of this phenomenon proceeding in a number of systems of transition metals, and impedes revealing the degree of stability and possible directions of further transformations into vitreous compositions.

In the study proposed, Knudsen mass spectrometry was used for investigating a vapor composition and thermodynamic properties of nickel–zirconium alloys within the temperature range 971 to 1518 K and the composition range 18.0 to 64.9 at. % of Zr. The saturated-vapor pressure was measured with the help of doubled Knudsen cells. As a reference medium, we used copper (99.999%) or ultrapure iron with an impurity content of 10^{-6}%. For synthesis of alloys, we used zirconium iodide (of 99.99% purity) and electrolytic nickel (of 99.98% purity). The procedures for preparing samples and performing the experiments were similar to those described previously [2].

Crystalline Ni–Zr alloys are characterized by extremely low partial pressures of the vapor of components. At temperatures of their stability, the Knudsen-measurement technique is capable of measuring only a nickel-vapor pressure over samples whose compositions belong to the regions of heterogeneous equilibrium
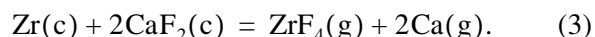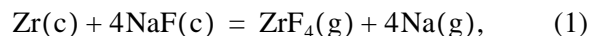
$$Ni + Ni_5Zr, \ Ni_5Zr + Ni_7Zr_2, \ Ni_7Zr_2 + Ni_{21}Zr_8.$$
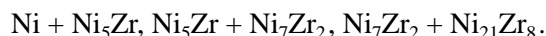
Kurdyumov Institute for Metal Physics
and Functional Materials,
Bardin Central Research Institute
for the Iron and Steel Industry,
Vtoraya Baumanskaya ul. 9/23, Moscow, 107005 Russia

These data are evidently insufficient for determining the thermodynamic functions of intermediate phases. With the purpose of establishing them, we developed a procedure based on initiating and investigating equilibrium with the participation of volatile products. We added into effusion cells with alloys under investigation certain quantities of fluorides of magnesium, calcium, or sodium. As a result of their interaction, volatile zirconium fluorides appear. In the mass spectra of saturated vapor, ZrF_3^+, ZrF_2^+, ZrF^+, Zr^+, and Na^+, Mg^+, or Ca^+ ions were detected, respectively. The lines of ZrF_3^+ and Na^+, Mg^+, or Ca^+ were the most intense. The experiments carried out with Ni–Zr alloys of various compositions and metallic zirconium, as well as calculations performed, showed that their interaction with admixtures of fluorides of Mg, Ca, and Na proceeds, basically, in the reactions

$$Zr(c) + 4NaF(c) = ZrF_4(g) + 4Na(g), \quad (1)$$

$$Zr(c) + 2MgF_2(c) = ZrF_4(g) + 2Mg(g), \quad (2)$$

$$Zr(c) + 2CaF_2(c) = ZrF_4(g) + 2Ca(g). \quad (3)$$

The ZrF_3^+, ZrF_2^+ ZrF^+, and Zr^+ ions have a fragmentation origin and are formed by the dissociative ionization of zirconium–tetrafluoride (ZrF_4) molecules. Na^+, Mg^+, or Ca^+ ions originate from Na, Mg, or Ca atoms, respectively. The ratios 100 : 7.5 : 5.9 : 4.0, which had been observed between ion-current intensities for ZrF_3^+, ZrF_2^+, ZrF^+, Zr^+, virtually coincided with those previously established in [3] while investigating evaporation of ZrF_4. For reactions (2) and (3), two measurement runs were carried out under different experimental conditions (effusion-orifice diameter, effusion-chamber material). The virtually complete coincidence of the experimental results (Fig. 1) demonstrates that a state close to equilibrium is attained in the effusion cell and
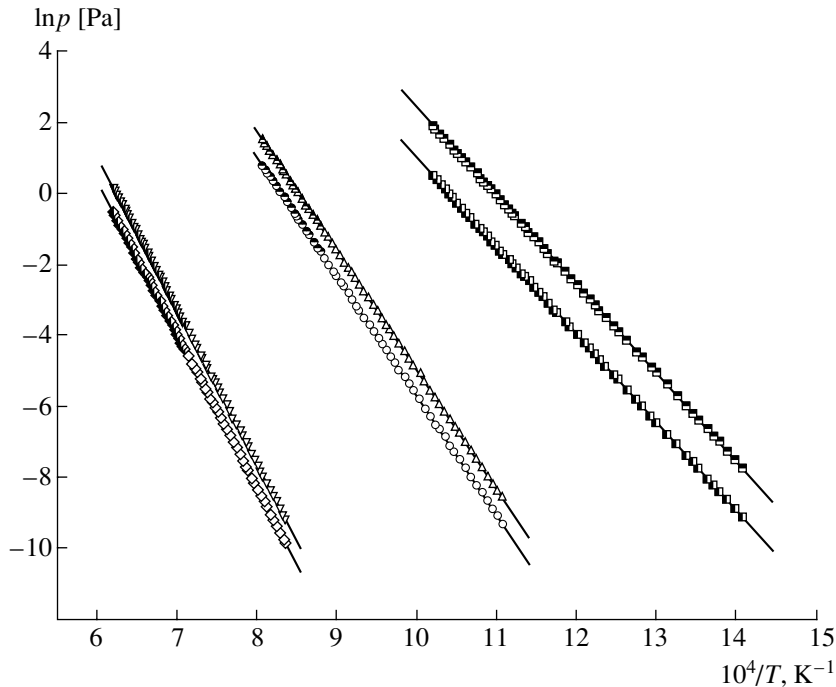
Fig. 1. Values of partial pressures for vapors of ZrF_4 and Na, Mg, or Ca over the mixtures of fluorides of sodium, magnesium or calcium with zirconium under various experimental conditions (added fluoride, effusion-cell material, material of the inner-surface coating, effusion-orifice diameter [d_{eff}, mm]): (■) Na and (▫) ZrF_4 (NaF, Mo, ZrB_2, 0.114); (△) Mg and (○) ZrF_4 (MgF_2, Mo, BN, 0.143); (▲) Mg and (◓) ZrF_4 (MgF_2, Nb, ZrB_2, 0.208); (▽) Ca and (◇) ZrF_4 (CaF_2, Ta, BN, 0.236); (▼) Ca and (◆) ZrF_4 (CaF_2, Nb, ZrB_2, 0.129).

that the data obtained are reliable. Data analysis made it possible to determine the variations in the Gibbs energy of reactions (1)–(3) (expressed in J/mol):

$$\Delta_r G\,(1) = 1033400 \pm 1200 - (641.5 \pm 1.5)T, \tag{4}$$
$$711 \leq T \leq 982 \text{ K,}$$

$$\Delta_r G\,(2) = 835700 \pm 800 - (417.1 \pm 0.7)T, \tag{5}$$
$$904 \leq T \leq 1241 \text{ K,}$$

$$\Delta_r G\,(3) = 1074800 \pm 1000 - (375.9 \pm 0.7)T, \tag{6}$$
$$1197 \leq T \leq 1618 \text{ K.}$$

These results virtually coincided with the JANAF reference data [4]. For example, the Gibbs-energy calculation for reaction (1) according to the data of [4] in the temperature range 700–1000 K led to the equation

$$\Delta_f G\,(1) = 1028100 - 636.5 \pm 1.5T, \tag{7}$$
$$700 \leq T \leq 1000 \text{ K.}$$

As can be seen from Fig. 1, introducing one or another additive leads to the initiation of reactions with volatile products within a wide temperature range from

700 to 1600 K, which makes it possible to cover the entire temperature range for investigation of crystalline Ni–Zr alloys.

From the measured values of partial vapor pressures (ion currents) of ZrF_4 and Mg, Ca, or Na over the mixtures of fluorides with nickel–zirconium alloys and a pure metal, we calculated partial thermodynamic functions for Zr (see table). This was done according to the expressions for constants of equilibrium in reactions (1)–(3). In such calculations, no ionization cross sections of gas molecules were used, which significantly elevated the accuracy of the desired values. For each of the two-phase regions in the diagram of state for the Ni–Zr system, we investigated several alloys of various compositions in different experimental conditions (effusion-chamber material, effusion-orifice area). Depending on the temperature measurement range, we used admixtures of different fluorides of Na, Mg, or Ca. In all cases, the coincidence was observed within the experimental error for the thermodynamic characteristics found under various conditions. This fact is illustrated in Fig. 2 by the example of two-phase fields,

$$Ni_{10}Zr_7 + Ni_{11}Zr_9, \ Ni_{10}Zr_7 + NiZr, \ Ni_{11}Zr_9 + NiZr,$$
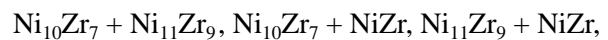
and proves that a state close to equilibrium is attained in the effusion cell when performing experiments with Ni–Zr alloys.
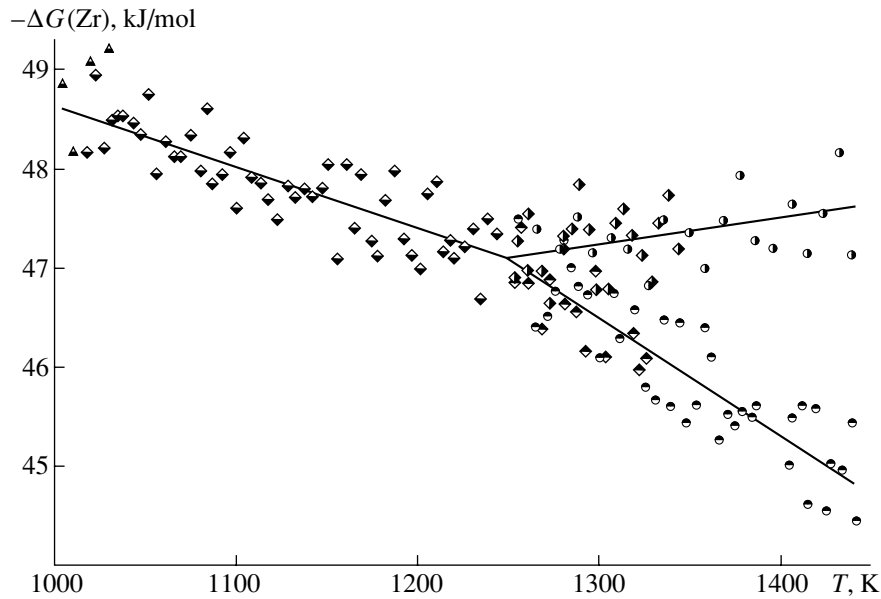
Fig. 2. Partial Gibbs energy for zirconium, which was established in investigations of alloys belonging to the regions of heterogeneous equilibrium of $Ni_{10}Zr_7 + Ni_{11}Zr_9$, $Ni_{11}Zr_9 + NiZr$, and $Ni_{10}Zr_7 + NiZr$ under various experimental conditions [x(Zr)], added fluoride, effusion-cell material, material of the inner-surface coating, and effusion-orifice diameter (d_{eff}, mm)}: (◇), (◆) 0.430, MgF_2, Nb, ZrB_2, 0.182; (◑) 0.442, CaF_2, Ta, BN, 0.224; (◆) 0.476, MgF_2, Mo, BN, 0.157; (▲) 0.476, NaF, Mo, BN, 0.157; (◓) 0.491, CaF_2, Nb, ZrB_2, 0.215.

The determination of partial thermodynamic properties of both components in the heterogeneous regions of $Ni_5Zr + Ni_7Zr_2$ and $Ni_7Zr_2 + Ni_{21}Zr_8$ made it possible to calculate the thermodynamic functions for the formation of corresponding phases. The thermodynamic characteristics of other compounds were found with the help of the Gibbs–Duhem equation. As a result, the following expressions were obtained for the temperature dependences of the Gibbs energy in the formation of intermetallic nickel–zirconium compounds from fcc Ni and bcc Zr:

$$\Delta_f G\left(\frac{1}{6}Ni_5Zr\right) = -(32025 \pm 790) + (2.74 \pm 0.57)T,$$

$$1108 \leq T \leq 1518 \text{ K},$$

$$\Delta_f G\left(\frac{1}{9}Ni_7Zr_2\right) = -(42930 \pm 754) + (4.84 \pm 0.55)T,$$

$$1108 \leq T \leq 1518 \text{ K},$$

$$\Delta_f G\left(\frac{1}{29}Ni_{21}Zr_8\right) = -(47028 \pm 716) + (5.99 \pm 0.53)T,$$

$$1201 \leq T \leq 1438 \text{ K},$$

$$\Delta_f G\left(\frac{1}{17}Ni_{10}Zr_7\right) = -(50075 \pm 611) + (5.16 \pm 0.46)T,$$

$$1058 \leq T \leq 1339 \text{ K},$$

(8)

$$\Delta_f G\left(\frac{1}{20}Ni_{11}Zr_9\right) = -(49675 \pm 586) + (4.66 \pm 0.45)T,$$

$$1253 \leq T \leq 1440 \text{ K},$$

$$\Delta_f G\left(\frac{1}{2}NiZr\right) = -(50793 \pm 553) + (5.23 \pm 0.43)T,$$

$$1004 \leq T \leq 1441 \text{ K},$$

$$\Delta_f G\left(\frac{1}{3}NiZr_2\right) = -(36460 \pm 450) + (2.12 \pm 0.37)T,$$

$$971 \leq T \leq 1345 \text{ K}.$$

Until now, only the formation enthalpy was experimentally investigated for Ni–Zr intermediate phases by means of dissolving calorimetry [5, 6] and direct reaction calorimetry [7]. The values $\Delta_f H$ [5–7] are compared in Fig. 3 with the data presented in this paper. As is seen, the results of all these studies agree well with each other.

The authors of [8] estimated the Gibbs energy for the formation of Ni–Zr intermediate phases at 1273 K on the basis of results of measuring the heat capacity for six Ni–Zr alloys with zirconium molar fractions of 0.30, 0.39, 0.47, 0.48, 0.54, and 0.61. In these experiments, differential scanning calorimetry within the temperature range of 120 to 800 K and data of [6, 7] for $\Delta_f H$ was used. As can be seen from Fig. 3, values of $\Delta_f G$

found in [8] are somewhat lower than our data. This discrepancy is likely associated with errors inherent in [8] when performing measurements and calculations. Namely, for determining the absolute entropy of compounds, the authors of [8] investigated heterogeneous alloys instead of homogeneous samples. For calculating the absolute entropy and the formation entropy at 1273 K, the measured heat capacities were extrapolated to the large temperature range of 120 and 473 K, respectively. At last, the formation entropy for the Ni_7Zr_2 phase was estimated by a simple interpolation of the values of $\Delta_f S(Ni_{21}Zr_8)$ to zero in the case of metallic nickel.

The authors of [9] performed an analysis of available experimental data on thermodynamic properties and phase equilibrium in the Ni–Zr system. As the initial thermodynamic data, they used the values of the formation enthalpy for the compounds, which had been established in [5–7]. The optimal values of $\Delta_f H$ obtained in [9] turned out to be close to both the results of [5–7] and those of the present study, whereas a distinction was observed in the values of $\Delta_f G$ (Fig. 3). This is caused by the fact that the initial information in [9] was insufficient for correctly determining the Gibbs energy of the formation of intermediate phases.

In our study, the thermodynamic functions for intermediate phases of the Ni–Zr system have been established while investigating alloys of various compositions and under different experimental conditions (effusion-chamber material, effusion-orifice diameter, and type of reactive admixture). These functions agree well both among themselves and with the independent experimental data of [10] on the phase equilibrium. For example, the thermodynamic functions of an equiatomic nickel–zirconium compound calculated on the basis of data obtained for the two-phase field of $Ni_{10}Zr_7 + NiZr$ and for the heterogeneous-equilibrium regions of $Ni_{10}Zr_7 + Ni_{11}Zr_9$ and $Ni_{11}Zr_9 + NiZr$ coincide. The peritectic–decomposition temperature for
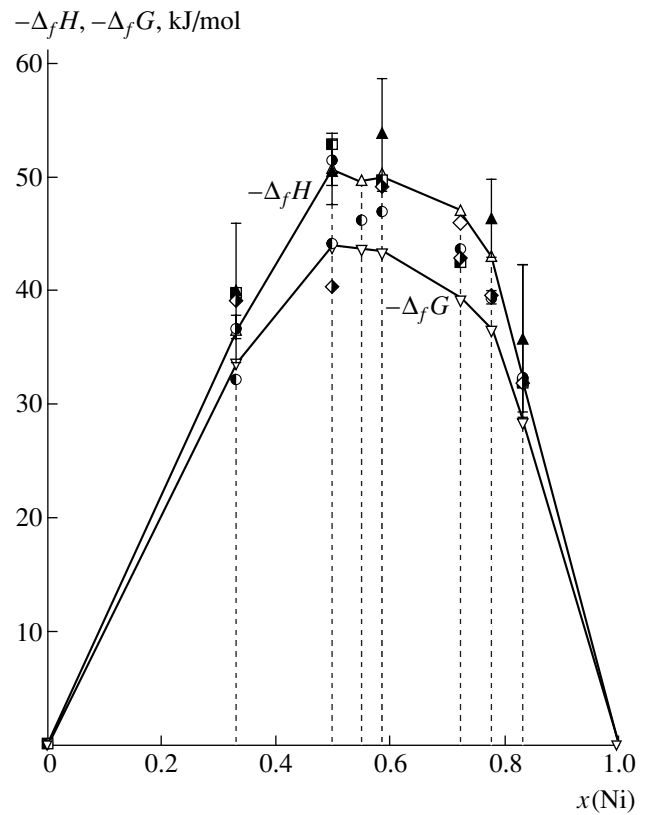

Fig. 3. Thermodynamic functions for the intermediate-phase formation in the Ni–Zr system from fcc Ni and bcc Zr according to the results of this study: ($\triangle$) $\Delta_f H$, ($\triangledown$) $\Delta_f G$, and data for $\Delta_f H$ of other authors: ($\diamond$) [5], ($\blacktriangle$) [6], ($\obullet$) [7], ($\blacksquare$) [9], ($\odot$) [8], and ($\blacklozenge$) [9].

$Ni_{11}Zr_9$ calculated from the data displayed in Fig. 2 attains 1248 K, whereas the value found by methods of physicochemical analysis is equal to 1251 K [10]. All these facts testify to the reliability of the procedure used for studying crystalline Ni–Zr alloys and to the precision of the thermodynamic values obtained.

Partial thermodynamic functions of components in Ni–Zr heterogeneous alloys with respect to fcc Ni and bcc **Zr**

Phase field	T, K	n	Component	$-\Delta H$, J/mol	$-\Delta S$, J/(mol K)
$Ni_5Zr + Ni_7Zr_2$	1108–1518	91	Zr	$197\,186 \pm 1000$	-34.55 ± 0.76
	1274–1518	55	Ni	-1086 ± 926	-3.64 ± 0.66
$Ni_7Zr_2 + Ni_{21}Zr_8$	1201–1438	62	Zr	$101\,972 \pm 2010$	-21.41 ± 1.52
	1336–1438	25	Ni	$26\,097 \pm 3072$	0.12 ± 2.22
$Ni_{21}Zr_8 + Ni_{10}Zr_7$	1058–1339	79	Zr	$63\,249 \pm 997$	1.57 ± 0.82
$Ni_{10}Zr_7 + Ni_{11}Zr_9$	1253–1440	57	Zr	$43\,886 \pm 2007$	-2.58 ± 1.5
$Ni_{10}Zr_7 + NiZr$	1004–1244	60	Zr	$54\,873 \pm 1258$	6.23 ± 1.13
$Ni_{11}Zr_9 + NiZr$	1253–1441	52	Zr	$61\,973 \pm 2304$	11.92 ± 1.73
$NiZr + NiZr_2$	971–1345	89	Zr	7880 ± 770	-4.26 ± 0.67

REFERENCES

1. P. J. Desre, Mater. Res. Soc. Symp. Proc. **554**, 51 (1999).
2. A. I. Zaitsev, N. V. Korolyov, and B. M. Mogutnov, High Temp. Sci. **28**, 341 (1990).
3. P. A. Akishin, V. I. Belousov, and L. N. Sidorov, Zh. Neorg. Khim. **8**, 1520 (1963).
4. JANAF Thermochemical Tables, J. Phys. Chem. Ref. Data **14**, 1 (1985).
5. F. H. M. Spit, J. W. Drijver, and S. Radelaar, Scr. Metall. **14**, 1071 (1980).
6. M. P. Henaff, C. Colinet, and A. Pasturel, J. Appl. Phys. **56**, 307 (1984).
7. J. C. Gachon and J. Hertz, CALPHAD: Comput. Coupling Phase Diagrams Thermochem. **7** (1), 1 (1983).
8. J. F. Smith, Q. Jiang, R. Luck, and B. Predel, J. Phase Equilib. **12**, 538 (1991).
9. N. Saunders, CALPHAD: Comput. Coupling Phase Diagrams Thermochem. **9** (4), 297 (1985).
10. P. Nash and C. S. Jayanth, Bull. Alloy Phase Diagrams **5**, 144 (1984).

Translated by V. Bukhanov

Formation of Diamond-Like Boron Nitride by Pulsed Heating

Academician V. E. Fortov*, S. S. Batsanov**, S. M. Gavrilkin**, L. I. Kopaneva**, V. N. Korobenko*, and A. I. Savvatimskiĭ*

Boron nitride (BN) is an artificially produced compound. This material is interesting due to its great hardness. Instruments using BN compete with those using diamond. The interest in application of diamondlike BN is caused by its two advantages. Boron nitride is annealed at 1800°C; i.e., it is efficient at higher (compared to diamond) temperatures. In addition, boron nitride does not react with metals. This makes it possible to employ this material for processing hardened steels.

It is well known that in the case of shock compression of hexagonal boron nitride (h-BN), the dense wurtzite phase (w-BN) is always formed in a thick-walled recovery ampoule. At the same time, the formation under these conditions of the cubic modification, the so-called sphalerite (c-BN), was apparently not observed. This situation is usually explained by the high-temperature nature of the cubic modification [1]. This fact leads to failures while loading specimens in the dynamic mode. For polymorphic transformation, a high initial temperature of a specimen being compressed is necessary. However, in combination with additional heating caused by the shock compression, this can lead to such high residual temperatures that, after the shock compression is over, annealing of the formed cubic modification c-BN occurs. At low (or room) initial temperatures, only the low-temperature wurtzite phase is formed.

However, there exists another possible (kinetic) reason for the absence of the cubic form in the case of a direct pulsed transformation of h-BN, e.g., due to the extremely high activation energy of this process. The h-BN ⟶ c-BN transition of a specimen compressed under conditions of millisecond-scale pulsed heating in a Belt-type high hydrostatic-pressure chamber was described by Bundy and Wentorf [2], indicating the possibility of millisecond-time phase transformation.

Later on, the results of Bless [3] were published. In this experiment, h-BN placed into a copper tube was compressed by the electromagnetic field up to pressures $P = 182$ kbar. According to the author's estimates, in the case of specimen porosity of about 5%, a temperature of 1000°C was attained due to the heating of rubbing particles. As a result, c-BN lines were observed in the X-ray diffraction pattern. However, the author of [3] made no mention of the quantitative yield of this phase. Therefore, it is possible that the temperature required for the phase transformation was attained only on the surface of rubbing particles and that the cubic modification was formed only in the thin surface layer.

Meanwhile, in the case of initial high temperatures, explosive loading can lead to the formation of the cubic c-BN phase only in the case of dynamic–static compression [4]. Indeed, in this method, the static pressure (20 kbar) is produced at the stage of shock unloading, which prevents annealing of the dense phase. However, due to the complexity of these experiments, it is difficult to choose their optimal temperature. Therefore, we undertook an investigation for the possibility of cubic-phase formation under conditions that can be considered tentative.

The experiments were carried out in the following manner. A tablet made of a h-BN and W (tungsten) powder mixture with a volumetric ratio of 1 : 1 was placed between Bridgman anvils in a miniature press. The area of the Bridgman anvils was subjected to the action of a force equivalent to a pressure of ~80 kbar, which was produced by means of an oil press. Then the tablet to which high pressure was applied was fed by a single electric-current pulse with an amplitude of 20 to 45 kA. An electric-pulse setup that had been used previously [5] in studies of properties of liquid carbon under pulsed heating was employed. At the moment of passing the short-time electric-current pulse (with a duration of about several tens of microseconds) through the tablet, the temperature reached the tungsten melting point, i.e., approximately 3700 K. (This estimate has been obtained in the course of experiment by the observation of melted traces of tungsten.) After termination of the pulsed discharge and decrease in pressure, the tablet of the substance under investigation was extracted from the experimental setup. Then it was subjected to study by X-ray and IR-spectroscopy methods

---

* *Institute of High-Energy Densities,*
Associated Institute of High Temperatures,
Russian Academy of Sciences,
Izhorskaya ul. 13/19, Moscow, 127412 Russia
** *Centre of High Dynamic Pressure,*
All-Russia Research Institute of Physicotechnical
and Radio-Engineering Measurements,
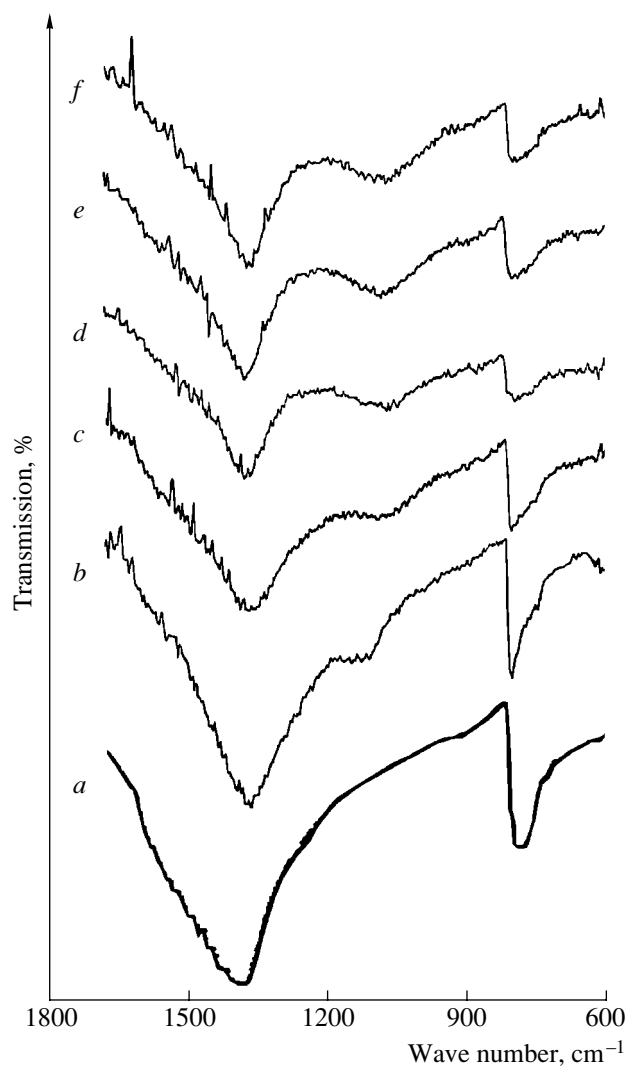*Mendeleevo, Moscow oblast, 141570 Russia*

Fig. 1. Evolution of the IR absorption spectra of BN while varying the charging voltage of the setup (elevation of the voltage corresponds to the rise of the heating electric current and, correspondingly, to the increase in temperature): (*a*) initial BN + W specimen; (*b*) BN + Cu, the voltage is 12 kV; (*c*) BN + W, the voltage is 10 kV; (*d*) BN + W, the voltage is 11.5 kV; (*e*) BN + W, the voltage is 12.5 kV; (*f*) BN + W, the voltage is 16 kV.

Fig. 2. Evolution of h-BN: (*a*) initial specimen; (*b*) the specimen after the pulsed action at a high pressure (the c-BN band is additionally shown with the tenfold increase in the sensitivity); (*c*) the specimen after the electric-pulse action at a high pressure + subsequent steady-state thermal treatment.

with the help of DRON-3 and Specord measuring devices, respectively. The X-ray diffractometry turned out to be low informative in this case. Actually, owing to the high concentration of tungsten, the BN lines do not manifest themselves. At the same time, the reflections of tungsten were slightly displaced (within the limits of several hundredths of an angstrom) towards the smaller parameters of the tungsten cell. This occurred apparently due to the formation, in a very insubstantial concentration, of the W–O or W–N incorporation solid solution.

On the basis of studying IR spectra, the appearance of a dense BN form was observed whose concentration increased with the rise of the electric-current pulse.
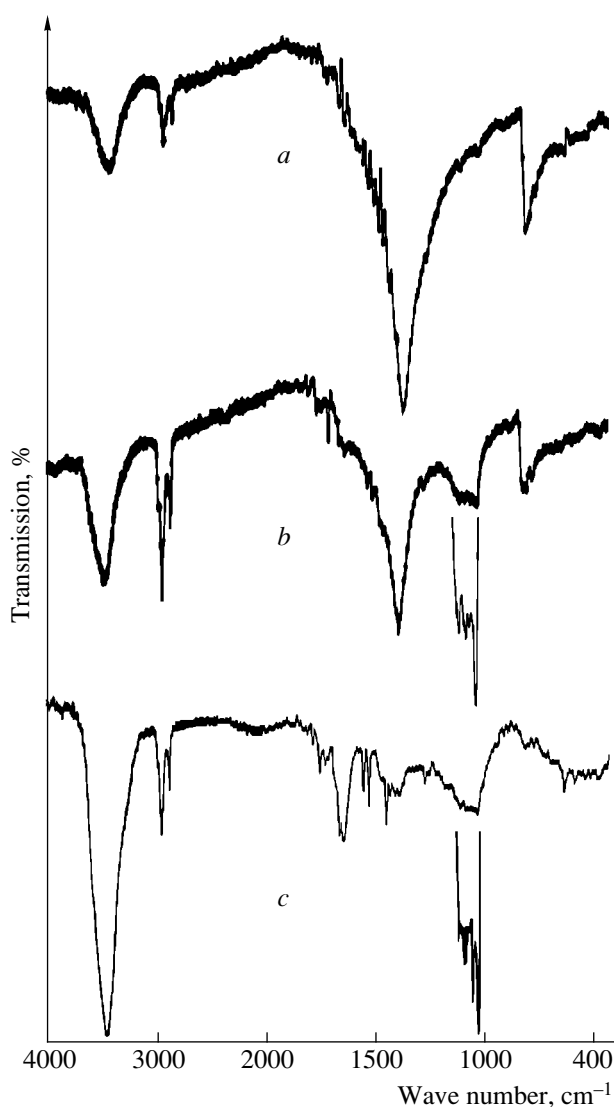
Figure 1 shows the evolution of the absorption spectra measured in this experimental run. In order to determine the structure of the BN dense form, a specimen obtained as a result of electric-pulse loading was subjected to thermal processing after the experiment. The specimen was heated in ambient argon for 5 h at a temperature of 1000°C. Then we compared the IR spectra of the original, transformed, and heated specimens (see Fig. 2). As the wurtzite modification is annealed even at 850°C, the spectrograms presented indicate the invariability of the absorption band for the dense phase (~1000 cm^{-1}) and provide an idea on its quantitative yield (~30% of the mass of the original hexagonal phase). Finally, in Fig. 3, the data corresponding to indicated conditions for thermal treatment of all BN
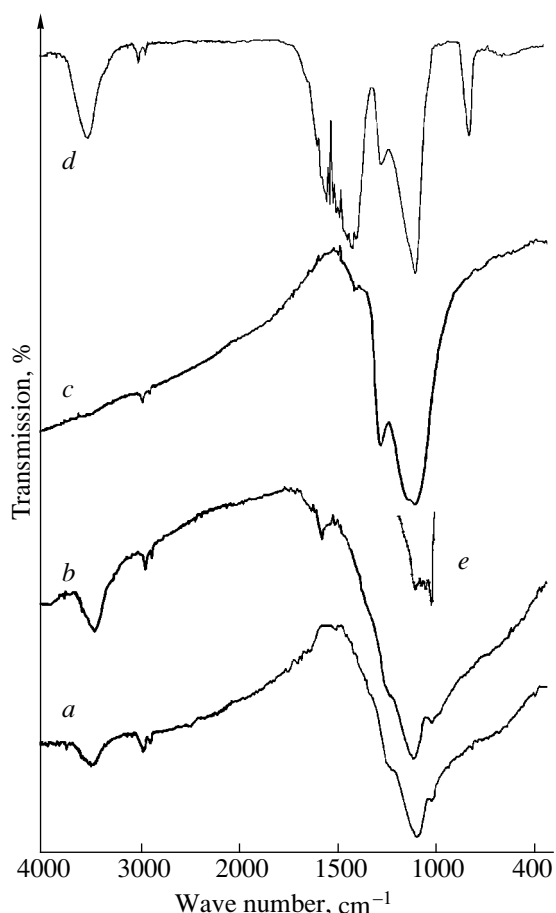
Fig. 3. Effect of annealing at 1000°C (5 h in ambient argon) on the IR spectra of polymorphic BN modification: (*a*) standard specimen of c-BN (1112 cm^{-1}); (*b*) c-BN after thermal treatment; (*c*) standard specimen of w-BN (1060 cm^{-1}); (*d*) hexagonal phase of h-BN (1380 cm^{-1}) formed from w-BN; (*e*) specimen obtained as a result of electric-pulse treatment.
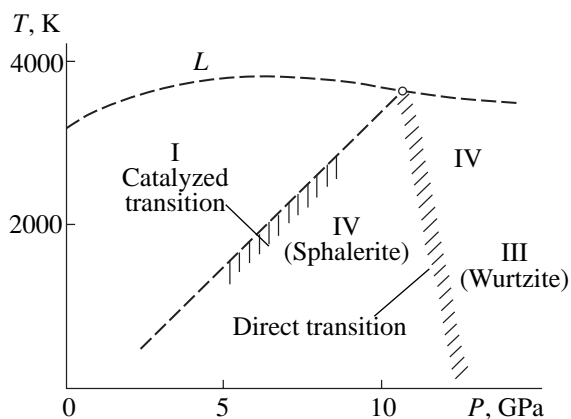

Fig. 4. Phase diagram borrowed from [2] for BN. (Notation corresponds to that of [2].): (*L*) liquid phase; (I) hexagonal (graphite-like) boron nitride h-BN; (III) (dense phase) w-BN; (IV) sphalerite (diamond-like modification) c-BN. Hatched curve is the line of equilibrium between the graphite-like and dense modifications (catalyzed transition of the hexagonal phase I into sphalerite IV); hatched straight line corresponds to the phase transition (without catalysts) of wurtzite (III) into sphalerite (IV).

modifications are displayed. These data unambiguously testify to the fact that we managed to synthesize the cubic form in the above-mentioned mode. At the same time, the intensity of the characteristic absorption band in the IR spectrum of the specimen obtained turned out to be enhanced by a factor of 10. From this result, it follows that the shape of the absorption band differs from the standard one, which implies possible structural peculiarities of specimens synthesized in the pulsed mode.

In Fig. 4, the phase diagram taken from [1, 2] for BN is presented. A similar phase diagram is also given in [6]. The high-pressure phases of BN III (wurtzite) and IV (sphalerite) can be obtained by either the catalytic method or directly, without the presence of catalysts (Fig. 4). It was assumed [1] that, at a temperature below 1600°C, the transition of h-BN into w-BN occurs, while at higher temperatures c-BN is formed. In Fig. 4, the transition of h-BN into the diamond-like modification c-BN is realized at a pressure of 110 kbar and temperature of ~2000 K. In [6], it was established that this transition can occur under steady-state conditions at a pressure of 80 kbar and temperature of about 2000 K. The results of the present experiments with pulsed loading, which were performed at an initial pressure of ~80 kbar and at a temperature of ~ 3700 K, give grounds for the conclusion that rapid heating is not an obstacle for such a phase transition. The distinction of the rapid method employed by the authors of this paper from the virtually steady-state method described in [6] consists in fast (tens of microseconds) pulsed heating that has no limitations related to the temperatures to be attained. This is rather favorable for research studies and further automation of the technological process. The fact that in the experiment under consideration a mass yield of the diamond-like phase attained approximately 30% (according to our estimates) indicates the high operation speed of the direct phase transition.

ACKNOWLEDGMENTS

REFERENCES

1. E. Yu. Tonkov, *High Pressure Phase Transformations* (Metallurgiya, Moscow, 1988; Gordon and Breach, Philadelphia, 1992), Vol. 1.
2. F. P. Bundy and R. H. Wentorf, J. Chem. Phys. **38**, 1155 (1963).
3. S. J. Bless, J. Appl. Phys. **43**, 1580 (1972).
4. S. S. Batsanov, Fiz. Goreniya Vzryva **30**, 125 (1994).
5. V. N. Korobenko and A. I. Savvatimskiĭ, Teplofiz. Vys. Temp. **36**, 725 (1998).
6. I. N. Frantsevich, T. R. Balan, A. V. Bochko, *et al.*, Dokl. Akad. Nauk SSSR **218**, 591 (1974).

Translated by G. Merzon

=== **MECHANICS** ===

On Bar Shapes That Are Optimal According to Strength and Stiffness Criteria

N. V. Banichuk*, F. Ragnedda**, and M. Serra**

Presented by Academician D.M. Klimov April 9, 2001

In this paper, we formulate optimization problems for the shape of the cross sections of cylindrical bars. We consider the flexural stiffness, the maximum stress, and the cross-section area of a bar as optimized functionals. The cross-section boundary of the bar, considered as unknown, is sought in the class of regular polygonal contours. Optimal boundaries are found by employing the minimax approaches for cases of simply connected and doubly connected cross sections with given convex holes.

1. Optimization problems for the shape of elastic cylindrical bars are considered in optimal design in order to improve the strength characteristics of the bars under bending, torsion, compression, and other types of static and dynamic loads. Rational and optimal design of the cross sections of bars was considered in a large number of theoretical studies. However, until now, solving many important problems on the optimal design of bar shapes with the use of present-day methods of investigating distributed systems with unknown boundaries encountered certain difficulties. The most complicated problems arising in the optimal design of the bar cross sections are associated with determining admissible cross sections, investigating local extrema, finding global optima, and solving multipurpose optimization problems. A detailed analysis of studies published before 1980 was given in monograph [1]. Variational methods were then used in [2–4] for analyzing the problem on finding convex cross sections for bars that have the maximum flexural and torsional stiffnesses. In [5], parametric representations of boundaries were used for solving the minimization problem for the mass of a thin-walled bar, with restrictions imposed on the minimum torsional and flexural stiffnesses. The problem posed in [6] of finding rational and optimal shapes of beam cross sections, with constraints imposed on the strength, was considered in [7]. The recent study [8]

should also be mentioned, in which the maximization problem was investigated for the torsional stiffness of a composite bar having imperfect matrix–fiber cohesion.

In this study, we investigate such characteristics as the buckling load, the strength, and the stiffness. At first, we consider stiffness properties for the cross sections of a bar, which determine the buckling load under compression and characterize the flexural stiffness of the bar. As is well known, for decreasing deflections of a bent beam and also for increasing the stability–loss critical force (fundamental eigenvalue), it is necessary to increase the moment of inertia of the beam cross section under certain isoperimetric conditions. We assume that the cross-section area S of a cylindrical bar is given $\{S = \text{meas}\,\Omega\}$ and the cross section Ω bounded by the contour Γ is convex. The optimization problem consists in finding the boundary Γ of the domain Ω that maximizes the minimum moment of inertia $I(\Gamma, \alpha)$,

$$I_* = \max_{\Gamma}\min_{\alpha} I(\Gamma, \alpha) \qquad (1)$$

under the isoperimetric condition

$$S(\Gamma) = \int_{\Omega} d\Omega = S_0. \qquad (2)$$

Here, S_0 is a given value of the cross-section area, and α is the angle determining the orientation of the flexural plane. We consider the case when all the bending loads applied to the bar act in the same flexural plane, while the orientation of this plane is not given beforehand and can be chosen arbitrarily. This case is peculiar to compressed columns in which the stability loss takes place in the plane having the minimum flexural stiffness (minimum moment of inertia). In this case, for optimizing the bar stiffness (i.e., the stability–loss critical force), it is necessary to maximize the minimum moment of inertia of the cross section. As was noted in [8] and as follows from the theory of symmetrization [9], in order to optimize the cross-section shape it is necessary to consider a family of admissible symmetric cross sections having the same moments of inertia

———————
* Institute of Problems of Mechanics, Russian Academy of Sciences, pr. Vernadskogo 101, Moscow, 117526 Russia
** Cagliari University, Cagliari, Sardinia, Italy

for arbitrary neutral lines crossing the centroid. It should be noted that an arbitrary regular symmetric cross section [from an equilateral triangle ($n = 3$) and to a circle ($n = \infty$), where n is the number of the polygon sides], has the same moments of inertia with respect to any axes passing through the cross-section center. In what follows, we consider only regular polygonal cross sections with n axes of symmetry and investigate their properties. For the symmetric polygonal cross sections under consideration, their moments of inertia with respect to the axes passing through the centroid turn out to be equal. We have

$$I = \frac{1}{2}(I_x + I_y) = \frac{1}{2}I_p,$$

$$I_p = \int_\Omega \rho^2 d\Omega, \quad \rho^2 = x^2 + y^2,$$

(3)

where I_p is the polar moment of inertia, ρ is the distance from the center (centroid) of the cross section, I_x and I_y are the moments of inertia with respect to the x- and y-axes of the orthogonal coordinate system Oxy, and the point O is the centroid of the cross section. In order to estimate the polar moment of inertia I_p, it is sufficient to consider the triangle OPQ (Fig. 1) having the polar moment of inertia $(I_p)^e$. For the polar moment of inertia of the cross section, we have $I_p = n(I_p)^e$. Introducing a local orthogonal coordinate system $O\eta\zeta$ with the $O\eta$-axis perpendicular to the side PQ, we obtain the relationship $(I_p)^e = (I_\zeta)^e + (I_\eta)^e$, where $(I_\eta)^e = b^3a/48$ and $(I_\zeta)^e = ba^3/4$ are the moments of inertia for the triangle OPQ with respect to the η- and ζ-axes. We denote the lengths of the segments OT and PQ by a and b, respectively (height and side of the triangle). Using the expression for $(I_p)^e$ and the isoperimetric equality $S_0 = n(ba/2)$ following from (2), we sum the quantities $(I_p)^e$ ($e = 1, 2, \ldots, n$). As a result, we obtain the relationships

$$I = \frac{1}{2}I_p = \frac{n}{2}(I_p)^e = S_0^2\varphi(n),$$

(4)

$$\varphi(x) = \frac{\sin^2\left(\frac{\pi}{n}\right) + 3\cos^2\left(\frac{\pi}{n}\right)}{12n\sin\left(\frac{\pi}{n}\right)\cos\left(\frac{\pi}{n}\right)}.$$

(5)

The dependence of the dimensionless moment of inertia $\tilde{I} = I/S_0^2$ on the number n of the sides of polygons is shown in Fig. 2. In what follows, we omit the tildes standing for dimensionless quantities. As can be seen from Fig. 2, the dimensionless moment of inertia I decreases monotonically as the number n tends to infinity and has the maximum value for $n = 3$. Thus, the optimum is attained for an equilateral triangle, while the worst case
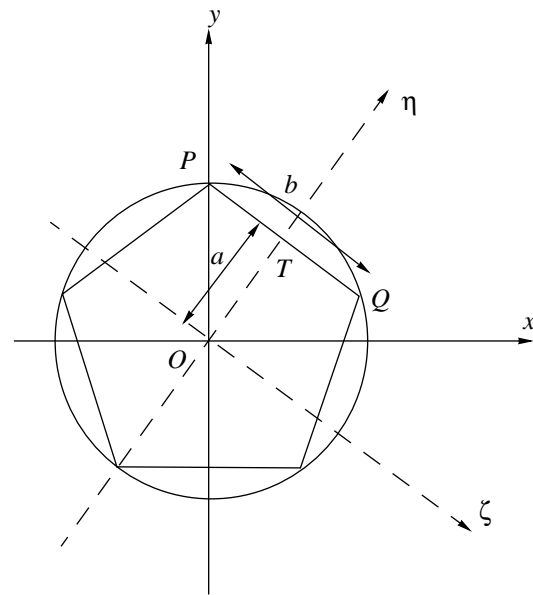

Fig. 1.
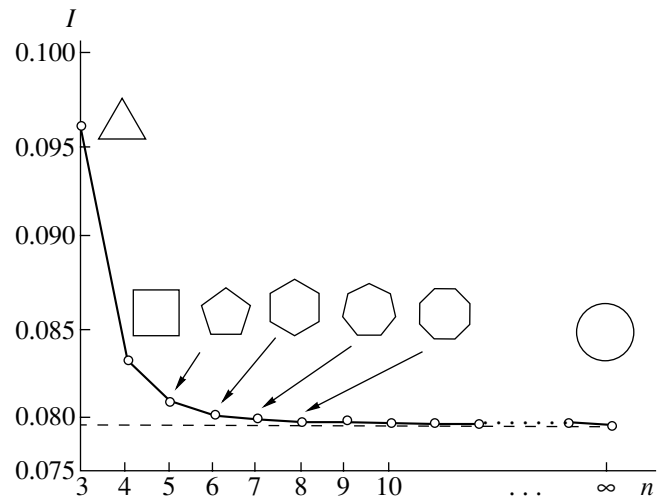
Fig. 2.

corresponds to a circular cross section ($n = \infty$). The fact that a triangular cross section is optimal on the set of all the regular polygonal domains (with the same area) was established in [8], where the problem on finding the column shape providing the maximum stability–loss critical force was investigated. We note that, using the calculus of variations, it is possible to establish that a triangular cross section is locally optimal in the class of symmetric convex regions. We now cite the corresponding considerations. To do this, we apply an arbitrarily small symmetric perturbation, which does not violate either the convexity condition or the isoperimetric constraint $S = S_0$, to the contour Γ bounding the polygonal cross section Ω. The unperturbed region PQR and a third of its perturbed boundary, $P'KT'DQ'$,

Fig. 3.

are shown in Fig. 3. The expression for the variation δI of the moment of inertia I is given by the formula

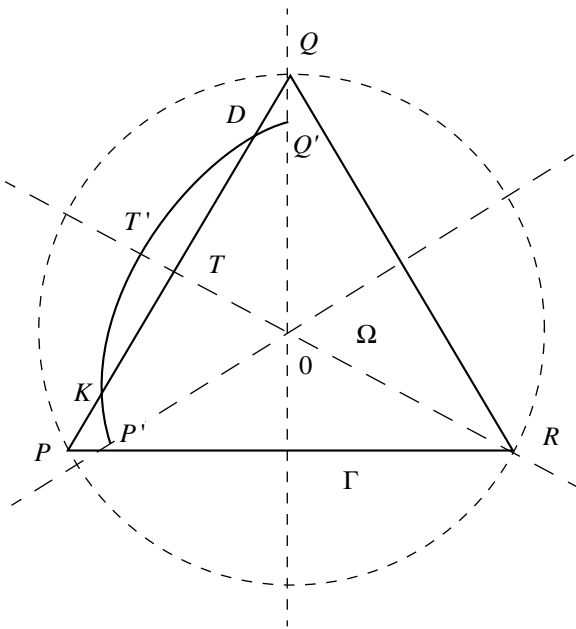$$\delta I = \frac{1}{2}\delta\int_{\Omega}\rho^2 d\Omega = \frac{1}{2}\int_{\Gamma}\rho^2\delta f\, d\Gamma, \tag{6}$$

where δf is the variation of the boundary of the cross section, which is measured in the direction of the outward normal to Γ. Allowing for the symmetry of both the unperturbed region of the cross section and the perturbed boundary with respect to the symmetry axes (shown in Fig. 3 by the dashed lines), we write the expressions for the variations of the moment of inertia and the cross-section area:

$$\delta I = 3\left(\int_{P}^{K}\rho^2\delta f\, d\Gamma + \int_{K}^{T}\rho^2\delta f\, d\Gamma\right), \tag{7}$$

$$\delta S = 6\left(\int_{P}^{K}\delta f\, d\Gamma + \int_{K}^{T}\delta f\, d\Gamma\right). \tag{8}$$

Formula (8) and the isoperimetric condition $S = S_0$ ($\delta S = 0$) lead to the relationship

$$\int_{P}^{K}\delta f\, d\Gamma = -\int_{K}^{T}\delta f\, d\Gamma. \tag{9}$$

Using Eq. (9) and the inequality

$$(\rho^2)_{PK} \geq (\rho^2)_K, \quad (\rho^2)_{KT} \leq (\rho^2)_K, \tag{10}$$

we arrive at the following estimates:

$$\delta I \leq 3\left\{(\rho^2)_K\int_{P}^{K}\delta f\, d\Gamma + (\rho^2)_K\int_{K}^{T}\delta f\, d\Gamma\right\}$$

$$= 3(\rho^2)_K\left(\int_{P}^{K}\delta f\, d\Gamma + \int_{K}^{T}\delta f\, d\Gamma\right) = 0. \tag{11}$$

Thus, $\delta I \leq 0$ and, therefore, the local maximum of the optimized functional corresponds to a triangular cross section.

We now assume that the cross section Ω is a doubly connected region; i.e., the bar has a cylindrical cavity. The region Ω has the given inner boundary Γ_i and the outer polygonal boundary Γ. We also assume that the inner region Ω_i, bounded by the contour Γ_i, is convex and has the same moments of inertia with respect to all the axes lying in the cross section and crossing the centroid. We suppose that the area S of the cross section Ω is given ($S = S_0$) and that the boundary of the equilateral triangle with the area $S = S_i + S_0$ [$S_i + S_0 = \text{meas}(\Omega_i + \Omega_0)$] does not touch or intersect the boundary Γ_i. The last condition is essential when considering the variations of the outer boundary Γ in the class of regular polygons. On the set of the boundaries Γ under consideration, the minimum distance between Γ and the centroid is attained for an equilateral triangle. Under these assumptions, an unknown outer boundary Γ is found from the optimum condition for the moment of inertia I of the cross section Ω. The expression for the moment of inertia I can be written as $I(n) = I_s(n) - I_i$. Here, I_s is the moment of inertia of the simply connected region $\Omega_i + \Omega$, which depends on the number n, and I_i is the moment of inertia of the inner convex region Ω_i, whose value is independent of n. The optimization problem is reduced to the maximization of the quantity $I_s(n)$. We have

$$I_* = \max_{n}I(n) = \max_{n}\{I_s(n)\} - I_i = I_s(3) - I_i. \tag{12}$$

Thus, the equilateral triangle with its center in the centroid of the cross section Ω_i is the optimal cross section.

2. Above, we considered the optimization problem for the stiffness of a bar, which was reduced to the maximization of integral functionals. Below, we analyze the maximization problem for the strength of a bar, which is based on estimating local functionals. We consider the minimization problem for the bending stresses in cylindrical bars having convex cross sections. As before, we assume that both the flexural plane and the plane in which external forces act are not known beforehand. The limiting value M_0 of the acting bending moment is considered as given. We allow for only

normal stresses acting in the bar cross sections. They are determined by the formula

$$\sigma(x, y, \Gamma, \beta) = M_0 \frac{h(x, y, \beta)}{I(\Gamma, \beta)}. \tag{13}$$

Here, the angle β specifies the direction of the neutral line of the cross section relative to the global coordinate system, and h is the distance between the point (x, y) under consideration and the neutral line of the bar. The optimization problem consists of finding the boundary Γ of the cross section Ω that minimizes the maximum stress

$$\sigma_* = \min_{\Gamma} \max_{\beta} \max_{(x, y) \in \Omega} \sigma(x, y, \Gamma, \beta) \tag{14}$$

under isoperimetric condition (2). In the case of fixed Γ and β, we denote the maximum values of h and σ on Ω by h_m and σ_m, respectively; i.e.,

$$h_m = h_m(\Gamma, \beta) = \max_{(x, y) \in \Omega} h(x, y, \beta), \tag{15}$$

$$\sigma_m = \sigma_m(\Gamma, \beta) = \frac{M_0}{I(\Gamma, \beta)} h_m. \tag{16}$$

As above, we consider only symmetric convex cross sections bounded by regular polygons. In this case, the moment of inertia is independent of β [$I = I(\Gamma)$], while the maximum value of h for the set of β ($0 \le \beta \le 2\pi$) and $(x, y) \in \Omega$ is given by the formula

$$\max_{\beta} h_m(\Gamma, \beta) = \max_{\beta} \max_{(x, y)} h(x, y, \beta)$$
$$= \frac{S_0^{1/2}}{\sqrt{n \sin\left(\frac{\pi}{n}\right) \cos\left(\frac{\pi}{n}\right)}}, \tag{17}$$

where n is the number of sides of the polygon under consideration. Isoperimetric condition (2) is taken into account when deriving expression (17). Furthermore, using formulas (4) and (17), we find the maximum value of the quantity σ in the form

$$\sigma_M = \max_{\beta} \sigma_m = \frac{M_0}{I} \max_{\beta} h_m(\Gamma, \beta) = \frac{M_0}{S_0^{3/2}} \psi(n),$$

$$\psi(n) \equiv \frac{12 \sqrt{n \sin\left(\frac{\pi}{n}\right) \cos\left(\frac{\pi}{n}\right)}}{\sin^2\left(\frac{\pi}{n}\right) + 3 \cos^2\left(\frac{\pi}{n}\right)}. \tag{18}$$

The dependence of the maximum stress σ_M on the number n is shown in Fig. 4, where the dimensionless quantity $\tilde{\sigma}_M = \sigma_M M_0^{-1} S_0^{3/2}$ is used, and the tilde, standing for the dimensionless variable, is omitted. As can be seen
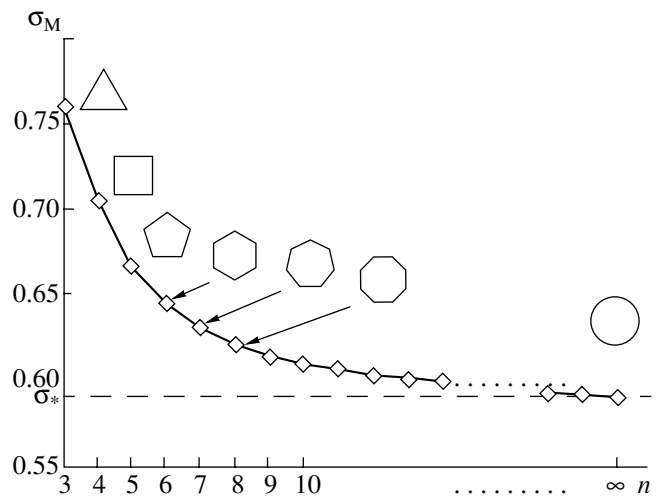
Fig. 4.

from Fig. 4, the maximum stress $\sigma_M = \Psi(n)$ decreases monotonically as n tends to infinity, taking the minimum value at $n = \infty$. Consequently, the optimum is realized in the case of a circular cross section and the worst case corresponds to a equilateral triangle ($n = 3$).

It is possible to show that a circular cross section provides the local minimum of the optimized functional. In order to prove this statement, we consider the circular cross section Ω and perform small symmetric variations of its boundary Γ, which do not violate the convexity condition and isoperimetric constraint (2) ($S = S_0$). For the sake of simplicity and without loss of generality, we assume that the perturbed boundary $\Gamma + \delta\Gamma$ has three axes of symmetry. The small variation of the optimized functional is given by the following expression:

$$\delta\sigma_M = \frac{1}{I} \delta h_m - \frac{h_m}{I^2} \delta I. \tag{19}$$

With regard to both the expression for the small variation of the area S of the circular region under consideration and the isoperimetric condition, we have

$$\int_{\Gamma} \delta f \, d\Gamma = 0. \tag{20}$$

Using equality (20), we estimate the first variation of the moment of inertia:

$$\delta I = \frac{1}{2} \int_{\Gamma} \rho^2 \delta f \, d\Gamma = \frac{\rho^2}{2} \int_{\Gamma} \delta f \, d\Gamma = 0. \tag{21}$$

Here we take into account that the function $\rho(x, y)$ is constant at the boundary Γ (ρ is the radius of the circular cross section). Thus, the second term in expression (19) vanishes. The variation of the quantity h_m is less than or equal to zero ($\delta h_m \le 0$). Therefore, for perturbances

under consideration of a circular cross section, the following inequality is valid:

$$\delta\sigma_M = \frac{1}{I}\delta h_m \leq 0. \tag{22}$$

As with the former part of this study, the considerations carried out can be extended to the case of doubly connected cross sections.

ACKNOWLEDGMENTS

REFERENCES

1. N. V. Banichuk, *Optimization of Shapes of Elastic Bodies* (Nauka, Moscow, 1980).

2. B. L. Karihaloo and W. S. Hemp, Eng. Opt. **11**, 39 (1987).

3. B. L. Karihaloo and W. S. Hemp, Eng. Opt. **10**, 289 (1987).

4. B. L. Karihaloo and W. S. Hemp, Proc. R. Soc. London, Ser. A **409**, 67 (1987).

5. B. L. Karihaloo and W. S. Hemp, Report 1438/82 (Univ. Oxford; Dept. Eng. Sci., Oxford, 1982), pp. 1–10.

6. A. Yu. Ishlinskiĭ, Nauchn. Zap. Mosk. Gos. Univ., Mekh., No. 39, 87 (1940).

7. N. V. Banichuk and V. V. Kobelev, Izv. Akad. Nauk SSSR, Mekh. Tverd. Tela, No. 1, 162 (1983).

8. J. B. Keller, Arch. Ration. Mech. Anal. **5** (4), 275 (1960).

9. G. Pólya and G. Szegö, *Isoperimetric Inequalities in Mathematical Physics* (Princeton Univ. Press, Princeton, 1951).

Translated by V. Bukhanov

$=\!=\!=\!=\!=\!=\!=\!=$ **MECHANICS** $=\!=\!=\!=\!=\!=\!=\!=$

On the Shear Correction Factor in the Timoshenko-Type Shell Theory

Corresponding Member of the RAS É. I. Grigolyuk* and G. M. Kulikov**

Received June 21, 2001

As is well known, in the theory of Timoshenko-type shells the shear correction factors k are introduced to allow for the nonuniformity of the transverse-shear distribution in shell cross sections [1]. At present, the following values are commonly used for the shear correction factors: $k = \dfrac{5}{6}$ [2] and $k = \dfrac{\pi^2}{12}$ [3]. These correction factors were obtained as a result of analysis of thin elastic plates and are consistent with one another. As is shown below, in the case of the approach [3] (in which the derivation of governing relations is based on the principle of virtual work), the value of the shear correction factor $k = 1$ is preferable. In this case, the transverse components of the stress tensor can be recovered by integrating equations of the spatial elasticity theory. The choice $k = 1$ makes it possible to construct a mathematically consistent and noncontradictory theory of Timoshenko-type shells.

1. We consider a thin anisotropic shell with a constant thickness h. It is assumed that at each shell point there exists a surface of elastic symmetry that is parallel to face surfaces S^- and S^+. We take as a reference surface S an arbitrary internal shell surface located at the distances δ^- and δ^+ from the face surfaces; i.e., $h = \delta^+ - \delta^-$. We associate the reference surface with orthogonal coordinates α_1 and α_2, which are counted off along the lines of principal curvatures. The α_3-coordinate is counted off in the direction of increasing the outer normal to the surface S.

In linear elasticity theory, the equations of equilibrium for a thin shell whose face-surface metrics can be identified with the metric of the reference surface have the form

$$\frac{1}{A_i}\frac{\partial \sigma_{ii}}{\partial \alpha_i} + \frac{1}{A_j}\frac{\partial \sigma_{ij}}{\partial \alpha_j} + \frac{\partial \sigma_{i3}}{\partial \alpha_3}$$

---
* *Moscow State Technical University (MAMI), Bol'shaya Semenovskaya ul. 38, Moscow, 105023 Russia*
** *Tambov State Technical University, Sovetskaya ul. 106, Tambov, 392620 Russia*

$$+ B_i(\sigma_{ii} - \sigma_{jj}) + 2B_j\sigma_{ij} + k_i\sigma_{i3} = 0, \quad i \neq j,$$

$$\frac{1}{A_1}\frac{\partial \sigma_{13}}{\partial \alpha_1} + \frac{1}{A_2}\frac{\partial \sigma_{23}}{\partial \alpha_2} + \frac{\partial \sigma_{33}}{\partial \alpha_3} \qquad (1)$$

$$+ B_1\sigma_{13} + B_2\sigma_{23} - k_1\sigma_{11} - k_2\sigma_{22} = 0.$$

Here, $B_i = \dfrac{\partial A_j/\partial \alpha_i}{A_1 A_2}$; $\sigma_{\alpha\beta}$ are stresses; A_i and k_i are the Lamé parameters and curvatures of the coordinate lines, respectively; $i, j = 1, 2$; and $\alpha, \beta = 1, 2, 3$.

The equations of the generalized Hooke law with allowance for the admission $\sigma_{33} \ll \sigma_{ij}$ can be written out in the form

$$\sigma_{ij} = \sum_{l \leq m} b_{ijlm}\varepsilon_{lm}, \quad \sigma_{i3} = \sum_{l} b_{i3l3}\varepsilon_{l3}, \qquad (2)$$

$$i, j, l, m = 1, 2.$$

In constructing the theory, we employ the modified Timoshenko hypothesis [4] on the linear distribution of displacements across the shell thickness

$$u_i = N^-(\alpha_3)v_i^- + N^+(\alpha_3)v_i^+, \quad u_3 = v_3,$$

$$N^-(\alpha_3) = \frac{\delta^+ - \alpha_3}{h}, \quad N^+(\alpha_3) = \frac{\alpha_3 - \delta^-}{h}, \qquad (3)$$

where $v_i^\pm(\alpha_1, \alpha_2)$ are tangential displacements of the face surfaces $S^\pm$, and $v_3(\alpha_1, \alpha_2)$ is the transverse displacement of the surface S.

We now introduce displacements (3) into the strain-displacement relations of the linear elasticity theory. Then, assuming the transverse shears to be distributed uniformly across the shell thickness, we arrive at the expressions

$$\varepsilon_{ij} = N^-(\alpha_3)e_{ij}^- + N^+(\alpha_3)e_{ij}^+, \quad \varepsilon_{i3} = e_{i3}, \quad \varepsilon_{33} = 0,$$

$$e_{ii}^\pm = \frac{1}{A_i}\frac{\partial v_i^\pm}{\partial \alpha_i} + B_j v_j^\pm + k_i v_3 \quad i \neq j,$$

$$e_{12}^{\pm} = \frac{1}{A_1}\frac{\partial v_2^{\pm}}{\partial \alpha_1} + \frac{1}{A_2}\frac{\partial v_1^{\pm}}{\partial \alpha_2} - B_2 v_1^{\pm} - B_1 v_2^{\pm}, \qquad (4)$$

$$e_{i3} = \beta_i - \theta_i, \quad \beta_i = \frac{1}{h}(v_i^+ - v_i^-),$$

$$\theta_i = k_i v_i - \frac{1}{A_i}\frac{\partial v_3}{\partial \alpha_i}, \quad v_i = \frac{1}{2}(v_i^- + v_i^+).$$

We multiply first two equations of equilibrium (1) by the shape functions $N^{\pm}(\alpha_3)$ and integrate them (together with the third equation) with respect to the transverse coordinate within the limits from δ^- to δ^+, with the boundary conditions $\sigma_{\alpha 3}(\delta^{\pm}) = p_{\alpha}^{\pm}$ taken into account. As a result, we arrive at the equations of equilibrium for a shell with respect to the stress resultants

$$\frac{1}{A_i}\frac{\partial H_{ii}^{\pm}}{\partial \alpha_i} + \frac{1}{A_j}\frac{\partial H_{ij}^{\pm}}{\partial \alpha_j} + B_i(H_{ii}^{\pm} - H_{jj}^{\pm})$$

$$+ 2B_j H_{ij}^{\pm} + \left(\frac{1}{2}k_i \mp \frac{1}{h}\right)T_{i3} = \mp p_i^{\pm}, \quad i \neq j,$$

$$\frac{1}{A_1}\frac{\partial T_{13}}{\partial \alpha_1} + \frac{1}{A_2}\frac{\partial T_{23}}{\partial \alpha_2} + B_1 T_{13} + B_2 T_{23} \qquad (5)$$

$$- k_1 T_{11} - k_2 T_{22} = p_3^- - p_3^+,$$

$$H_{ij}^{\pm} = \int_{\delta^-}^{\delta^+} \sigma_{ij} N^{\pm}(\alpha_3)d\alpha_3, \quad T_{i\alpha} = \int_{\delta^-}^{\delta^+} \sigma_{i\alpha} d\alpha_3.$$

Here, $T_{i\alpha}$ and $H_{ij}^{\pm}$ are the classical and generalized stress resultants, respectively, and $p_{\alpha}^{\pm}$ are the surface loads acting on the face surfaces $S^{\pm}$.

With allowance for relationships (2), the constituting equations for specific forces and moments can be represented in the form

$$H_{ij}^- = \frac{1}{6}h\sum_{l \leq m} b_{ijlm}(2e_{lm}^- + e_{lm}^+),$$

$$H_{ij}^+ = \frac{1}{6}h\sum_{l \leq m} b_{ijlm}(e_{lm}^- + 2e_{lm}^+), \qquad (6)$$

$$T_{ij} = H_{ij}^- + H_{ij}^+, \quad T_{i3} = h\sum_l k_{il}b_{i3l3}e_{l3},$$

where we assumed $k_{il} = 1$ for the shear correction factors. We should note that formula (6) for the transverse forces T_{i3} expresses a rather simple fact. This formula implies that the elasticity relations for the transverse shear stresses (2) in the Timoshenko-type shell theory are not satisfied pointwise but are fulfilled as integral relations across the shell thickness [4, 5].

Furthermore, we integrate Eqs. (1) of the spatial elasticity theory over the transverse coordinate from δ^- to α_3. Taking into account the boundary conditions $\sigma_{\alpha 3}(\delta^-) = p_{\alpha}^-$, we arrive at the formulas for the determination of the stress transverse components

$$\sigma_{i3} = p_i^- - \frac{1}{A_i}\frac{\partial Q_{ii}}{\partial \alpha_i} - \frac{1}{A_j}\frac{\partial Q_{ij}}{\partial \alpha_j}$$

$$- B_i(Q_{ii} - Q_{jj}) - 2B_j Q_{ij} - k_i Q_{i3}, \quad i \neq j, \qquad (7)$$

$$\sigma_{33} = p_3^- - \frac{1}{A_1}\frac{\partial Q_{13}}{\partial \alpha_1} - \frac{1}{A_2}\frac{\partial Q_{23}}{\partial \alpha_2}$$

$$- B_1 Q_{13} - B_2 Q_{23} + k_1 Q_{11} + k_2 Q_{22},$$

$$Q_{i\alpha} = \int_{\delta^-}^{\alpha_3} \sigma_{i\alpha} d\alpha_3. \qquad (8)$$

We pay attention to the fact that, by virtue of the equality $Q_{i\alpha}(\delta^+) = T_{i\alpha}$ and equations of equilibrium (5), the boundary conditions $\sigma_{\alpha 3}(\delta^+) = p_{\alpha}^+$ immediately follow from relationships (7).

2. We now discuss a statement important for the theory of Timoshenko-type shells and associated with the validity of equations of equilibrium (5) for a shell in the case of the stress field (2), (7), which was found as a result of solving the problem. The matter is that upon the determination of the transverse shear stresses σ_{i3} according to formula (7) and the calculation on this basis of the transverse forces T_{i3}^s, we can encounter a situation when listed equations of equilibrium (5) for a shell are not exactly satisfied. The reason consists in the fact that the transverse forces T_{i3}, whose calculation is based on Hooke law (2), i.e., on formula (6), in the general case, can be not coincident with T_{i3}^s.

In order to solve the problem posed, we employ the formulas following from relationships (2), (4), and (8):

$$\int_{\delta^-}^{\delta^+} Q_{ij}d\alpha_3 = hH_{ij}^-, \quad \int_{\delta^-}^{\delta^+} Q_{i3}d\alpha_3 = \frac{1}{2}hT_{i3}.$$

With allowance for these formulas, as well as for relation (7), we obtain the expression

$$T_{i3}^s = \int_{\delta^-}^{\delta^+} \sigma_{i3}d\alpha_3 = h\left[p_i^- - \frac{1}{A_i}\frac{\partial H_{ii}^-}{\partial \alpha_i} - \frac{1}{A_j}\frac{\partial H_{ij}^-}{\partial \alpha_j}\right.$$

$$\left. - B_i(H_{ii}^- - H_{jj}^-) - 2B_j H_{ij}^- - \frac{1}{2}k_i T_{i3}\right], \quad i \neq j. \qquad (9)$$

With equations of equilibrium (5) for a shell taken into account, we have from Eq. (9) that $T_{i3}^s = T_{i3}$, which was in need of proof.

In conclusion, it is worth emphasizing that we managed to construct the noncontradictory theory for Timoshenko-type shells [in the sense of the simultaneous satisfaction of the equations of equilibrium for a shell (5) and relationships (7)]. Such a construction became possible on the basis of a physically clear assumption about the integral validity of equations corresponding to the Hooke law for transverse shear stresses (2). This implies that we should admit $k_{il} = 1$ in formula (6) for transverse forces. In this connection, we note that, from the standpoint of the approach developed in this paper, attempts to construct theories for Timoshenko-type shells, which are based on one concept or another related to calculation methods for the shear correction factors [1], will result in mathematically inconsistent and contradictory theories.

REFERENCES

1. É. I. Grigolyuk and I. T. Selezov, *Mechanics of Deformable Solids,* Vol. 5: *Nonclassical Theories of Oscillations of Bars, Plates and Shells* (VINITI, Moscow, 1973).

2. E. Reissner, J. Math. Phys. **23** (4), 184 (1944).

3. R. D. Mindlin, J. Appl. Mech. **18** (1), 31 (1951).

4. G. M. Kulikov, J. Eng. Mech. **127** (2), 119 (2001).

5. É. I. Grigolyuk and G. M. Kulikov, *Multi-Layer Reinforced Shells: Analysis of Pneumatic Tires* (Mashinostroenie, Moscow, 1988).

Translated by G. Merzon

========================= **MECHANICS** =========================

Electrocapillary-Vortex Model
for a Hill–Taylor Spherical Vortex

V. L. Natyaganov

Presented by Academician E.I. Shemyakin March 26, 2001

In the classical setting, the problem of the electro-capillary motion of a spherical droplet [1] with a surface charge of the double electrical layer is described in dimensionless variables by the system of equations [2]

$$r > 1: \quad \Delta\varphi = 0, \quad \Delta\mathbf{u} = \nabla p, \quad \mathrm{div}\,\mathbf{u} = 0;$$

$$r < 1: \quad \Delta\varphi' = 0, \quad \Delta\mathbf{u}' = \nabla p', \quad \mathrm{div}\,\mathbf{u}' = 0;$$

$$r \to 0: \quad |\nabla\varphi'|, |\mathbf{u}'|, |\nabla p'| < \infty;$$

$$r \to \infty: \quad \mathbf{u} \to u_e \mathbf{k}, \quad \nabla\varphi \to -\mathbf{k}; \qquad (1)$$

$$r = 1: \quad u_n = u_n' = 0, \quad u_\theta = u_\theta' = -v_0 \sin\theta,$$

$$-\frac{\partial\varphi}{\partial r} + \mathrm{div}_\Sigma \mathbf{j}_\Sigma = 0, \quad \sigma_* \frac{\partial\varphi'}{\partial r} + \mathrm{div}_\Sigma \mathbf{j}_\Sigma' = 0,$$

$$\eta_* p_{n\theta}' = p_{n\theta} - q\nabla_\Sigma(\varphi - \varphi').$$

Here, $\sigma_* = \dfrac{\sigma'}{\sigma}$, $\eta_* = \dfrac{\eta'}{\eta}$ are the ratios for the coefficients of the electrical conduction and dynamic viscosity; q is the dimensionless charge density in the double electrical layer; $\mathbf{j}_\Sigma = \pm q\mathbf{v}_\theta$ is the convective surface current for each of two oppositely charged surfaces of the thin double electrical layer, $\left(\dfrac{d}{a} \ll 1,\, d\right.$ is the thickness of the double electrical layer, and a is the droplet radius$\Big)$; u_e is the unknown dimensionless velocity of the droplet electrocapillary motion, which is normalized to $E_0 a \sqrt{\dfrac{\sigma}{\eta}}$; and E_0 is the intensity of an external electric field. Other characteristic quantities correspond to those taken in [2].

The solution to this problem yields a potential flow outside the droplet and a spherical Hill vortex inside it.

At the same time, the distribution of the electric potential has the form

$$\varphi' = -\frac{2q v_0}{\sigma_*} r\cos\theta, \quad \varphi = \left(-r + \frac{\beta}{r^2}\right)\cos\theta,$$

where $\beta = q v_0 - 1/2$ and the fluid velocity v_0 on the droplet surface is connected with u_e by the formula

$$u_e = \frac{2}{3} v_0 = \frac{q}{2 + 3\eta_* + q^2(1 + 2/\sigma_*)}.$$

However, we can go out of the usual framework for electrodynamics and obtain the final solution to this problem in the electrical approximation [3]. In other words, we seek the magnetic field **B** induced by the flowing electric currents. Then, we take into account in the equations of motion the existence of the magnetic component of the Lorentz force (that arises due to the interaction of these currents with the self-magnetic field) on the basis of the theory of electrovortex flows [4]. In this case, we can find several new effects.

1. Taking the quantity $B_0 = \mu\sigma a E_0$ as a characteristic induction of the self-magnetic field, and after certain transformations, we arrive at the system of equations

$$\begin{cases} \mathrm{rot}\,\mathbf{B} = \mathbf{j} \\ \mathrm{div}\,\mathbf{B} = 0 \end{cases} \Rightarrow \begin{cases} r > 1: \mathbf{B} = \dfrac{1}{2} r\left(1 + \dfrac{2\beta}{r^3}\right)\sin\theta\,\mathbf{e}_\varphi \\ r < 1: \mathbf{B}' = q v_0 r \sin\theta\,\mathbf{e}_\varphi. \end{cases} \quad (2)$$

In this case, at the passage through the electric-current layers of a mobile double electrical layer, the jump of the magnetic-field induction is $\{\mathbf{B}\} = 0$ as $r = 1$. However, it is well known from the courses of electrodynamics (see, e.g., [3, 5]) and magnetic hydrodynamics [6] that the tangential component of the magnetic field **B** has a discontinuity when passing through an electric-current layer.

This illusory contradiction can be overcome due to the fact that, in the presence of the relative motion of phases, the double electric layer corresponds to the vec-

Moscow State University,
Vorob'evy gory, Moscow, 119899 Russia

tor double current layer (DCL), inside of which (as $\dfrac{d}{a} \longrightarrow 0$) there is a simple magnetic layer (SML) similar to the surface δ-function with the induction $\mathbf{B}_\Sigma = -qv_0\sin\theta\mathbf{e}_\varphi$. This conclusion is confirmed by the solution (within the accuracy to the small parameter $\dfrac{d}{a} \ll 1$) to the interior Dirichlet problem for a magnetic field inside a spherical layer.

Thus, a new structure arises, namely, a vector triple electromagnetic layer (TEML) with the meridional and antiparallel spreading of the convective electric current in the double current layer. This structure is accompanied by the appearance of the orthogonal azimuth magnetic field in the simple magnetic layer. This can be written out in the following symbolic form:

$$\mathrm{TEML = DCL \cup SML.}$$

In addition, a direct verification of other properties of the triple electromagnetic layer as a generalizing unification of classical concepts for potentials of double and simple layers [5–7] is possible.

2. In the electrodynamic approximation, the electrovortex flow caused by the Lorentz force is described by the equation

$$\Delta\mathbf{u}_1 + M\cdot[\mathbf{j}\times\mathbf{B}] = \nabla p_1, \tag{3}$$

where $\mathbf{j} = -\nabla\varphi$ and $\mathbf{B}$ are determined by formulas (2). The Hartmann number M calculated on the basis of the induction B_0 of the self-magnetic field of the electric current $\mathbf{j}$ is connected with the Alfven number Al, the Reynolds number Re, and the electrovortex-flow parameter S by the following relations:

$$B_0 a\sqrt{\frac{\sigma}{\eta}} = \mathrm{M} = \mathrm{Al}\cdot\mathrm{Re} = \frac{S}{\mathrm{Re}} = \mu j a^2\sqrt{\frac{\sigma}{\eta}}.$$

The application of the curl operation to Eq. (3) with both the expression for the Lorentz force and the axial symmetry taken into consideration makes it possible to derive the inhomogeneous equation for the stream function $\Psi(r,\theta)$ outside a droplet

$$\frac{1}{r\sin\theta}\left(\frac{\partial^2}{\partial r^2} + \frac{\sin\theta}{r^2}\frac{\partial}{\partial\theta}\left(\frac{1}{\sin\theta}\frac{\partial}{\partial\theta}\right)\right)^2\Psi$$
$$= \frac{3\beta}{r^3}\left(1 + \frac{2\beta}{r^3}\right)\sin\theta\cos\theta. \tag{4}$$

By virtue of the potential properties of the Lorentz force for $r < 1$, a similar homogeneous equation can also be obtained for the interior of the droplet.

The form of the angular dependence in the right-hand side of Eq. (4) allows us to seek the stream func-

tion and the tangential component of the electrovortex flow on the droplet surface in the form

$$\Psi(r,\theta) = f(r)\sin^2\theta\cos\theta,$$

$$u_{1\theta} = u'_{1\theta} = -v_1\sin\theta\cos\theta.$$

With allowance for the corresponding modification of the boundary conditions related to the system of equations (1) as $r \longrightarrow \infty$ and $r = 1$, we finally obtain

$$\Psi = \frac{M\beta}{8}\left(r^2 - \frac{2\beta}{r} + A_0 + \frac{C_2}{r^2}\right)\sin^2\theta\cos\theta,$$

$$\Psi' = M\beta A_3(r^5 - r^3)\sin^2\theta\cos\theta, \tag{5}$$

$$\varphi_1 = \frac{\beta_2}{r^3}P_2(\cos\theta), \quad \varphi'_1 = \alpha_2 r^2 P_2(\cos\theta),$$

where

$$A_0 = \beta - 2 + \frac{4v_1}{\beta M}, \quad C_2 = 1 + \beta - \frac{4v_1}{\beta M}, \quad A_3 = \frac{v_1}{2\beta M},$$

$$\alpha_2 = -\frac{qv_1}{\sigma_*}, \quad \beta_2 = \frac{2}{3}qv_1,$$

$$v_1 = \frac{M\beta(\beta+4)}{20\left[1 + \eta_* + \dfrac{q^2}{5}\left(2 + \dfrac{3}{\sigma_*}\right)\right]}.$$

Outside the droplet, the velocity field of the electrovortex flow, which corresponds to stream functions (5), presents an analog of the axisymmetric deformation flow, while in the droplet interior we deal with the system of Taylor toroidal vortices. The summary electrocapillary vortex motion inside a droplet has the form of a spherical Hill–Taylor vortex.

3. The electrocapillary flow formally found in [1, 2] corresponds to the Stokes approximation (Re $\ll$ 1). At the same time, the potential flow outside a droplet and the Hill spherical vortex inside it are related to the class of dynamically reversible flows and satisfy the complete Navier–Stokes equations [8]. Then, the electrovortex flow found as a correction to the electrocapillary flow takes place for all values of the parameter S for which the breakdown of the double electrical layer does not even occur. Therefore, ball lightning composed of cold or cluster plasma can also have a similar electrocapillary-vortex structure. This ball lightning can be a cluster of the spherical Hill–Taylor-vortex type. The cluster can possess the surface triple electromagnetic layer at the interface that bounds the phases and the ambient ionized air and can participate in the above-described (or more complicated) motion. This model of ball lightning makes it possible to qualitatively explain many strange characteristic features intrinsic to its nature [9].

REFERENCES

1. V. G. Levich, *Physicochemical Hydrodynamics* (Fizmatgiz, Moscow, 1959).

2. V. L. Natyaganov and I. V. Oreshina, Kolloidn. Zh. **62** (1), 90 (2000).

3. V. V. Tolmachev, A. M. Golovin, and V. S. Potapov, *Thermodynamics and Electrodynamics of Continuous Medium* (Mosk. Gos. Univ., Moscow, 1988).

4. V. V. Boyarevich, Ya. Zh. Freĭberg, E. I. Shilova, and É. V. Shcherbinin, *Electrovortex Flows* (Zinatne, Riga, 1985).

5. I. E. Tamm, *The Principles of Electricity Theory* (Nauka, Moscow, 1989).

6. J. A. Shercliff, *Textbook of Magnetohydrodynamics* (Pergamon, Oxford, 1965; Mir, Moscow, 1967).

7. V. S. Vladimirov, *Equations of Mathematical Physics* (Nauka, Moscow, 1971; Marcel Dekker, New York, 1971).

8. G. K. Batchelor, *An Introduction to Fluid Dynamics* (Cambridge Univ. Press, Cambridge, 1967; Mir, Moscow, 1973).

9. I. P. Stakhanov, *On Physical Nature of Ball Lightning* (Nauchnyĭ Mir, Moscow, 1996).

Translated by G. Merzon

===================== **MECHANICS** =====================

Surface of a Taylor Bubble in Vertical Cylindrical Flows

T. R. Nigmatulin
Presented by Academician R.F. Ganiev February 20, 2001

A missile flow is one of the complicated and often-encountered regimes of two-phase flows. In a vertical missile flow, a major fraction of gas is enclosed in a large bulletlike bubble, which is called a Taylor bubble. This bubble occupies the greater part of the pipe cross section. Fluid between the Taylor bubble and the pipe wall flows around this bubble as a thin film. Taylor bubbles are separated by continuous fluid portions, which can contain small bubbles. The shape of the interphase surface in two-phase flows specifies the exchange by the mass, momentum, and energy between the phases.

THEORETICAL DESCRIPTION OF THE TAYLOR BUBBLE SHAPE

If a Taylor bubble is more than five times longer than the diameter of the pipe with the missile flow, the bubble can be separated into three parts so that the Taylor bubble shape can be described by three asymptotes (as is shown in Fig. 1).

The surface of the first part (bow) of the bubble is spherical. The radius of this surface is equal to $\frac{3}{8}D$, where D is the pipe diameter. The surface of this part can be described in the cylindrical coordinates (r, x) by the following equation [1]:

$$r = \frac{D}{2} - \frac{1}{2}\sqrt{x(3D - 4x)}. \qquad (1)$$

The second part of the Taylor bubble can be described by the equation derived in [2] under the assumption on the free fall of a perfect fluid:

$$r = \frac{D}{2}\sqrt{1 - \frac{u_g}{\sqrt{2gx}}}. \qquad (2)$$

Here, D is the pipe diameter, u_g is the emersion velocity of the bubble in the pipe with the quiescent fluid, and g is the acceleration of gravity.

At the third part of the Taylor bubble, the falling-fluid layer becomes so thin that the gravity force is balanced by viscous forces. Therefore, the layer thickness

becomes constant and can be represented by the equation derived in [3]:

$$\delta = \sqrt[3]{\frac{\nu_l^2}{g}}, \qquad (3)$$

where ν_l is the kinematic viscosity of the fluid. This part begins at a distance on the order of five pipe diameters from the bow part of the bubble, and the layer thickness depends on the properties of the gas and liquid phases of the flow.

EXPERIMENTAL INVESTIGATION

Our experiments were carried out with the setup shown in Fig. 2. A solitary Taylor bubble was formed in

$$R = \frac{3}{8}D \quad [1]$$

$$\delta = \frac{D}{2} - \sqrt{1 - \frac{u_g}{\sqrt{2gx}}} \quad [2]$$

$$\delta = \delta_\infty \quad [4]$$
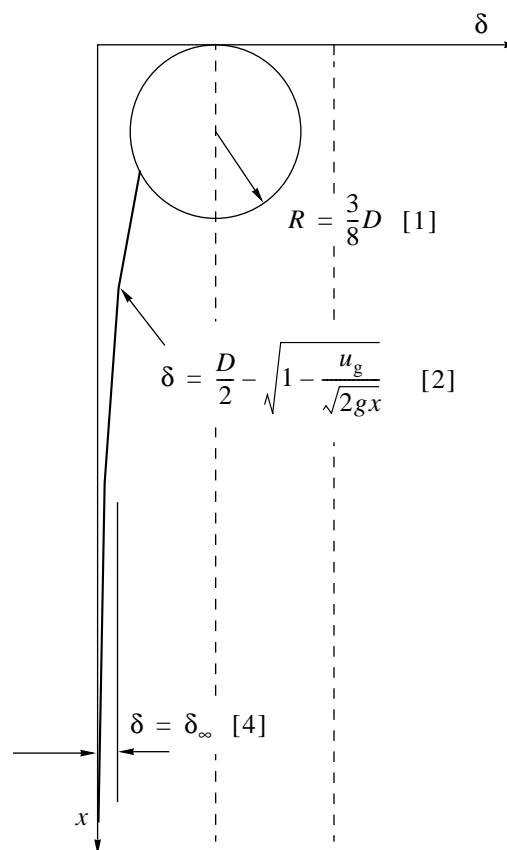
Fig. 1. Asymptotic shapes of the Taylor bubble.

Research Center for Nonlinear Mechanics and Technology,
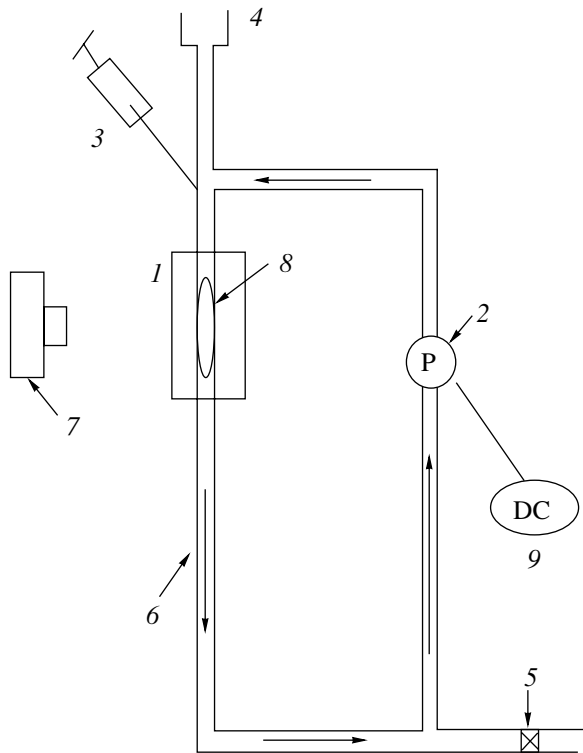*Russian Academy of Sciences, Moscow, Russia*

Fig. 2. Layout of the experimental setup: (*1*) section for measuring and photographing the flow, (*2*) water pump, (*3*) air-feeding syringe, (*4*) tank with water, (*5*) drain valve, (*6*) glass pipe, (*7*) photographic or video camera, (*8*) Taylor bubble, and (*9*) controllable power supply.

Fig. 3. Long Taylor bubble.

a vertical glass pipe with a length of 1.5 m and an inner diameter of 15.6 mm. This pipe was a part of a closed system in which distilled water circulated under the action of an electrical pump. The water flow in the measuring section (glass pipe) was directed downward. Air was introduced into this section through a capillary tube by a calibrated syringe. In this manner, a solitary Taylor bubble was formed in the system and kept at rest by means of the downward water flow, whose velocity was varied with the voltage applied to the pump. The buoyancy force was balanced by other hydrodynamic downstream forces (friction force and inertia force) acting upon the bubble. As a result of the balance of these forces, the Taylor bubble remained at rest. This method enabled us to thoroughly examine the Taylor bubble surface, because the bubble was immobile with respect to the pipe (i.e., to the Eulerian coordinate system). The immobile Taylor bubble was photographed and recorded on videotape using a high-speed video camera.[1]

In order to eliminate the effect of refraction in the cylindrical-pipe wall, a cubic box with glass windows

---

[1] It should be noted that the problem of a moving bubble in an immobile pipe and the problem of a viscous flow around an immobile bubble in the same pipe are not equivalent hydrodynamically.

(with a refractive index $n = 1.41$) was placed in the measuring section. The glass pipe ($n = 1.41$) and the box had a common axis of symmetry. The box was filled with the same distilled water ($n = 1.334$) as in the system. This facility enabled us to investigate the interphase boundaries of the Taylor bubbles without distortions.

In Fig. 3, we show the photograph on which pronounced waves in the form of ripples at the lateral surface of the bubble are seen distinctly. The photographs obtained were processed digitally (Fig. 4). We measured the thickness of the fluid layer between the pipe wall and the Taylor bubble. The experiments showed that the longer the Taylor bubble, the smaller the amplitude and length of the waves at the bubble surface.

The Taylor bubble velocity was also measured. For this purpose, the Taylor bubble was displaced at the glass-pipe bottom by increasing the water-pump capacity. After switching off the pump and stopping the motion of the working fluid, the Taylor bubble began floating up. The measurements were carried out only after the bubble had passed a relaxation section with a
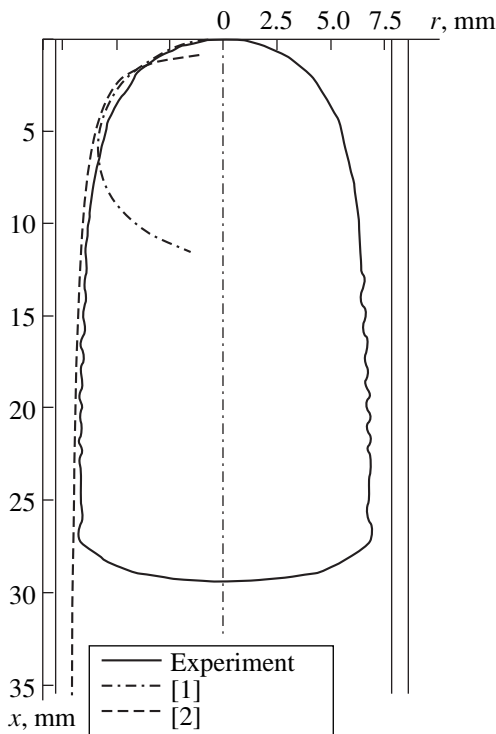
Fig. 4. Taylor bubble shape obtained by the digital processing of the photographic image and the theoretical asymptotes ($D = 15.6$ mm).

The emersion velocity for the Taylor bubble in a cylindrical channel is [1, 2]

$$u_{\mathrm{g}} = k_1 \rho_1^{-\frac{1}{2}} [gD(\rho_1 - \rho_{\mathrm{g}})]^{\frac{1}{2}}, \qquad (4)$$

where ρ_1 and ρ_{g} are the liquid and gas densities, respectively, and k_1 is equal to either 0.351 [1] or 0.328 [2]. We used an average value $k_1 = 0.345$; it was obtained in the set of experiments carried out in study [4]. In our case ($\rho_{\mathrm{g}} \ll \rho_1$), equation (4) can be reduced to the form

$$u_{\mathrm{g}} = 0.345 \sqrt{gD}. \qquad (5)$$

It follows from (5) that the theoretical emersion velocity for the Taylor bubble is equal to 0.135 m/s. This value is very close to 0.13 m/s obtained in our experiment.

From comparison between the Taylor bubble surface and its asymptotic behavior (1)–(3), it is seen that the theoretical values are in good agreement with our experimental data. The results of the comparison are shown in Fig. 4. None of the theoretical schemes known to us can describe waves on the Taylor bubble surface; in any case, this concerns fairly short bubbles.

It is evident that such waves have to be taken into account in calculating the interphase density of the Taylor bubble surface, and this should be the object of further investigations.

length of 15 cm. Measuring the time that the bubble spent to cover a given distance between two points, we determined the emersion velocity. The Taylor bubble velocity was equal to the average velocity of the water flow that held the Taylor bubble in a fixed position. The emersion velocity was 0.13 m/s. The same velocity was observed for all the Taylor bubbles except those with the smallest volume.

The high-speed video recording and photography showed that the stability of the bottom surface of a Taylor bubble depends on its length. Namely, the longer the bubble, the less stable the lower surface.

Translated by V. Bukhanov

REFERENCES

1. D. T. Demitrescu, Z. Angew. Math. Mech. **23**, 139 (1943).
2. R. M. Davies and G. I. Taylor, Proc. R. Soc. London, Ser. A **200**, 375 (1950).
3. S. Jayanti and G. F. Hewitt, Int. J. Multiphase Flow **18**, 847 (1992).
4. D. J. Nusselt, J. O. Wilkes, and J. F. Davidson, Trans. Inst. Chem. Eng. **40**, 61 (1962).
5. E. T. White and R. H. Berdamore, Chem. Eng. Sci. **17**, 128 (1962).

======================== **MECHANICS** ========================

Mathematical Model for Dissociation of Gas Hydrates Coexisting with Gas in Strata

G. G. Tsypkin

Presented by Academician D.M. Klimov June 15, 2001

Received June 20, 2001

1. Fields of natural gas hydrates discovered in various world regions have turned out to be so significant that they are considered as potential sources of natural gas. Presently, the development of technologies for gas extraction from natural deposits of gas hydrates has become a principal problem [1]. In [2, 3], simple models were proposed for hydrate formation and decomposition in natural conditions, which allow for basic governing physical mechanisms. Further investigations demonstrated that the consideration of new physical processes leads to principle changes in the mathematical structure of the solution to the problem of gas-hydrate decomposition in natural reservoirs [4–6].

In this paper, a new mathematical model is analyzed for the dissociation of a heterogeneous gas-hydrate mixture in strata, taking into account the existence of a mobile liquid phase. The presence of four qualitatively different regimes of hydrate decomposition is shown; these correspond to extended hydrate-dissociation domains as well as to ice formation under the dissociation and to the formation of ice plugs in strata initially having positive temperatures.

2. We assume that a hydrate-containing stratum corresponds to a porous medium saturated with a heterogeneous mixture of gas hydrate and gas. We admit that the operation of a gas-producing well decreases the gas pressure in a stratum and leads to hydrate dissociation and the appearance of a domain saturated with water and gas. A system of governing equations comprises the conservation laws for mass and energy, the Darcy law, and the equation of state for the gas, as well as thermodynamic relations. For the gas–hydrate domain, we have the system of equations

$$m\frac{\partial}{\partial t}(1-v)\rho_g + \mathrm{div}\rho_g\vec{v}_g = 0,$$

$$\vec{v}_g = -\frac{k}{\mu_g}f_g(v)\mathrm{grad}P, \tag{1}$$

Institute for Problems in Mechanics,
Russian Academy of Sciences,
pr. Vernadskogo 101, Moscow, 117526 Russia

$$P = \rho_g RT,$$

$$(\rho C)_1\frac{\partial T}{\partial t} + \mathrm{div}(\vec{v}_g P) + C_v\rho_g\vec{v}_g\mathrm{grad}T = \mathrm{div}(\lambda_1\mathrm{grad}T),$$

$$\lambda_1 = mv\lambda_h + m(1-v)\lambda_g + (1-m)\lambda_s,$$

$$(\rho C)_1 = mv\rho_h C_h + m(1-v)\rho_g C_g + (1-m)\rho_s C_s.$$

For the gas–water domain, the system of equations acquires the form

$$m\frac{\partial}{\partial t}(1-S)\rho_g + \mathrm{div}\rho_g\vec{v}_g = 0,$$

$$m\frac{\partial}{\partial t}S + \mathrm{div}\vec{v}_w = 0, \tag{2}$$

$$P = \rho_g RT, \quad \vec{v}_j = -\frac{k}{\mu_j}f_j(S)\mathrm{grad}P, \quad j = w, g,$$

$$(\rho C)_2\frac{\partial T}{\partial t} + \mathrm{div}[P(\vec{v}_g + \vec{v}_w)]$$

$$+ (\rho_w C_w\vec{v}_w + \rho_g C_g\vec{v}_g)\mathrm{grad}T = \mathrm{div}(\lambda_2\mathrm{grad}T),$$

$$\lambda_2 = mS\lambda_w + m(1-S)\lambda_g + (1-m)\lambda_s,$$

$$(\rho C)_2 = mS\rho_w C_w + m(1-S)\rho_g C_g + (1-m)\rho_s C_s.$$

The conditions on the hydrate-decomposition front are formulated like those of the thermodynamically equilibrial jump for saturation functions of gas and water. The conditions of the thermodynamic equilibrium on the hydrate-dissociation front are of the form

$$T_+ = T_- = T_*, \quad P_+ = P_- = P_*,$$

$$\ln P_* = A - \frac{B}{T_*}, \quad A = 49.32, \quad B = 9459. \tag{3}$$

The second group of boundary conditions on the dissociation surface represents the conservation laws

for the mass of gas and water, as well as the energy-conservation law:

$$m\left(v_+\frac{\rho_{0g}}{\rho_g} + S_- - v_+\right)V_n = \frac{kf_g(v_+)}{\mu_g}(\mathrm{grad}\,P)_{n+}$$

$$-\frac{kf_g(S_-)}{\mu_g}(\mathrm{grad}\,P)_{n-},$$

$$m\left(v_+\frac{\rho_{0w}}{\rho_w} - S_-\right)V_n = \frac{kf_w(S_-)}{\mu_w}(\mathrm{grad}\,P)_{n-}, \qquad (4)$$

$$mv_+q\rho_h V_n = (\lambda\,\mathrm{grad}\,T)_{n+} - (\lambda\,\mathrm{grad}\,T)_{n-}.$$

Here, v is the hydrate saturation, T is temperature, P is pressure, S is the water saturation, ν is the filtration rate, f is the relative permeability, m is the porosity, k is the permeability, C is the heat capacity, R is the gas constant, μ is the viscosity, ρ is the density, λ is the thermal conductivity, V is the jump velocity, and q is the specific dissociation heat. The subscripts w, g, and s correspond to water, gas and the skeleton of the porous medium, respectively. The symbols n, plus, and minus correspond to the normal to the hydrate-decomposition front and relevant quantities on the right and left of the front. The symbols asterisk, subscript zero, and superscript zero correspond to values of various quantities on the front, initial values, and values on the immobile boundary, respectively.

3. We now consider the problem of the hydrate decomposition in a semiinfinite stratum. Let, in the initial time moment, the semiinfinite space $x > 0$ occupy a stratum filled with a heterogeneous mixture of hydrate and gas at a temperature T_0, pressure P_0, and the hydrate saturation is $v = v_0$. We assume that on an immobile wall $x = 0$, which corresponds to a gas-extracting well, the pressure drops down to a sufficiently low level P^0. This value satisfies the thermodynamic conditions for the existence of gas in the free state. Then the hydrate-dissociation front $x = X(t)$ propagates to the right from the surface $x = 0$. This front separates the domains saturated with the gas-hydrate mixture and the gas-water mixture.

We analyze the dissociation regimes that correspond to the technology of the hydrate decomposition by the method of decreasing the stratum pressure. In this case, the stratum-temperature variation is not high, since it is associated with the heat absorption due to the hydrate decomposition. Assuming the variations of pressure to be low compared to its absolute value, and ignoring small terms in the systems of equations (1) and (2), we arrive at the system of linear equations for perturbations in the gas–water and hydrate–gas domains, respectively:

$$\frac{\partial S'}{\partial t} = \kappa_w \Delta P', \quad \frac{\partial P'}{\partial t} = \kappa_j \Delta P',$$

$$\frac{\partial T}{\partial t} = a_j \Delta T, \quad j = 1, 2,$$

$$\kappa_w = \frac{kf(S^0)}{m\mu_w}, \quad \kappa_1 = \frac{kP_0}{m\mu_g},$$

$$\kappa_2 = \left[\frac{S^0}{\mu_w} + \frac{1 - S^0}{\mu_g}\right]\frac{kP^0}{m(1 - S^0)}.$$

Here, a_j are the thermal-diffusivity coefficients and S^0 is the unperturbed water saturation for the gas-water domain.

The initial and boundary conditions have the forms

$$t = 0: \; X(0) = 0, \quad x > 0: \; T = T_0, \; P = P_0;$$

$$x = 0: \; P = P^0 \; (P^0 < P_0), \; T = T^0.$$

We now turn to the case when the stratum saturation with hydrate and the initial and boundary values for temperature and pressure are constant. Then the problem has the self-similar solution of the form

$$T = T(\zeta), \quad P = P(\zeta), \quad S = S(\zeta),$$

$$\zeta = x/2\sqrt{a_1 t}, \quad X(t) = 2\gamma\sqrt{a_1 t}.$$

The solutions in both domains can be expressed as probability integrals. Substituting the solutions into the conditions on the moving boundary (3), (4), we obtain a system of transcendental equations for the determination of the boundary velocity and the values of desired functions on this boundary.

4. The system of transcendental equations on the mobile boundary was solved numerically. The numerical experiments performed in the wide range of parameters revealed four principally different regimes for the decomposition of gas hydrates in a stratum that initially coexisted with gas at the positive temperature. Figure 1a exhibits examples of the calculation results, which testify to the existence of a consistent solution corresponding to typical values of parameters and the following initial and boundary conditions:

$$T_0 = T^0 = 275 \text{ K}, \quad P_0 = 6 \times 10^6 \text{ Pa},$$

$$P^0 = 2.5 \times 10^6 \text{ Pa}, \quad k = 10^{-17} \text{ m}^2.$$

In this case, the solution is noncontradictory. The increase in the stratum permeability results in a qualitative change of the solution. Figure 1b presents the calculation results corresponding to $k = 5 \times 10^{-17}$ m² when the hydrate-decomposition temperature in the domain ahead of the dissociation front dropped below the stra-
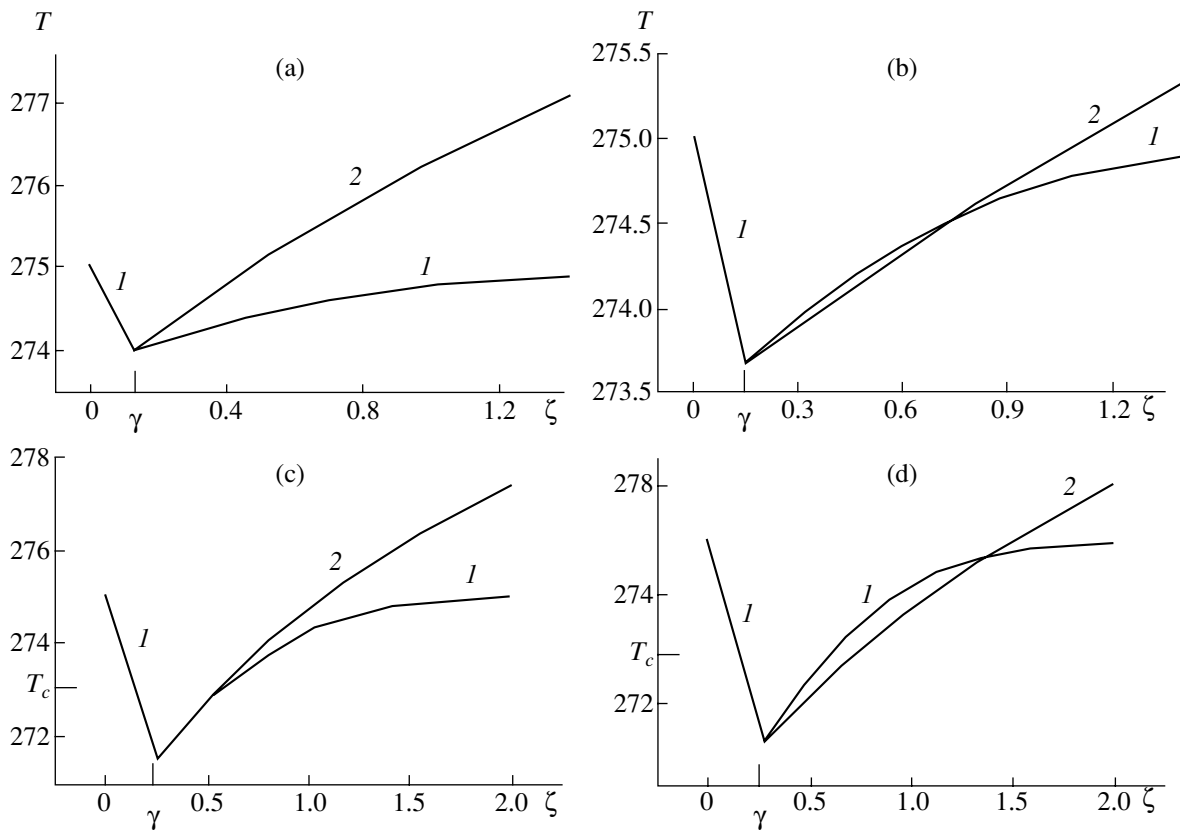
Fig. 1. Distributions (*1*) of temperature T K in a stratum and (*2*) of the hydrate dissociation temperature: (a) noncontradictory case, $P^0 = 2.5 \times 10^6$ Pa, $k = 1 \times 10^{-17}$ m^2; (b) hydrate superheating, $P^0 = 2.5 \times 10^6$ Pa, $k = 5 \times 10^{-17}$ m^2; (c) water supercooling on the dissociation front, $P_0 = 1.3 \times 10^6$ Pa, $k = 1 \times 10^{-17}$ m^2; (d) hydrate superheating in the domain ahead of the dissociation front and supercooling of water on the front, $P_0 = 1.5 \times 10^6$ Pa, $k = 2 \times 10^{-17}$ m^2.

tum temperature, which corresponds to hydrate superheating in the domain. In this case, an extended domain of hydrate decomposition arises similar to the domain introduced in [4].

The decrease in pressure on the boundary ($P^0 = 1.3 \times 10^6$ Pa) for the permeability $k = 1 \times 10^{-17}$ m^2 results in intensifying the dissociation process (Fig. 1c). Therefore, the dissociation temperature calculated in the process of solving the problem turns out to be lower than the water-crystallization temperature. In this case, it is natural to assume that the hydrate-decomposition process is accompanied by the appearance of ice and the formation of ice plugs hindering the gas outflow.

If both the pressure gradient and the permeability are sufficiently high ($P^0 = 1.5 \times 10^6$ Pa, $k = 2 \times 10^{-17}$ m^2), then a dissociation regime can exist for which hydrate in the domain ahead of the dissociation front is superheated and, simultaneously, the temperature calculated on the front is lower than the water-crystallization point (Fig. 1d). In this case, the physical process is accompanied by the creation of an extended dissociation domain and an ice-containing domain.

In the problem-parameter space, domains can be isolated that correspond to the existence of the solution of each type. In Fig. 2, two neutral curves are plotted in the $(k, \Delta P)$-plane. These curves divide the plane into
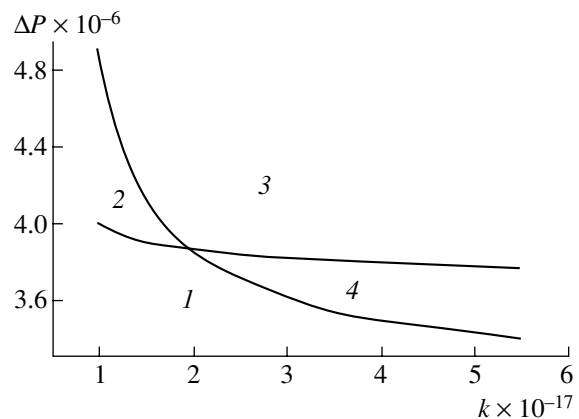

Fig. 2. Critical diagram in the $(k, \Delta P)$-plane. The domains correspond to (*1*) decomposition into gas and water; (*2*) decomposition with the formation of ice; (*3*) formation of ice and of an extended dissociation domain; (*4*) formation of an extended dissociation domain. $\Delta P = P_0 - P^0$.

four domains in which the corresponding form of the solution is realized.

It is worth noting that the model under discussion presents an adequate mathematical description only in one domain in the $(k, \Delta P)$-plane. Nevertheless, this model allows in each case the prediction of both physical features intrinsic to the process and the structure of a mathematical model that presents a consistent description of the process.

ACKNOWLEDGMENTS

REFERENCES

1. E. D. Sloan, *Clathrate Hydrates of Natural Gas* (Marcel Dekker, New York, 1998).
2. N. V. Cherskiĭ and É. A. Bondarev, Dokl. Akad. Nauk SSSR **203**, 550 (1972) [Sov. Phys. Dokl. **17**, 211 (1972)].
3. M. S. Selim and E. D. Sloan, AIChE J. **35**, 1049 (1989).
4. A. M. Maksimov and G. G. Tsypkin, Izv. Akad. Nauk SSSR, Mekh. Zhidk. Gaza, No. 5, 84 (1990).
5. G. G. Tsypkin, Dokl. Akad. Nauk SSSR **323**, 52 (1992) [Sov. Phys. Dokl. **37**, 126 (1992)].
6. G. G. Tsypkin, Izv. Akad. Nauk, Mekh. Zhidk. Gaza, No. 2, 84 (1993).

Translated by G. Merzon

$=====$ **MECHANICS** $=====$

A Physical Cut Introduced into a Preliminary Loaded Elastic Body: The Case of Finite Strains

V. A. Levin

Presented by Academician V.P. Myasnikov January 17, 2001

Received March 13, 2001

The problem under consideration concerns introducing a damage into a preloaded elastic body. The damage leads to the origination of new large strains and stresses. They are superposed upon large strains and stresses already existing in the body considered as a continuum. Since the initial stresses in the body are large, the initial thickness of the cut that finally takes the shape of a narrow slot can be much smaller than the characteristic dimension (length) of the cut. Hence, we can treat the process as a traction breaking along the whole cut, i.e., as the formation of a physical cut (in the sense of a physical microscopic molecular model, for example, within the framework of kinetic theory of fracture [1–3]).

For solving this problem, we use the theory of multiple superposition of large strains [4–6]. Our results from the numerical calculations are given for a plane problem. The extended statement of the problem is the following. Let an unstressed body be subjected to external forces introducing large plane static strains and stresses in the body. As a result, the body makes the transition into the first intermediate state. Further, we mentally remove a part of the body, which is bounded by a certain closed surface. In accordance with the principle of freedom of bonds, we substitute the forces distributed over this surface for the action of the removed part onto the remainder of the body. Obviously, such a procedure does not change the stress–strain state of the remaining body's part. Furthermore, we quasi-statically (for example, isothermally) decrease these forces, considered as external, down to zero. This procedure initiates large stresses and strains (at least, in the vicinity of the boundary surface), which are superposed onto the large initial stresses and strains already existing in the body. As a result, the body makes the transition into the final state (or, if the loading is not completed, into the second intermediate state [5]). Naturally, this transition is accompanied by variation of the shape of the

formed boundary surface (i.e., the cavity contour). In the case under consideration, the surface in the final state is assumed to be given. We note that the procedure of forming another possible cut (if it is required) is similar.

We now write out basic relations of the theory of multiple superposition of large strains [5, 7], which are necessary for solving the problems under consideration.

The system of equilibrium equations and the boundary conditions have the form

$$
\nabla \cdot \overset{n}{\Sigma}_{0,m} - \overset{n}{\Sigma}_{0,m} \cdot \overset{n}{\nabla} \ln(1 + \Delta_{0,m})
$$
$$
+ \overset{n}{\Sigma}_{0,m} \cdot\cdot \overset{n}{\nabla}\Psi_{n,m} \cdot \Psi_{n,m}^{-1} - (\overset{n}{\nabla} \cdot \Psi_{n,m}^{*^{-1}} \cdot \Psi_{n,m}^{*}) \cdot \overset{n}{\Sigma}_{n,m} = 0, \tag{1}
$$

$$
\overset{n}{N} \cdot \overset{n}{\Sigma}_{0,m} = \overset{n(m)}{P}_{\overset{n}{N}},
$$
$$
\overset{nm}{P}_{\overset{}{N}} = (1 + \Delta_{0,n}) \frac{\left| d\overset{n}{\tau}_k \right|}{\left| d\overset{m}{\tau}_k \right|} \overset{n(n)}{P}_{\overset{n}{N}} \cdot \Psi_{m,n}^{-1}. \tag{2}
$$

In Eq. (1),

$$
\overset{n}{\Sigma}_{0,m} = (1 + \Delta_{0,n})\Psi_{m,n}^{*} \cdot \sigma_{0,m} \cdot \Psi_{m,n} \tag{3}
$$

is the generalized total-stress tensor in the mth state, with the tensor related to the coordinate basis of the nth state; $\sigma_{0,m}$ is the actual total-stress tensor in the mth state (at $m = 1$, $\sigma_{0,1}$ is the Cauchy tensor); $\Delta_{0,m}$ is the relative volume change caused by transition of the body from the initial state to the mth state; $\Psi_{m,n} = \Psi_{0,m}^{-1} \cdot \Psi_{0,n}$ is the corresponding strain affinor [5, 7]; $\Psi_{m,n} = \overset{m}{\mathbf{e}}_i \overset{n}{\mathbf{e}}_i$; $\overset{n}{\mathbf{e}}_i = \dfrac{\partial \overset{n}{\mathbf{r}}}{\partial \xi^i}$; $\overset{n}{\mathbf{r}}$ is the radius vector of the particle in the nth state; ξ^i are the Lagrangian (frozen [8]) coordinates of the particle; $\overset{n}{\mathbf{r}} - \overset{n}{\mathbf{r}}^1 = \mathbf{u}_n$, where $\mathbf{u}_n$ is the vector deter-

---

Moscow State University, Vorob'evy gory,
Moscow, 119899 Russia

mining the translation from the previous $((n-1)$th) state to the next (nth) one; and

$$\Psi_{q,p} = I + \sum_{n=q+1}^{p} \overset{p}{\nabla}\mathbf{u}_n = \left(I - \sum_{n=q+1}^{p} \overset{p}{\nabla}\mathbf{u}_n\right)^{-1},$$

$$\overset{p}{\nabla} = \overset{p_i}{\mathbf{e}}\frac{\partial}{\partial\xi^i}.$$

(4)

In Eqs. (1)–(4) and below, the symbol above a quantity denotes the number of the state which this quantity is given in or to which it is related (with the exception of $\overset{n}{\mathbf{r}}$ and $\overset{n}{\mathbf{e}}$).

In Eqs. (2), $\overset{n\,(n)}{P_{\overset{}{N}}}$ is the vector of actual stresses on the $d\overset{n}{\tau}_k = \overset{n}{N}|d\overset{n}{\tau}_k|$ area. The symbol $*$ stands for the transposition. For the Treloar material, which was used in the specific calculations, the defining relations written in the space of an arbitrary mth state have the form ([5, 7, 9])

$$\overset{m}{\Sigma}_{0,n} = p_{0,n}(I + 2\alpha\overset{m}{E}_{m,n})^{-1} + \mu(I - 2\overset{m}{E}_{0,m})^{-1},$$

$$\alpha = \mathrm{sgn}(m-n).$$

(5)

Here, $\overset{m}{E}_{m,n}$ is the strain tensor describing strain variation caused by the transition from the mth state to the nth state and related to the coordinate basis of the nth state. (We note that, for $m > n$, the sequence of subscripts in the notation $\overset{m}{E}_{m,n}$ entering into the first term is inverted; i.e., formally, $\overset{m}{E}_{m,n} = -\overset{m}{E}_{n,m}$.) In the general case,

$$\overset{\gamma}{E}_{q,p} = \frac{1}{2}(\Psi_{\gamma,p}\cdot\Psi_{\gamma,p}^* - \Psi_{\gamma,q}\cdot\Psi_{\gamma,q}^*),$$

$$\Psi_{\gamma,p} = \Psi_{p,\gamma}^{-1},$$

(6)

where, for $p = \gamma = 1$ and $q = 0$, $\overset{1}{E}_{0,1}$ is the Almansi tensor. In Eqs. (5), $p_{0,n}$ is the Lagrange multiplier. It is determined by both the equations of the boundary value problem and the incompressibility conditions [5, 9]

$$\Delta_{0,n} \equiv 0,$$

representing, in the general case, a system of N equations, where N is the number of the final state [9].

Relations (4)–(6) show that for $m > n$, the tensor $\overset{m}{E}_{0,n}$ depends not only on the strain tensor $\overset{m}{E}_{0,n}$ but also on the strain tensor $\overset{m}{E}_{n,m}$. As a result, solving the problems formulated in the space of the mth state is signifi-

cantly complicated, because the system of the equilibrium equations (in general, m vector equations) does not split into separate equations. However, such a formulation is often necessary, for example, when boundary conditions are specified in the mth state.

We now consider the results of solving the problem formulated above on a cut introduced into a preliminary loaded body made of the Treloar material [5, 9], with the final shape of the damage being a narrow slot with the axes a and b. In the case of a preliminary uniaxial tensile load, when $\sigma_{0,1_{1,1}}^{\infty} = 0$ and $\sigma_{0,1_{2,2}}^{\infty} = 0.0060415\mu$, provided that $\frac{a}{b} = 248$ (with the coefficients of conformal transformation $C_1 = 0.988$ and $C_3 = -0.004$), we have $h = 0.21 \times 10^{-5}l$. Here, h and l are the maximum distance between the edges of a damage (crack) and its length (the characteristic dimension of the damage), respectively, at the initial time. In addition, $\sigma_{0,2_{\varphi\varphi}} = 1.28\mu$ in the crack tip. We note, for example, that when $l = 0.3$ mm, the dimension h can be considered as a permolecular one [10, 11].

Thus, the above consideration confirms the statement made at the beginning of the paper.

ACKNOWLEDGMENTS

REFERENCES

1. G. Pluvinagge, *Mecanique elastoplastique de la rupture* (Toulouse, 1989; Mir, Moscow, 1993).

2. G. P. Cherepanov, *Mechanics of Brittle Failure* (Nauka, Moscow, 1974).

3. E. M. Morozov and M. V. Zernin, *Contact Problems in Failure Mechanics* (Mashinostroenie, Moscow, 1999).

4. V. A. Levin, Dokl. Akad. Nauk SSSR **299**, 1079 (1988) [Sov. Phys. Dokl. **33**, 296 (1988)].

5. V. A. Levin, *Multiple Severe Deformation of Elastic and Viscoelastic Bodies* (Nauka, Moscow, 1999).

6. V. A. Levin, Int. J. Solids Struct. **35**, 2585 (1998).

7. V. A. Levin and K.V. Zingerman, Trans. ASME, J. Appl. Mech. **65**, 431 (1998).

8. L. I. Sedov, *An Introduction to the Mechanics of Continuum* (Fizmatlit, Moscow, 1962).

9. A. I. Lur'e, *Nonlinear Theory of Elasticity* (Nauka, Moscow, 1980).

10. V. V. Novozhilov, Prikl. Mat. Mekh. **33**, 212 (1969).

11. V. V. Novozhilov, Prikl. Mat. Mekh. **33**, 797 (1969).

Translated by Yu. Verevochkin

======================== **MECHANICS** ========================

Initiation of the *T* Sheet
in a Disk-Shaped Magnetohydrodynamic Channel

Corresponding Member of the RAS V. M. Fomin, V. P. Fomichev, and A. Yu. Kerkis

At the present time, a growing interest is observed in the magnetohydrodynamic (MHD) method for the direct transformation of thermal energy into electric energy. This method is considered to be the most promising for creating various autonomous power facilities that can be employed, e.g., in geophysical studies [1, 2], in the development of compact autonomous power modules [3–6], in aerospace applications [7–9], etc. The general feature of these and similar facilities is the fact that in order to run them, hot gas flows produced by combusting various solid, liquid, and gaseous fuels at a temperature from 2000 to 3000 K are used.

A complication in the employment of these flows is that it implies a certain level of electric conduction required for the MHD process in conditions when the thermal ionization of fuel-combustion products is virtually absent. The conduction can be provided, e.g., by using readily ionized additives of alkaline metals [10]. However, due to the great ecological hazard, this method is completely unsuitable in the case of application of the MHD method in autonomous power modules and aerospace crafts that operate by an open cycle. The solution to this problem can be found through the employment of laminar flows with a nonuniform electric conduction.

A principle feasibility to form a stable flow-layer structure is associated with using the *T*-sheet effect theoretically predicted and substantiated by Academicians Tikhonov and Samarskiĭ with their coworkers [11]. This feasibility implies that a domain with a high temperature, equilibrium conduction (the so-called *T* layer or *T* sheet), and high electric-current density is formed in a flow of weakly conducting gas (plasma) moving across a magnetic field. The *T* layer can be formed in a plasma flow due to small fluctuations of the electric conduction as a result of a nonlinear effect consisting of the development of superheating instability [12]. In order to use the effect of the *T* layer in facilities with a relatively cold flow, it is necessary to be able to initiate it. This can be realized, e.g., with the help of additional

heating of a part of the flow up to a temperature supporting a certain minimal conduction level sufficient for the development of the *T* sheet.

It was shown theoretically that the *T* sheet in the flow of a weakly conducting plasma can be obtained by introducing a local perturbation of either temperature or electric conduction [13]. If the temperature perturbation gives rise to the *T* sheet, we speak on the pickup of the perturbation. If this perturbation of the flow temperature occurs during a time much shorter than the time of the sound-wave propagation through the channel width, then we should speak about the isochoric heating process. The calculations made in [14] showed that, at the initial time moment, the process of the expansion (divergence) of the perturbed wave essentially affects the pickup of the isochoric perturbation. This fact sometimes results in ceasing the *T*-sheet development. Such a phenomenon cannot be observed upon the spontaneous appearance of the *T* sheet in a plasma flow placed into a magnetic field, because the development of the *T* sheet occurs from an infinitely small perturbation (fluctuation) of the conduction. It is of interest to experimentally investigate the effect of the perturbance pickup.

The initiation of the *T* sheet by local isochoric heating was experimentally investigated on the basis of a model of a disk-shaped induction MHD generator. The sketch of the experimental setup is presented in Fig. 1. An electric-discharge shock tube with a coaxial discharge chamber served as a plasma source. The diameters of both the chamber and the low-pressure channel were 50 mm. The discharge chamber and the channel were made of copper and aluminum, respectively. The lengths of the chamber and of the channel were 850 and 1200 mm. The plasma source was fed from a capacitor battery with a total capacity of 1200 μF and a voltage of 5 kV.

The channel *2* is connected with a ring-shaped MHD channel formed by two organic-glass disks with a diameter of 350 mm. The gap between the disks (i.e., the MHD-channel width) is 20 mm. In channel walls, sockets for pressure sensors and Rogowski loops are provided. There are also optical windows for IR diagnostics, spectroscopic measurements, and photorecording plasma flows. The MHD channel was designed

Institute of Theoretical and Applied Mechanics,
Siberian Division, Russian Academy of Sciences,
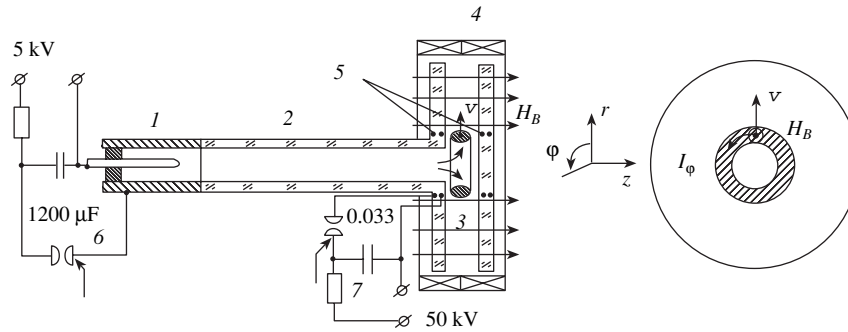*Novosibirsk, Russia*

Fig. 1. Sketch of the experimental setup aimed at investigation of the *T*-sheet development after a local temperature perturbance: (*1*) coaxial plasma source; (*2*) low-pressure channel; (*3*) disk-shaped MHD channel; (*4*) permanent-current electromagnet; (*5*) induction-heating coil; (*6*) power-supply units for the plasma generator; (*7*) oscillator-heater.

according to data obtained as a result of studies of the *T*-sheet development, which were described in [11, 15].

The external magnetic field is formed by an iron-free permanent-current electromagnet constructed in accordance with the Helmholtz scheme. The maximum field strength in the electromagnet gap reached 6400 Oe; the radial and axial nonuniformities of the field were lower than 2% in both the central and the middle channel parts and 5% at the channel end.

At the channel inlet, plasma was heated by a pulsed inductive discharge. Inductor turns with a radius of 55 mm were located in pairs at each side. They were embedded into the channel walls at a depth of 1 mm. A capacitor battery with a total capacity of 0.033 μF and a voltage of 50 kV is discharged into two induction coils switched contrary to each other.

Flow parameters, namely, the flow velocity, the gas-dynamic pressure, and the electron density, which are required for the determination of the hydromagnetic interaction, were measured. According to the two latter quantities, the electron temperature and the electric conduction were calculated, which are necessary for the determination of the magnetic Reynolds number and the hydromagnetic-interaction parameter. The flow velocity was determined by photographic sweeps of the plasma flow. The pressure and the electron density were determined with the help of piezoelectric sensors and by both the broadening of the hydrogen H_β emission line and the absorption of laser radiation with wavelength $\lambda = 10.6$ μm.

We performed an experimental verification of the possibility for the existence of the pickup and an investigation of its basic characteristics. The results obtained were compared with the spontaneously arising *T* sheet described in [11, 13, 15]. To do this, the setup regimes were initially studied in which a flow with the *T* sheet appeared as a result of the development of a superheating instability in the flow. These instabilities were associated with nonuniformities of the temperature and conductivity existing in the flow. Figure 2 presents plots for the variation of both the maximum electron density in the *T* sheet and its velocity as a function of the chan-

nel radius at $H_0 = 3200$ Oe. As is seen, the electron density increases during the motion along the channel from 2.2×10^{16} at its inlet to 4.0×10^{16} cm^{-3} at the radius of 85 mm. At the time moment corresponding to the radius of 130 mm, the drag ceases and, in the process of further movement, the flow velocity remains constant, while the electron density decreases to 2×10^{16} cm^{-3}. The temperature distribution along the channel length, which was calculated from the measured values of N_e and p, testifies to the fact that in the input part of the channel the plasma in the bright luminous ring (the *T* sheet being photographed manifests itself in this manner) is heated, and its temperature reaches 13 000 K. Furthermore, at the channel end (for *r* exceeding 100 mm) the temperature drops to 10 000 K. Such features of the process are consistent with the experimental results obtained for air in the case of the spontaneous formation of the *T* sheet [15]. Thus we can consider dynamics of the current-sheet development and the associated flow rearrangement, in general, to be similar to those described in [13] and observed in [15]. These facts tes-
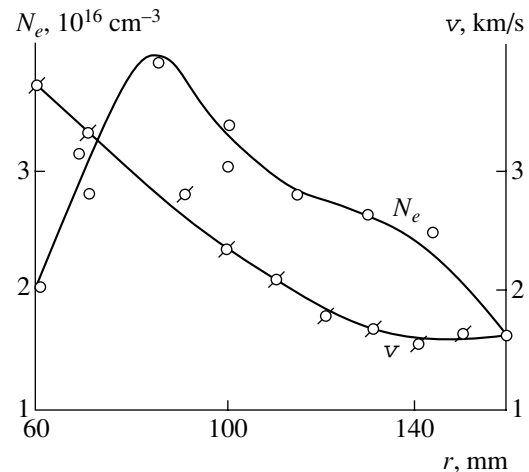

Fig. 2. Electron-density variation in the current sheet and velocities of its motion along the MHD channel as a function of the channel radius. $H_0 = 3200$ Oe, argon, $p_0 = 2$ torr.
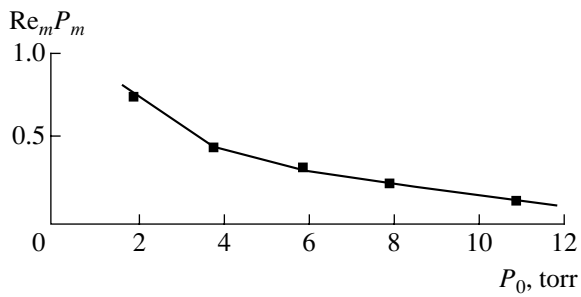
Fig. 3. Variation of the hydromagnetic-interaction parameter P at the input of the MHD channel as a function of the initial pressure.
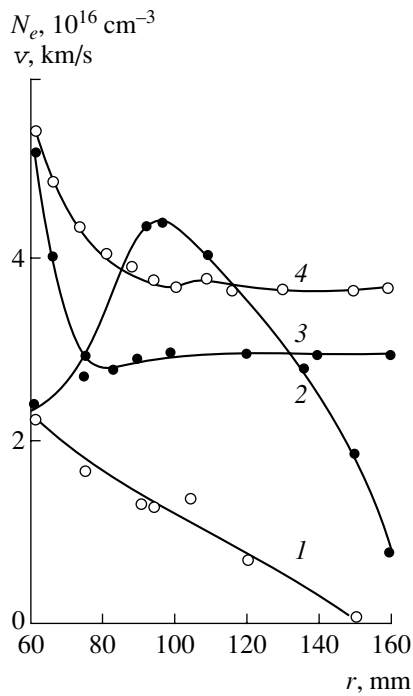

Fig. 4. Variations of flow parameters in the ring-shaped heating zone during flow movement in the channel: (*1*), (*2*) electron density; (*3*), (*4*) flow velocity. (○) $H_0 =$ 1600 Oe; (●) 4800 Oe.

tify to the manifestation of the *T*-sheet effects. The magnetic Reynolds number was 0.3–0.4. In this case, the parameter of the hydrodynamic interaction, $P = \mathrm{Re}_m P_m$, was 0.5–0.6.

Afterwards, by increasing the initial pressure in the plasma source, the decrease in temperature and the plasma-flow velocity at the input of the MHD channel was attained. In this case, weakening or a complete cessation of the plasma interaction with the external magnetic field in the channel was observed. Figure 3 exhibits the parameter of the hydromagnetic interaction as a function of the initial pressure (from 1 to 12 torr) in the plasma source.

As the experiments showed, when the initial pressure was higher than 10 torr, the flow parameters were so small that the interaction of the flow with the magnetic field was not observed. In these conditions, the initiation of the *T* sheet was investigated with the help of additional heating of the flow.

The heating of plasma in a ring with an approximate cross section of $2 \times 2 \ \mathrm{cm}^2$ was provided by the induction discharge for 2 μs. During this time, an energy of about 4 J was introduced into the plasma. Comparing the time of heating (2 μs) with the time of the sound-wave propagation through the perturbed zone having a temperature of 12000 K, a pressure of 0.6 bar, and a width of 2 cm ($t_S \approx 10$ μs), we can consider the heating to be isochoric. The moment for heating was chosen so as to provide the increase of the electron density immediately beyond the front of the wave produced after the impact of the plasma bunch with the end wall. The experimental results obtained for the pressure $p_0 = 2$ torr testifies to the fact that the current sheet indeed arises in this part of the flow. The plots for variations of the maximum electron density of the flow in the bright luminous zone (i.e., in the *T* sheet) with the channel radius, as well as the flow velocity at the magnetic-field intensity $H_0 = 1600$ and 4800 Oe, are given in Fig. 4. As is seen, heating the flow at a magnetic-field intensity of 1600 Oe leads to neither an increase in the electron density during the movement of the flow along the channel nor the formation of the current sheet. The formation of the current sheet occurs with an increase of the magnetic-field intensity to 4800 Oe. The electron density in the heated layer rose with the radius, and an essential flow drag was observed. As a result of heating, the electron concentration, pressure, and temperature in the narrow ring-shaped zone increased from $0.4 \times 10^{16} \ \mathrm{cm}^{-3}$, 0.7 bar, and 8500 K to $2.5 \times 10^{16} \ \mathrm{cm}^{-3}$, 0.8 bar, and 10600 K, respectively. In this case, the magnetic Reynolds number and the parameter of hydromagnetic interaction increased to 0.22 and 0.34. As a result, conditions arose in favor of sufficiently intense flow interaction with the magnetic field.

In conclusion, we analyze the data presented in Figs. 2 and 4, as well as features of the flow with allowance for the fact that the magnetic Reynolds number and hydromagnetic-interaction parameter have comparable values. Under these conditions, we can certainly identify the argon-plasma flows for $p_0 = 11$ torr in the presence of heating (which were accompanied by the initiation of the *T* sheet) with the flow at $p_0 = 2$ torr without heating when the spontaneous *T*-layer formation was observed.

Thus, based on the results presented above, we may conclude that the *T* sheet can be initiated in the MHD channel by isochoric heating of a part of a flow.

REFERENCES

1. E. P. Velikhov, B. P. Zhukov, A. E. Sheĭndlin, *et al.*, in *Proceedings of the 8th International Conference on*

MHD-Energy Transformation, Moscow, 1983, Vol. 5, p. 59.

2. E. P. Velikhov, O. G. Matveenko, V. P. Panchenko, *et al.*, Dokl. Akad. Nauk **370**, 617 (2000) [Dokl. Phys. **45**, 74 (2000)].

3. J. P. Moder, L. N. Myrabo, and D. A. Kaminski, J. Propul. Power **9**, 739 (1993).

4. M. Ishikawa, T. Suemura, M. Fujita, and J. Umoto, J. Propul. Power **9**, 749 (1993).

5. N. Esposito, M. Raugi, and A. Tellini, IEEE Trans. Magn. **31**, 47 (1995).

6. Y. P. Babakov, A. V. Plekhanov, and V. B. Zheleznyi, IEEE Trans. Magn. **31**, 259 (1995).

7. V. S. Slavin and K. A. Finnikov, in *Proceedings of the 3rd Conference on Magnetic and Plasma Aerodynamics in Aerospace Applications (Notes to Reports), Moscow, 2001*, p. 64.

8. A. L. Kuranov and E. G. Sheikin, in *Proceedings of the II Workshop on Magneto-Plasma-Aerodynamics in Aerospace Applications, Moscow, 2000*, p. 69.

9. S. O. Macheret, M. N. Shneider, and R. B. Miles, in *Proceedings of the II Workshop on Magneto-Plasma-Aero-dynamics in Aerospace Applications, Moscow, 2000*, p. 86.

10. V. A. Kirilin and A. E. Sheĭndlin, Teplofiz. Vys. Temp. **12**, 372 (1974).

11. A. N. Tikhonov, A. A. Samarskiĭ, L. A. Zaklyaz'minskiĭ, *et al.*, Dokl. Akad. Nauk SSSR **173**, 808 (1967) [Sov. Phys. Dokl. **12**, 331 (1967)].

12. V. S. Sokolov, Phenomena of the *T* Sheet and of the Superheating Instability in Certain Problems of Magnetic Gas Dynamics. Doctoral Dissertation in Physics and Mathematics (Novosibirsk, 1974).

13. L. N. Degtyarev, L. A. Zaklyaz'minskiĭ, S. P. Kurdyumov, *et al.*, Teplofiz. Vys. Temp. **7**, 471 (1969).

14. N. N. Yanenko, S. S. Katsnel'son, A. Yu. Kerkis, *et al.*, Chislennye Metody Mekh. Sploshnoĭ Sredy **9**, 146 (1978).

15. A. Yu. Kerkis, V. S. Sokolov, N. A. Trynkina, and V. P. Fomichev, Prikl. Mekh. Tekh. Fiz., No. 3, 31 (1974).

Translated by G. Merzon

===== **MECHANICS** =====

Averaging Method in Systems with Fast and Slow Phases

L. D. Akulenko

Presented by Academician F.L. Chernous'ko August 16, 2001

Received August 16, 2001

Nonlinear oscillatory systems containing fast and slow phases are considered. We propose a modified averaging method under conditions when slow variables averaged over the fast phase do not vary. We describe and substantiate a new method for separation of variables. The method is applicable for large time intervals at which significant changes of all the variables take place. Several examples illustrating the approach proposed are presented.

1. We consider a system of two vectors x and y with arbitrary dimensions, which is standard in the Bogolyubov sense [1, 2]. We assume that the following requirements concerning the quantities averaged with respect to t are satisfied:

$$\dot{x} = \varepsilon X(t, x, y), \quad x(0) = x^0, \quad X_0(x, y) = \langle X \rangle \equiv 0;$$
$$\dot{y} = \varepsilon Y(t, x, y), \quad y(0) = y^0, \quad Y_0(x, y) = \langle Y \rangle \not\equiv 0; \tag{1}$$

The functions X and Y are assumed to be piecewise-continuous, 2π-periodic in t, and sufficiently smooth in $(x, y) \in D_x \times D_y$, where D_x and D_y are closed bounded sets. The angular brackets stand for averaging over the argument t (i.e., over the fast phase). In the first approximation with respect to ε, the mean variation rate of x is zero; i.e., $|x - x^0| = O(\varepsilon)$, and that of y is on the order of $O(\varepsilon)$; i.e., $|y - y^0| = O(1)$ for $t \sim \frac{1}{\varepsilon}$. For practical applications, it is of interest to study the variation of the slow variable x within a time interval $t \sim \frac{1}{\varepsilon^2}$, because this variable determines basic parameters of the oscillatory system (its energy and amplitude). The fast variable y is usually related to a phase or an angular variable and can significantly affect the vector x (see examples in Section 4).

Institute of Problems in Mechanics,
Russian Academy of Sciences,
pr. Vernadskogo 101, Moscow, 117526 Russia

In the general case of a system of form (1), the application and substantiation of the standard averaging method at a time interval of $t \sim \frac{1}{\varepsilon^2}$ (1) is difficult. Therefore, we will consider the case, often encountered in applications, when the average system for y has a complete family of one-particle rotatory–oscillatory motions with a constant $x = \xi$ [1–3]:

$$x = \xi \in D_x, \quad y = \eta_0(\varphi, \zeta, \xi) \in D_y,$$
$$\varphi = \omega(\zeta, \xi)\tau + \varphi^0, \quad \tau = \varepsilon t. \tag{2}$$

Here, φ is the slow phase ($\dot{\varphi} \sim \varepsilon$) and the summed dimension of the constant vectors ζ and $\varphi^0 (\mathrm{mod}\, 2\pi)$ coincides with the dimension of y.

Using the change of variables $(x, y) \longrightarrow (\xi, \eta)$, which is close to an identity, we rewrite system (1) in the form

$$\dot{\xi} = \varepsilon^2 \Xi(t, \xi, \eta, \varepsilon), \quad \xi(0) = x^0, \quad \xi \in D_x;$$
$$\dot{\eta} = \varepsilon Y_0(\xi, \eta) + \varepsilon^2 H(t, \xi, \eta, \varepsilon),$$
$$\eta(0) = y^0, \quad \eta \in D_y; \tag{3}$$
$$x = \xi + \varepsilon \int_0^t X(s, \xi, \eta)\, ds,$$
$$y = \eta + \varepsilon \int_0^t [Y(s, \xi, \eta) - Y_0(\xi, \eta)]\, ds.$$

The functions Ξ and H satisfy the conditions of smoothness and periodicity. Ignoring the terms on the order of $O(\varepsilon^2)$ in system (3), we arrive at expressions (2) for ξ and η. We then make the change of variables $y = \eta \longrightarrow (\zeta, \varphi)$ according to relations (2). As a result, with due regard to the terms on the order of $O(\varepsilon^2)$ and the identity for η_0, we obtain a system with both fast and slow phases, t and φ, respectively:

$$\dot{\alpha} = \varepsilon^2 A(t, \alpha, \varphi, \varepsilon), \quad \alpha(0) = \alpha^0, \quad \alpha = (\xi^T, \zeta^T)^T,$$

$$\dot{\varphi} = \varepsilon\omega(\alpha) + \varepsilon^2\Phi(t, \alpha, \varphi, \varepsilon),$$

$$\varphi(0) = \varphi^0(\mathrm{mod}\,2\pi); \quad A = (\Xi^T, Z^T)^T,$$

$$(\Phi, Z^T)^T = \left\|\frac{\partial\eta_0}{\partial\varphi}, \frac{\partial\eta_0}{\partial\zeta}\right\|^{-1}\left(H - \frac{\partial\eta_0}{\partial\xi}\Xi\right); \quad (4)$$

$$\left(\frac{\partial\eta_0}{\partial\varphi}\right)\omega(\xi, \zeta) \equiv Y_0(\xi, \eta_0), \quad \alpha \in D_\alpha, \quad |\varphi| < \infty.$$

The functions A, ω, and Φ are sufficiently smooth in α, φ, and ε; in addition, they are piecewise-continuous in t and 2π-periodic in t and φ. The initial values α^0 and φ^0 are determined by the change of variables $y \longrightarrow (\zeta, \varphi)$ according to relations (2). System (4) is to be analyzed in the interval $0 \le t \le \dfrac{L}{\varepsilon^2}$ on which the slow variable α can acquire, generally speaking, an increment of $\delta\alpha \sim 1$. In this case, the fast phase, i.e., the argument t, is separated out with an accuracy to a desired power of ε, while the slow phase φ and variable α are interrelated. The averaged system allows a new argument $\tau = \varepsilon t$, $0 \le \tau \le \dfrac{L}{\varepsilon}$, to be introduced and, furthermore, can be subjected to the standard asymptotic analysis [1–6]. If the phase φ is scalar, the averaging method developed for systems with fast rotating phases is employed [1, 2]. Like the classical Krylov–Bogolyubov method, the proposed scheme of highest powers is based on the requirement that the asymptotic expansion should contain no singular terms of the form $(\varepsilon^2 t)^k$ within the extended interval $0 \le t \le \dfrac{L}{\varepsilon^2}$. A particular case of missing y was studied previously [7].

2. In order to separate the fast phase t, we use the change of variables $(\alpha, \varphi) \longrightarrow (\beta, \psi)$ such that the variable t is eliminated from the equations with an accuracy to a desired power of ε:

$$\alpha = \beta + \varepsilon^2\Pi(t, \beta, \psi, \varepsilon), \quad \varphi = \psi + \varepsilon^2\Gamma(t, \beta, \psi, \varepsilon),$$

$$\dot{\beta} = \varepsilon^2 B(\beta, \psi, \varepsilon), \quad \dot{\psi} = \varepsilon\omega(\beta) + \varepsilon^2\Psi(\beta, \psi, \varepsilon). \quad (5)$$

In the right-hand sides of Eqs. (5), the unknown exchange functions Π and Γ, which are 2π-periodic with respect to t and ψ and do not contain the functions B and Ψ averaged over t and independent of t, can be approximately found by asymptotic expansions of them or by successive approximations in powers of ε using the solutions to the following partial differential equations:

$$(I + \varepsilon^2\Pi'_\beta)B + \Pi'_\psi(\varepsilon\omega + \varepsilon^2\Psi)$$

$$= A(t, \beta + \varepsilon^2\Pi, \psi + \varepsilon^2\Gamma, \varepsilon) - \Pi'_t,$$

$$\varepsilon^3\Gamma'_\beta B + (1 + \varepsilon^2\Gamma'_\psi)(\omega(\beta) + \varepsilon\psi) \quad (6)$$

$$= \omega(\beta + \varepsilon^2\Pi) + \varepsilon\Phi(t, \beta + \varepsilon^2\Pi, \psi + \varepsilon^2\Gamma, \varepsilon) - \Gamma'_t.$$

In particular, the first expansion coefficients governing a significant evolution of the variables are given by the equations

$$B_0 = \langle A(t, \beta, \psi, 0)\rangle,$$

$$\Pi_0(t, \beta, \psi) = \int_0^t ((A) - \langle(A)\rangle)ds,$$

$$\psi_0 = \langle\Phi(t, \beta, \psi, 0)\rangle, \quad (7)$$

$$\Gamma_0(t, \beta, \psi) = \int_0^t ((\Phi) - \langle(\Phi)\rangle)ds;$$

$$B_1 = \langle(A'_\varepsilon)\rangle - \omega(\beta)\langle\Pi'_{0\varphi}\rangle, \dots.$$

The angular brackets stand for averaging over the explicit argument t, and the quantities in the parentheses (A) or (Φ) correspond to $\alpha = \beta$, $\varphi = \psi$, and $\varepsilon = 0$. The subsequent coefficients B_j, Π_{j-1}, Ψ_{j-1}, and Γ_{j-1}, with $j \ge 2$, are found by the recurrence method. By analogy with the conventional averaging, in order to construct the jth approximation within a time interval of $t \sim \varepsilon^{-2}$, all the functions up to B_{j-1}, Π_{j-2}, Ψ_{j-2}, and Γ_{j-3} must be found. In particular, the Cauchy problem for the first approximation takes the form

$$\dot{\beta} = \varepsilon^2 A_0(\beta, \psi), \quad \beta(0) = \alpha^0; \quad \dot{\psi} = \varepsilon\omega(\beta),$$

$$\psi(0) = \varphi^0; \quad 0 \le t \le L\varepsilon^{-2}. \quad (8)$$

System (8) can be treated by standard analytic or numerical methods. This system is significantly simpler than original system (4), allows the slow time $\tau = \varepsilon t$ to be introduced, and can be written out in a standard form with the fast phase ψ [1–5]. If the function $\omega(\beta) \ge c > 0$, where c is a constant, then the phase ψ is rotating and, in the first approximation, the method of averaging over the variable ψ in the interval $0 \le \tau \le \dfrac{L}{\varepsilon}$ is applicable to the system (8); i.e., $t \sim \varepsilon^{-2}$.

The following theorem holds.

Theorem 1. *The solution to Cauchy problem* (8) *determines the solution to problem* (5) *under the same initial conditions with errors on the order of* $O(\varepsilon)$ *in* β *and of* $O(1)$ *in* ψ *within the time interval* $0 \le t \le L\varepsilon^{-2}$. *The slow* ($\alpha$, ξ, *and* x) *and relatively fast* (η, φ, *and* y) *variables are found within this interval with errors on the order* of $O(\varepsilon)$ *and of* $O(1)$, *respectively. In general, the variations in the quantities* x, y, ξ, η, α, *and* β *are*

on the order of $O(1)$ and those in φ and ψ are on the order of $O(\varepsilon^{-1})$; i.e., a significant evolution of the system occurs.

Proof. Under corresponding assumptions on smoothness and boundedness, Theorem 1 is proved with the help of the Gronwall lemma by standard methods with due regard to the exact changes of variables (3) and (5).

The second approximation is based on the averaged Cauchy problem

$$\dot{\beta} = \varepsilon B_0(\beta, \psi) + \varepsilon^2 B_1(\beta, \psi),$$
$$\dot{\psi} = \omega(\beta) + \varepsilon \Psi_0(\beta, \psi) \tag{9}$$

under the same initial conditions. The dot (in the superscript) stands for the derivative with respect to $\tau = \varepsilon t$, $0 \le \tau \le L\varepsilon^{-1}$. The functions B_j and Ψ_{j-1} are determined from Eqs. (5)–(7). The problem of nth approximation is constructed similarly to (8) and (9):

$$\dot{\beta} = \varepsilon B_0(\beta, \psi) + \varepsilon^2 B_1 + \ldots + \varepsilon^j B_{j-1}, \quad \beta(0) = \alpha^0,$$
$$\dot{\psi} = \omega(\beta) + \varepsilon \Psi_0(\beta, \psi) + \varepsilon^2 \Psi_1 + \ldots + \varepsilon^{j-1} \Psi_{j-2}, \tag{10}$$
$$\psi(0) = \varphi^0.$$

Here, the terms on the order of ε^{j+1} and of ε^j are omitted in β and ψ, respectively. When constructing the jth approximation, we can also use a standard scheme of successive approximations, which is based on partial differential equations (6) in the functions B, Ψ, Π, and Γ having a certain structure. Both the schemes require that the right-hand side of system (4) should be smooth in α and φ [i.e., original system (1) should be smooth in x and y], because the order of the derivatives with respect to the slow variables β and ψ increases. In the general case, the separation of the variables t, β, and ψ does not occur even for analytic systems [4, 5].

The following theorem holds.

Theorem 2. *The functions $\beta(\tau, \varepsilon)$ and $\psi(\tau, \varepsilon)$ determined by Eqs. (10) are the solution to Cauchy problem (4) with errors on the order of $O(\varepsilon^j)$ and of $O(\varepsilon^{j-1})$ at the interval $0 \le \tau \le L\varepsilon^{-1}$, respectively. The original variables x and y are found with the same errors.*

In the particular case of a quasi-linear oscillatory system with $\omega(\beta) = \nu = \text{const}$, all the variables are determined with the same error of $O(\varepsilon^j)$ [1, 2]. Theorems 1 and 2 substantiate the application of the second-power scheme ($t \sim \varepsilon^{-2}$).

3. The proposed scheme for the separation of variables can be extended to the case of the slow phase φ determined by Eqs. (2) and (3). As a result, we arrive at an approximate many-particle nonlinear system similar to (10). However, the analytic and numerical analysis of this system for $\tau \sim \varepsilon^{-1}$ is associated with certain difficulties [1–6].

Similar asymptotic expansions are also valid in the case of a more general hierarchy of the variation rate for both the slow variable β and the phase ψ, namely, when

$$\dot{\beta} = \varepsilon^k B_{k-2} + \varepsilon^{k+1} + \ldots \text{ and } \dot{\psi} = \varepsilon^l \omega(\beta) + \varepsilon^{l+1} + \ldots,$$

with $k > l \ge 1$. The case of $\omega \equiv 0$ can also be considered, for example, when $\dot{\beta} = \varepsilon^3 B_1$ and $\dot{\varphi} = \varepsilon^2 \Psi_0$. The corresponding asymptotic expansions are valid for $0 \le t \le L\varepsilon^{-k}$ (the kth-power scheme). Alongside the variant with one slow phase, a more complicated system containing a phase hierarchy can be analyzed, namely, when $\dot{\varphi}_1 \sim \varepsilon\omega_1$, $\dot{\varphi}_2 \sim \varepsilon^2\omega_2$, $\ldots$, $\dot{\varphi}_l \sim \varepsilon^l\omega_l$. In this case, the variable β must be 2π-periodic and slow: $\dot{\beta} \sim \varepsilon^k$, $k > l$.

The range of applicability of the approach proposed can be significantly extended. Instead of system (1), we now consider a more general system $\dot{x} = X(x, \varepsilon)$. If $\varepsilon = 0$, this general system has a family of asymptotically (exponentially) stable periodic (rotatory–oscillatory) solutions $x_0(\theta, x)$, where $\theta = \nu(a)t + \theta^0$ is a phase and a is a constant vector [1, 3, 8]. There exists a change of variables $x \longrightarrow (a, \theta, h)$ taking the form

$$x = x_0(\theta, a) + \frac{1}{2}[N(\theta, a)h + N^*(\theta, a)h^*], \tag{11}$$

where N is a complex-valued matrix 2π-periodic in the real phase, h is a vector, and the asterisk stands for the complex conjugation. The sum of dimensions of the vectors a, h, and θ is equal to the dimension of the vector x. In the neighborhood of the local integral manifold, the perturbed system is described by the equations [8]

$$\dot{a} = A(a, \theta, h, \varepsilon), \quad a(0) = a^0; \quad a, a^0 \in D_a,$$
$$\dot{\theta} = \nu(a) + \Theta(a, \theta, h, \varepsilon), \quad \theta(0) = \theta^0 (\text{mod} 2\pi),$$
$$\dot{h} = K(a)h + H(a, \theta, h, \varepsilon); \quad h(0) = h^0, \tag{12}$$
$$A, \Theta, H = O(|\varepsilon| + |h|^2).$$

Here, the functions A, ν, and Θ are real-valued and the characteristic indices of the matrix K have negative real parts if $a \in D_a$. For sufficiently small $|\varepsilon|$ and $|h|$, the solutions to system (12) approach the stable integral manifold arbitrarily closely within the period on the order of $\ln|\varepsilon|^{-1}$: $h_* = \varepsilon h_1(a, \theta) + \varepsilon^2 h_2 + \varepsilon^3 + \ldots$, where the functions h_j are found in the standard manner [1, 8, 9]. After substituting h_* into Eqs. (12), we obtain a standard system for a and θ with a rotating phase. Introducing the argument θ (by dividing $\dot{a}$ by $\dot{\theta}$), we can write out this system in the form of Eqs. (1). Furthermore, a method (standard or highest-power) of separation of the slow and fast variables, a and θ, respectively, is employed.

4. We now consider several examples of oscillatory systems analyzed by means of the second-power averaging method presented in Sections 1 and 2.

4.1. To illustrate the method proposed, first we consider the two-dimensional system

$$\dot{x} = \varepsilon f(x, y)\sin(t + \theta(x, y)), \quad \dot{y} = \varepsilon\gamma(x, y) \quad (13)$$

with corresponding initial conditions. The functions f, θ, and γ are assumed to be 2π-periodic in y and smooth in x and y. We transform the variable x according to Eqs. (3); i.e., we perform the change of variables $(x, y) \longrightarrow (\alpha, y)$. As a result of averaging over t, we obtain the equations of the first approximation (see Sections 1 and 2) with the slow time $\tau = \varepsilon t$, which serves as an independent variable:

$$\dot{\beta} = -\varepsilon\left(\frac{1}{2}f^2\theta'_\xi + \gamma(f\cos\theta)'_y\right), \dot{y} = \gamma(\beta, y),$$

$$0 \le \tau \le L\varepsilon^{-1}. \quad (14)$$

Here, there is no need to transform the slow variable y to the form of a phase because system (14) can be analyzed immediately. If the function γ averaged over y is nonvanishing for the values of β under consideration $[\beta = x + O(\varepsilon)]$, the passage to the phase φ and then to ψ are performed in a regular manner [1–3, 9] in accordance with Eqs. (3)–(5). In particular, if the function γ does not approach zero, it is convenient to pass from the argument τ to y, i.e., to analyze the equation for $\frac{d\beta}{dy}$.

Equation (14) can be averaged over y, and, as a result, the second term in its right-hand side vanishes. After averaging, system (14) can be completely integrated, because the variables of both its equations are separated. In this case, variations in the variables β and x are governed by the function $-\frac{f^2\theta'_\beta}{2\gamma}$ averaged over y and, in the general case, are on the order of $O(1)$ for $y \sim \varepsilon^{-1}$; i.e., $t \sim \varepsilon^{-2}$. The standard scheme [1–3] for a time interval $t \sim \varepsilon^{-1}$ leads to the expression $x = x^0 + O(\varepsilon)$.

4.2. In studying a many-particle quasi-linear system in the neighborhood of a resonance, one of its frequency mismatches often is larger (usually being on the order of $\sqrt{\varepsilon}$) than others. In this case, a system of the form (4) holds under corresponding assumptions, with the indicated mismatch being equal to $\sqrt{\varepsilon}\omega = \text{const}$. Herein, we use for convenience the parameter ε^2 instead of ε. As an example, we consider the system

$$\ddot{q} + Q(q) = P(t) - \Lambda\dot{q}, \quad q = \varepsilon r, \quad Q(0) = 0,$$

$$Q'(0) = v^2 > 0, \quad \chi = -\frac{1}{2}Q''(0),$$

$$\mu = -\frac{1}{6}Q'''(0), \quad (15)$$

$$P = \varepsilon^2 h\sin 2t + \varepsilon^3 f\sin(t + \kappa),$$

$$v = 1 + \varepsilon\gamma, \quad \Lambda = \varepsilon^2\lambda.$$

Omitting the terms on the order of $O(\varepsilon^4)$ and dividing Eqs. (15) by ε, we obtain a quasi-linear equation in the unknown r. This equation is then reduced to the variables x and y (the amplitude and the phase mismatches, respectively) by the conventional change of variables $r = x\cos(t + y)$ and $\dot{r} = -x\sin(t + y)$. Transforming the variables (x, y) in accordance with Eqs. (3)–(5), we arrive at the averaged system of the first approximation, with the slow time $\tau = \varepsilon t$ serving as an independent variable:

$$\dot{\beta} = \varepsilon\left(\gamma^2\beta\sin 2\psi - \frac{1}{4}\gamma^2\beta - \frac{1}{2}f\cos(\psi - \kappa)\right.$$

$$\left. -\frac{1}{2}\lambda\beta + \cos\psi\left(\frac{2}{3}h\gamma - \frac{1}{2}\chi\gamma\beta^2\sin 2\psi\right)\right),$$

$$\dot{\psi} = \gamma, \quad \beta = x + O(\varepsilon) = x^0\exp\left[-\frac{1}{2}\varepsilon\left(\frac{1}{2}\gamma^2 + \lambda\right)\tau\right], \quad (16)$$

$$0 \le \tau \le \frac{L}{\varepsilon}.$$

The frequency mismatch $\varepsilon\gamma$ in Eqs. (15) results in an additional exponential damping for $t \sim \varepsilon^{-2}$. The standard approach leads to $x = x^0 + O(\varepsilon)$ for $t \sim \varepsilon^{-1}$.

4.3. Lastly, we consider quasi-linear parametric oscillations in the vicinity of the second resonance zone [7]. They describe the motion of a plane physical pendulum whose axis of suspension periodically vibrates in both vertical and horizontal directions. We introduce a small parameter and make corresponding assumptions, similar to (15), relevant to orders of the quantities. As a result, we obtain the desired equation

$$\ddot{z} + (4 - \varepsilon\cos 2t)z = -4\varepsilon\gamma z$$

$$-\varepsilon^2\left(4\gamma^2 z + \lambda\dot{z} - \frac{2}{3}z^3 + 4d\sin(2t + \kappa)\right). \quad (17)$$

The parameters ε, $\varepsilon^3 d$, and $\varepsilon^2\lambda$ relate to the amplitudes of vertical and horizontal vibrations and the energy dissipation, respectively. By passage to the variables (x, y) (i.e., amplitude and phase mismatch), this equation is reduced to the form of Eqs. (1), for which the second-power averaging scheme is applicable. The averaging over the explicit argument t leads to equations similar to (16). However, the right-hand side of the equation for the variable β is very cumbersome. Under the assumption that $\gamma \sim 1$, we obtain expressions similar to (16), which are valid in the interval $t \sim \varepsilon^{-2}$ with an error on the order of $O(\varepsilon)$. It is worth noting that for $\gamma \sim \varepsilon$ the evolution of the system is much more complicated than that for $\gamma \sim 1$ [7] because in the latter case the averaging over ψ significantly simplifies the situation.

REFERENCES

1. N. N. Bogolyubov and Yu. A. Mitropol'skii, *Asymptotic Methods in the Theory of Nonlinear Oscillations* (Nauka, Moscow, 1974, 4th ed.; Gordon and Breach, New York, 1962).

2. V. M. Volosov and B. I. Morgunov, *Averaging Method in the Theory of Nonlinear Oscillatory Systems* (Mosk. Gos. Univ., Moscow, 1971).

3. L. D. Akulenko, *Asymptotic Methods of Optimal Control* (Nauka, Moscow, 1987).

4. A. I. Neĭshtadt, Prikl. Mat. Mekh. **48**, 197 (1984).

5. V. I. Arnol'd, V. V. Kozlov, and A. I. Neĭshtadt, *Dynamical Systems*, Ed. by V. I. Arnol'd (VINITI, Moscow, 1985; Springer-Verlag, Berlin, 1989), Vol. 3.

6. F. L. Chernous'ko, Prikl. Mat. Mekh. **27**, 474 (1963).

7. L. D. Akulenko, Prikl. Mat. Mekh. **65**, 845 (2001).

8. Yu. A. Mitropol'skiĭ and O. B. Lykova, *Integral Manifolds in Nonlinear Mechanics* (Nauka, Moscow, 1973).

9. L. D. Akulenko, Izv. Akad. Nauk, Mekh. Tverd. Tela, No. 3, 26 (1995).

Translated by V. Chechin

<div align="center">═══════════ MECHANICS ═══════════</div>

Suppressing Convective Instability of a Vertical Thin-Layer Flow by Feedback Control

V. A. Buchin and G. A. Shaposhnikova

Presented by Academician S.S. Grigoryan July 20, 2001

Received July 23, 2001

INTRODUCTION

A control problem for a thin layer of a viscous incompressible fluid flowing down a vertical wall is studied. A feedback regulator using both cooling and heating of the wall is proposed to suppress the convective flow instability. The structure of the regulator stabilizing low-frequency harmonic perturbations of the flow is determined.

SYSTEM OF EQUATIONS AND FORMULATION OF THE PROBLEM

To describe a thin layer of a viscous incompressible fluid flowing down a vertical wall, we use the following system of equations [1]:

$$\frac{\partial h}{\partial t} + \frac{\partial q}{\partial x} = 0, \tag{1}$$

$$\frac{\partial q}{\partial t} + 1.2\frac{\partial}{\partial x}\frac{q^2}{h} = gh - \frac{3\nu q}{h^2}. \tag{2}$$

Here, t is time, x is the coordinate directed along the gravity force, h is the layer thickness, q is the flow rate, ν is the kinematic viscosity, and g is the acceleration of gravity.

In this paper, we consider the evolution only of long-wave perturbations; therefore, the term associated with the surface tension is omitted in equation (2).

The fluid temperature T enters into the kinematic viscosity as a parameter; i.e., $\nu = \nu(T)$. The investigation concerns sufficiently thin layers such that at any time moment their temperature can be considered as equal to the wall temperature. For small deviations of

─────────────

Institute of Mechanics, Moscow State University,
Michurinskiĭ pr. 1, Moscow, 117234 Russia

temperature from the steady wall temperature T_0, we can write out

$$\nu = \nu_0\left(1 + \frac{\partial\nu}{\partial T}\frac{\Delta T}{\nu_0}\right), \quad \Delta T = T - T_0,$$
$$\nu_0 = \nu(T_0). \tag{3}$$

Thus, the variation of wall temperature changes fluid viscosity and, consequently, the last term in equation (2). As a result, the existence of the temperature difference ΔT, in fact, leads to the appearance of an additional force applied to the layer.

By using representative values of layer thickness, the volume flow, time, and layer length denoted by h_r, q_r, t_r, and L, respectively, we introduce the following dimensionless variables and parameters:

$$t^* = \frac{t}{t_r}, \quad x^* = \frac{x}{L}, \quad q^* = \frac{q}{q_r}, \quad h^* = \frac{h}{h_r},$$

$$q_r = \frac{gh_r^3}{3\nu_0}, \quad t_r = \frac{h_r L}{q_r}, \quad \beta = \frac{9\nu_0^2 L}{gh_r^4}.$$

Furthermore, asterisks used as superscripts of dimensionless variables are omitted.

The effect of unsteady temperature variation along the x direction on the fluid-layer flow is described by the dimensionless function

$$\Theta(t, x) = -\frac{\partial\nu}{\partial T}\frac{\Delta T(t, x)}{\nu_0}, \quad \frac{\partial\nu}{\partial T} = \frac{\partial\nu}{\partial T}(T_0). \tag{4}$$

In the case of the constant wall temperature $T = T_0$, the system of equations (1), (2) has the steady-state solution

$$q = 1, \quad h = 1. \tag{5}$$

It can be shown that both characteristics of the hyperbolic system (1), (2) are directed downstream so that all perturbations brought into the layer drift along this direction.

As is known, the steady-state solution describing the vertical fluid-layer flow is unstable. Remaining bounded at an arbitrary fixed x, the amplitude of small

harmonic perturbations brought in at a certain flow point increases downstream.

The force caused by temperature variations allows realization of the control action onto the fluid layer and, if necessary, suppression of convective instability with the help of a feedback regulator.

We now discuss the feedback structure. The vertical surface is partitioned into a system of segments, each of length d. An external device varies wall temperature inside each segment so that the deviation of the current temperature from T_0 is proportional to the deviation of the layer thickness from its steady-state value at a given point of the segment under consideration. For the kth segment, we have

$$\Theta = \Theta(t, x) = \alpha[h(t, x_k) - 1]\Phi_k(x),$$
$$x_k = kd, \tag{6}$$

where α is the gain factor, x_k is the coordinate of the point sensor situated in the kth segment, and $\Phi_k(x)$ is the given function localized in this segment.

SUPPRESSION OF SMALL PERTURBATIONS

We now analyze the problem of suppressing small perturbations in the linear formulation. To do this, we introduce the functions q_1 and h_1:

$$q = 1 + q_1, \quad h = 1 + h_1,$$
$$q_1 \ll 1, \quad h_1 \ll 1. \tag{7}$$

We assume that, within the first surface segment $(0 \le x \le d)$, $\Phi_k(x) \equiv 1$ and the control action has the form

$$\Theta = \alpha h_1(t, d). \tag{8}$$

Then, q_1 and h_1 satisfy the system of equations

$$\frac{\partial}{\partial t}h_1 + \frac{\partial}{\partial x}q_1 = 0, \tag{9}$$

$$\frac{\partial}{\partial t}q_1 + 2.4\frac{\partial}{\partial x}q_1 - 1.2\frac{\partial}{\partial x}h_1$$
$$= -\beta(q_1 - 3h_1 - \alpha h_1(t, d)). \tag{10}$$

Harmonic perturbations are assumed to be brought continuously into the layer at $x = 0$. Therefore, the boundary conditions have the form

$$x = 0, \quad h = h_0\exp\{i\omega t\}, \quad q = q_0\exp\{i\omega t\}, \tag{11}$$

where, generally speaking, q_0 and h_0 are complex numbers.

The solution to the system of equations (9), (10), which satisfies the boundary conditions (11), is sought as

$$h = H(x)\exp\{i\omega t\}, \quad q = Q(x)\exp\{i\omega t\}. \tag{12}$$

Relations (9)–(12) lead to both a system of equations and boundary conditions for the functions $Q(x)$ and $H(x)$. The solution to this system can be represented in the form

$$\begin{pmatrix} Q(x) \\ H(x) \end{pmatrix} = \begin{pmatrix} A_{11}(i\omega, x) & A_{12}(i\omega, x) \\ A_{21}(i\omega, x) & A_{22}(i\omega, x) \end{pmatrix} \begin{pmatrix} q_0 \\ h_0 \end{pmatrix}. \tag{13}$$

Elements of the transition matrix $\{A_{ij}\}$ have the following structure:

$$A_{ij}(i\omega, x) = \frac{B_{ij}(i\omega, x)}{\Delta(i\omega)},$$

$$\Delta(i\omega) = 1 + \frac{\beta\alpha k_1 k_2}{(i\omega + \beta) \times 2i\omega\sqrt{D}}(\exp\{k_1 d\} - \exp\{k_2 d\}),$$

$$k_1 = -\left(i\omega + \frac{5}{4}\beta\right) + \sqrt{D}, \quad k_2 = -\left(i\omega + \frac{5}{4}\beta\right) - \sqrt{D},$$

$$D = -\frac{1}{6}\omega^2 + \frac{5}{3}\beta i\omega + \frac{25}{16}\beta^2.$$

Here, the functions $B_{ij}(i\omega, x)$ and $\Delta(i\omega)$ are such that $B_{ij}(\lambda, x)$ and $\Delta(\lambda)$ represent analytic functions of the complex-valued argument λ in the right half-plane $\mathrm{Re}\,\lambda \ge 0$. In the imaginary axis, $\lambda = i\omega$.

The eigenvalues μ_1 and μ_2 of the matrix $\{A_{ij}\}$ are determined by the formulas

$$\mu_{1,2} = \frac{A_{11} + A_{22}}{2} \pm \sqrt{\frac{(A_{11} - A_{22})^2}{4} + A_{12}A_{21}}.$$

The values μ_1 and μ_2 characterize variations of the flow rate and layer thickness with increasing the coordinate x. If μ_1 and μ_2 are modulo smaller than unity, both the volume flow and thickness perturbations decrease with increasing x; if they are modulo larger than unity, the perturbations grow with x.

In the absence of a regulator ($\alpha = 0$), $|\mu_1| > 1$ or $|\mu_2| > 1$ for all frequencies of the perturbations brought in at $x = 0$. Consequently, the perturbation of any frequency grows with x; i.e., the steady-state thin-layer flow is unstable.

Introducing a control leads to the onset of an infinite discrete set of self-oscillations of the system. Among these oscillations, there can be both stable and unstable ones. The eigenvalues λ_k ($k = 1, 2, \ldots$) corresponding to these self-oscillations are calculated by solving the equation $\Delta(\lambda) = 0$. Parameters of the regulator should be chosen in a manner that provides all self-oscillations to be stable. This requirement is satisfied if all roots of

the equation $\Delta(\lambda) = 0$ belong to the left half-plane $\mathrm{Re}\,\lambda_k < 0$. By virtue of the Rouché theorem [2], the condition $\mathrm{Re}\,\lambda_k < 0$ is certainly satisfied for

$$|\alpha| < \frac{1}{\max\limits_{-\infty < x < \infty} |\Psi(i\omega)|}, \quad \Psi(i\omega) = \frac{1 - \Delta(i\omega)}{\alpha}.$$

Numerical investigations carried out for $\beta = 1$ show that, for any d ($d \le 1$), there is an α range ($\alpha_{\min} < \alpha < \alpha_{\max}$, $\alpha_{\min} < 0$, $\alpha_{\max} > 0$) not containing roots of the equation $\Delta(\lambda) = 0$. Perturbations generated by the regulator and corresponding to this range are damped. Values of $|\alpha_{\min}|$ and $\alpha_{\max}$ depend on d and grow as it increases. At $d = 1$, $\alpha_{\min} = -3$ and $\alpha_{\max} = 4$, while, at $d = 0.1$, $\alpha_{\min} = -25.8$ and $\alpha_{\max} = 34.4$.

To suppress the perturbations being brought in into the flowing layer, parameters α and d of the regulator are chosen in the range $\alpha_{\min}(d) < \alpha < \alpha_{\max}(d)$, within which its self-oscillations are stable.

Numerical investigation of the effect of the regulator parameters α and d ($\alpha_{\min} < \alpha < \alpha_{\max}$) on μ_1 and μ_2 was carried out for the frequency ω ranging from 0 to 100. At $d = 0.1$, Fig. 1 shows the quantity $y = \max\{|\mu_1|, |\mu_2|\}$ as a function of the frequency ω for $\alpha = 0$ (curve *1*, absence of the regulator) and for values $\alpha = -2$ (curve *2*) $\alpha = -5$ (curve *3*), and $\alpha = -10$ (curve *4*). As is seen, for $d = 0.1$ and $\alpha = -2$, stabilization of the perturbations occurs in the range $0 < \omega < 30$, while at $d = 0.1$ and $\alpha = -10$, this is true within the range $15 < \omega < 60$. To stabilize higher frequencies ($\omega > 60$), one should decrease d and α. For example, the regulator with $d = 0.01$ and $\alpha = -20$, stabilizes the oscillations from the range $3 < \omega < 100$.

The results obtained for $\beta = 1$ can be also used for $\beta \ne 1$ by dividing the corresponding value of d by β and multiplying the corresponding ω by β.

The above-considered problem concerns the stabilization within the first surface segment. As a result, it was established that at the exit of the first segment, amplitudes of the perturbations brought in are multiplied by $y = \max\{|\mu_1|, |\mu_2|\}$. Since the perturbations propagate only downstream, the stabilization within each segment can be considered in the same manner as within the first one and independently of the others. Consequently, after passing through n segments, the initial amplitude is multiplied by y^n.

NUMERICAL INVESTIGATION OF CONVECTIVE-INSTABILITY SUPPRESSION WITH THE HELP OF THE FEEDBACK REGULATOR

Here, we numerically investigate the development of perturbations brought into the flow at $x = 0$ and having the form

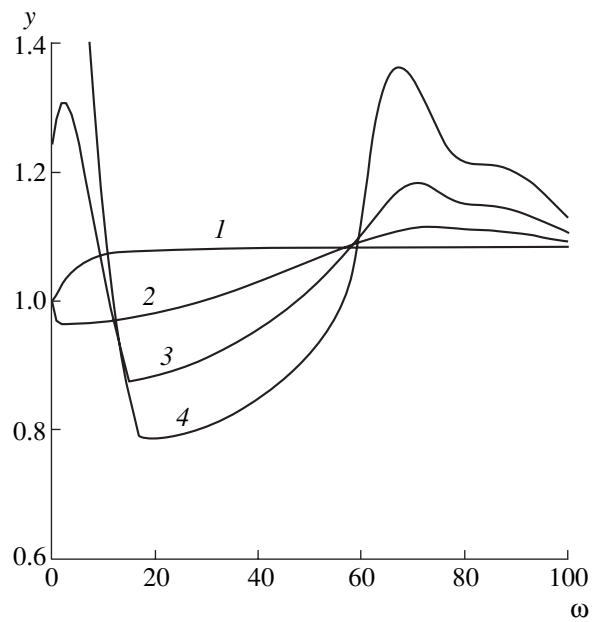$$h_1 = h_0 \sin(\omega t + \varphi), \quad q_1 = q_0 \sin(\omega t).$$

Fig. 1. Dependence of $y = \max\{|\mu_1|, |\mu_2|\}$ on the frequency ω at $\beta = 1$, $d = 0.1$: (*1*) $\alpha = 0$; (*2*) -2; (*3*) -5; and (*4*) -10.
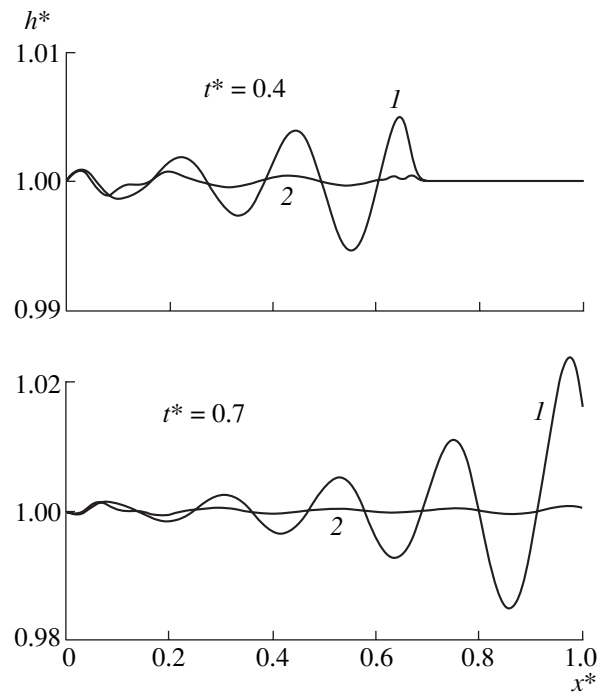

Fig. 2. Development of harmonic perturbations with the frequency $\omega = 50$ at the time moments $t^* = 0.4$ and 0.7 for $\alpha = -2$, $\beta = 5$, and $d = 0.02$: (*1*) without the regulator and (*2*) with the regulator.

To suppress the convective instability, we use the control action of form (8).

The system of equations (1), (2) is solved by the Godunov method. The calculations are carried out for different values of the parameters β, q_0, h_0, φ, and ω.

Figure 2 presents results of the numerical calculations for $\beta = 5$, $\omega = 50$, $q_0 = 0.001$, and $h_0 = 0$. A dimensionless coordinate x and a dimensionless layer thickness h are plotted as an abscissa and an ordinate, respectively. The development of the convective instability in the absence of the regulator is shown in Fig. 2 by curves *1*, while the effect of the regulator is illustrated by curves *2*. The regulator parameters $\alpha = -2$ and $d = 0.02$ are chosen according to the results obtained in item 2 of this paper. Switching on the regulator and starting generation of the perturbations occurred simultaneously at $t = 0$. Figure 2 presents states of the fluid layer for the time $t^* = 0.4$ and 0.7. The regulator with the chosen parameters suppresses the perturbations within the range $0 < \omega < 150$. To suppress higher frequency perturbations, we should use the regulator with other parameters chosen in accordance with the results of item 2.

REFERENCES

1. V. Ya. Shkadov, *Certain Methods and Problems in Theory of Hydrodynamic Stability* (Mosk. Gos. Univ., Moscow, 1973), Nauch. Tr. Inst. Mekh. Mosk. Gos. Univ., No. 25.

2. M. A. Lavrent'ev and B. V. Shabat, *Methods in the Theory of Functions of a Complex Variable* (Nauka, Moscow, 1973).

Translated by Yu. Verevochkin

===== **MECHANICS** =====

Anomalies in Mechanical Characteristics of Nanometer-Size Objects

A. M. Krivtsov and Academician N. F. Morozov

Received July 18, 2001

In recent years, rapid development of nanotechnologies led to the necessity of constructing adequate physical models that make it possible to describe physicomechanical properties of objects with a nanometer-size (nanosize) scale. The majority of existing models of such a kind adopt that basic mechanical characteristics of nanosize objects correspond to those obtained in macroscopic experiments. However, when dealing with structures containing only several atomic layers, the discrepancy arises between the evident discreteness of an object under study and a continual method of its description. The inconsistency of values of elastic moduli, which were obtained in microscale and macroscale experiments, was noted by many researchers. In particular, one of the methods of determining elastic characteristics of nanosize objects is investigating the microrelief arising in the course of tension of a specimen having an ultrathin coating [1–3]. The solution to an equivalent continual problem allows the Poisson's ratio and Young modulus for the coating to be determined from such experiments [2, 4, 5]. However, the values of elastic characteristics measured by this method exhibit a substantial inconsistency by their macroscopic values for the same material.

In the present study, we used a two-dimensional strip made of a single-crystal material with a hexagonal closely packed (HCP) lattice as a model for studying the effect of scaling on mechanical properties of a material. The interaction between atoms is assumed to be dual. The basic problem of our study is determining the dependence of the Poisson's ratio and Young modulus of a finite (in one direction) single crystal on the number of atomic layers.

We consider a two-dimensional single crystal shown in the figure. The crystal possesses an infinite length along the x direction and $N \geq 2$ atomic layers in the y direction. Each atom interacts only with its nearest neighbors, as is shown in the figure. Constant tensile forces Q are applied to atoms located at crystal ends. The deformed single-crystal state under consideration

is completely determined by the distance a between neighboring atoms in each layer and by the interlayer distance h. We denote by the symbol b the distance between nearest atoms in neighboring layers (see figure). In this case, evidently, the relationship $b^2 = \dfrac{a^2}{4} + h^2$ is valid. In the undistorted state, the lattice consists of equilateral triangles with an edge $a = b = a_0$, and the end load is absent ($Q = 0$). Let $F(r)$ be the force of interaction between two atoms separated by distance r (the attraction is considered as positive) Then, projecting onto the y direction the equation of equilibrium for an atom situated at the crystal surface, we find

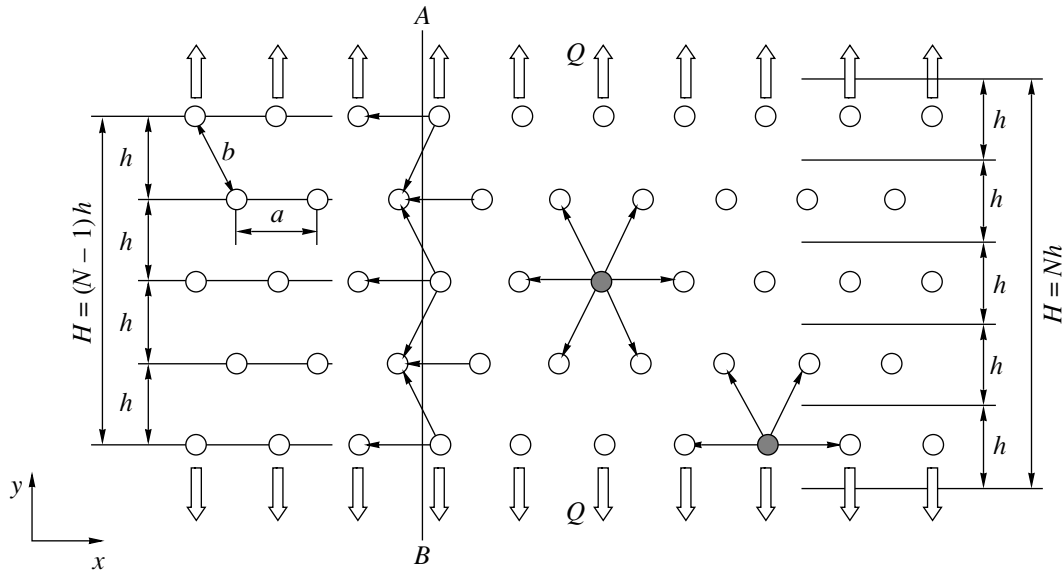$$Q = 2\frac{h}{b}F(b) \Rightarrow \sigma_2 \overset{\text{def}}{=} \frac{Q}{a} = 2\frac{h}{ab}F(b). \qquad (1)$$

Here, σ_2 is the normal stress in the y direction. We now mentally cut the crystal by a vertical straight line AB (see figure). The total normal force acting from one part of the crystal onto the other part can be written out as

$$H\sigma_1 = NF(a) + (N-1)\frac{a}{2b}F(b). \qquad (1a)$$

Here, σ_1 is the normal stress in the x direction and H is the crystal thickness (its extension along the y direction). The quantity H, in principle, cannot be determined unambiguously. For example, if we assume that the crystal thickness is equal to the distance between atomic layers lying on opposite crystal ends (see figure), then, in this case, $H = (N-1)h$. On the other hand, it is quite reasonable to determine the crystal thickness as a product of the number of layers by the thickness of a single layer, which results in the formula $H = Nh$. Therefore, we denote

$$H \overset{\text{def}}{=} N_* h, \quad N - 1 \leq N_* \leq N, \qquad (2)$$

where N_* is the quantity reflecting an arbitrariness in the determination of H. By virtue of the smallness of

St. Petersburg State Technical University,
ul. Politechnicheskaya 29, St. Petersburg, 195251 Russia

Two-dimensional single-crystal strip.

strains, forces acting within the crystal can be approximately written out in the form

$$F(a) = C\Delta a, \quad F(b) = C\Delta b, \quad C \stackrel{\text{def}}{=} F'(a_0) > 0, \quad (3)$$

where C has a meaning of the rigidity of an interatomic bond, while the symbol Δ implies the deviation of a certain quantity from its value corresponding to the undistorted crystal. We denote the crystal strain in the x and y directions as ε_1 and ε_2, where

$$\varepsilon_1 \stackrel{\text{def}}{=} \frac{\Delta a}{a_0}, \quad \varepsilon_2 \stackrel{\text{def}}{=} \frac{\Delta h}{h_0}, \quad h_0 \equiv \frac{\sqrt{3}a_0}{2}. \quad (4)$$

The substitution of relationships (2), (3), and (4) into expressions (1) and (1a) yields the elasticity relations

$$\sigma_1 = \frac{\sqrt{3}}{12}\frac{C}{N_*}((9N-1)\varepsilon_1 + 3(N-1)\varepsilon_2),$$

$$(5)$$

$$\sigma_2 = \frac{\sqrt{3}}{4}C(\varepsilon_1 + 3\varepsilon_2).$$

As is seen from relations (5), the crystal under consideration is anisotropic. We recall that the infinite crystal with the HCP crystal lattice is isotropic and, hence, the anisotropy indicated is a manifestation of the scale factor. Furthermore, we denote

$$\nu_1 \stackrel{\text{def}}{=} -\frac{\varepsilon_2}{\varepsilon_1}\bigg|_{\sigma_2 = 0}, \quad E_1 \stackrel{\text{def}}{=} \frac{\sigma_1}{\varepsilon_1}\bigg|_{\sigma_2 = 0};$$

$$\nu_2 \stackrel{\text{def}}{=} -\frac{\varepsilon_1}{\varepsilon_2}\bigg|_{\sigma_1 = 0}, \quad E_2 \stackrel{\text{def}}{=} \frac{\sigma_2}{\varepsilon_2}\bigg|_{\sigma_1 = 0}.$$

Here, ν_1 and E_1 are the Poisson's ratio and Young modulus for tension along the x axis; the quantities ν_2 and E_2 correspond to tension along the y axis. Using relationships (5), we obtain

$$\nu_1 = \nu_\infty, \quad E_1 = \frac{N}{N_*}E_\infty;$$

$$\nu_2 = \frac{N-1}{N-1/9}\nu_\infty, \quad E_2 = \frac{N}{N-1/9}E_\infty,$$

where, $\nu_\infty = \frac{1}{3}$ and $E_\infty = \frac{2C}{\sqrt{3}}$ are values of the Poisson's ratio and Young modulus, which correspond to the infinite crystal [6, 7]. We now analyze the formulas obtained. Under tension along atomic layers, the Young modulus E_1 substantially depends on the quantity N_*, i.e., on a method for determining the thickness of the nanocrystal strip. If we assume that $N_* = N$ (N is the maximal value of N_*) then, under tension along atomic layers, the Poisson's ratio and Young modulus are independent of a number of layers. Evidently, this is associated with the fact that in the longitudinal direction, the crystal under consideration is infinite. By contrast, the Young modulus E_1^{max} corresponding to the minimal value $N_* = N - 1$, is not constant. It increases with a decrease in the number of atomic layers and for $N = 2$ attains a value twice as large as E_∞ (see table). Thus, the ambiguity in determining the Young modulus turns out to be rather substantial for small values of N. In the case of tension in the direction perpendicular to atomic layers, both the Poisson's ratio and the Young modulus depend on N, the former decreasing and the latter

increasing with the reduction in the number of layers. The values of the Poisson's ratio and Young modulus for different N are presented in the table. It is worth noting that for $N = 2$ the Poisson's ratio is smaller than ν_∞ almost by a factor of 2. As $N \longrightarrow \infty$, elastic moduli tend to values corresponding to the infinite crystal, which are independent of the deformation direction.

Based on the studies performed, we can list the basic properties intrinsic to nanocrystals.

1. For the Young modulus of a nanocrystal, only a possible interval of values is determined. This is associated with the impossibility of unambiguously determining the size of a nanoobject.

2. Elastic properties of a nanocrystal substantially depend on the number of atomic layers forming it.

3. The shape and size of a nanocrystal introduce an additional anisotropy into its elastic properties.

The effects listed are obtained on the basis of a rather simplified model. However, as far as they manifest themselves for the simplest nanocrystal, they must all the more play an important role in the case of more complicated nanocrystalline objects. The indicated ambiguity in the determination of the Young modulus, evidently, manifests itself for all mechanical characteristics whose definition substantially involves the concept of the nanoobject's size. In particular, the specific deformation energy per unit volume is determined ambiguously.

In the present study, we took into account the interaction of only neighboring atoms in the crystal lattice. It can be shown that allowance for further neighbors leads to the enhanced effect of the scale factor, especially in the three-dimensional case.

Thus, the concepts of classical continuum mechanics, including those of the elasticity theory, must be used with great care in the case of their application to nanoobjects. It is necessary to take into account the variation of mechanical characteristics when scales of objects under consideration approach nanometers. Special attention should be paid to quantities (such as the Young modulus) that are in principle ambiguous at the nanometer level. Using them, we must clearly define

Poisson's ratio and Young modulus of a nanocrystal as functions of the number of atomic layer

N	$E_1^{\mathrm{max}}/E_\infty$	ν_2	ν_2/ν_∞	E_2/E_∞
2	2.00	0.18	0.53	1.06
3	1.50	0.23	0.69	1.04
4	1.33	0.26	0.77	1.03
5	1.25	0.27	0.82	1.02
10	1.11	0.30	0.91	1.01
20	1.05	0.32	0.96	1.01
50	1.02	0.33	0.98	1.00
100	1.01	0.33	0.99	1.00

what we imply while applying these quantities to nanoobjects.

ACKNOWLEDGMENTS

REFERENCES

1. A. L. Volynskiĭ, I. V. Chernov, and N. F. Bakeev, Dokl. Akad. Nauk **355**, 491 (1997).

2. S. L. Bazhenov, A. L. Volynskiĭ, E. E. Voronina, and N. F. Bakeev, Dokl. Akad. Nauk **367**, 75 (1999).

3. Yu. P. Baĭdarovtsev, G. N. Savenkov, and V. A. Tarasenko, Vysokomol. Soedin., Ser. A **41**, 1302 (1999).

4. D. L. Bykov and D. N. Konovalov, in *Proceedings of the XXXVI International Workshop "Topical Problems of Strength," Vitebsk, 2000*, p. 428.

5. D. L. Bykov and D. N. Konovalov, Vestn. Tambov. Gos. Univ. **5** (314), 224 (2000).

6. A. M. Krivtsov, Tr. S.-Peterb. Gos. Tekh. Univ. **443**, 9 (1992).

7. A. M. Krivtsov, Z. Angew. Math. Mech. **79** (S2), 419 (1999).

Translated by G. Merzon